DESIGN AND FABRICATION OF SERS GUIDED TARGETED NANOPROBES TOWARDS CANCER MANAGEMENT

Thesis Submitted to AcSIR for the Award of the Degree of
DOCTOR OF PHILOSOPHY
in Chemical Sciences

AcSIR

By

NISHA N.

Registration No: 10CC13J39010

Under the guidance of

Dr. KAUSTABH KUMAR MAITI

**CSIR-NATIONAL INSTITUTE FOR INTERDISCIPLINARY
SCIENCE AND TECHNOLOGY (CSIR-NIIST)
THIRUVANANTHAPURAM-695 019, KERALA, INDIA**

November, 2017

DEDICATED TO

MY PARENTS, BROTHER AND TEACHERS...

DECLARATION

I hereby declare that the matter embodied in the thesis entitled: " *Design and Fabrication of SERS guided Targeted Nanoprobes Towards Cancer Management*" is the result of the investigations carried out by me at the Organic chemistry Section, Chemical Sciences and Technology Division, CSIR-National Institute for Interdisciplinary Science and Technology (CSIR-NIIST), Thiruvananthapuram, under the supervision of Dr. Kaustabh Kumar Maiti and the same has not been submitted elsewhere for any other degree.

In keeping with the general practice of reporting scientific observations, due acknowledgement has been made wherever the work described is based on the findings of other investigators.

Nisha N.

Thiruvananthapuram
27-11-2017

CERTIFICATE

This is to certify that the work embodied in this Ph. D. thesis entitled "***Design and Fabrication of SERS Guided Targeted Nanoprobes towards Cancer Management***" submitted by **Ms. Nisha N.** to Academy of Scientific and Innovative Research (AcSIR), in partial fulfilment of the requirements for the award of the **Degree of Doctor of Philosophy in Chemical Sciences**, has been carried out under my supervision and guidance at the Organic chemistry Section, Chemical Sciences and Technology Division of the CSIR-National Institute for Interdisciplinary Science and Technology (CSIR-NIIST), Thiruvananthapuram. I further certify that this work has not been submitted to any other University or Institution in part or full for the award of any degree or diploma.

Dr. Kaustabh Kumar Maiti
(Thesis Supervisor)

ACKNOWLEDGEMENTS

CONTENTS

List of Abbreviations

AO	Acridine orange
ATCC	American Type Culture Collection
a.u.	Arbitrary unit
AuNCs	gold nanocubes
AuNPs	Gold nanoparticles
BSA	Bovine Serum Albumin
c	Concentration
CARS	Coherent anti-Stokes Raman spectroscopy
$CDCl_3$	Deuterated chloroform
CE	chemical enhancement
$CHCl_3$	Chloroform
cm	Centimeter
CTAB	Cetyl trimethyl ammonium bromide
CTCs	circulating tumor cells
CV	Crystal Violet
d	Doublet
DAB	3,3'-Diaminobenzidine
DIC	N,N'-Diisopropylcarbodiimide
DIPEA	N,N-Diisopropylethylamine
DLS	Dynamic light scattering
DMEM	Dulbecco's Modified Eagle's Medium
DMF	Dimethyl formamide
DMSO	Dimethyl Sulfoxide
DNA	Deoxyribonucleic acid
DOX	doxorubicin
DTTC	Diethylthiatricarbocyanine

EB	ethidium bromide
EDC	3-(dimethylamino)-propyl)-N′-ethylcarbodiimide
EGFR	Epidermal growth factor receptor
EM	electromagnetic
ESI	Electrospray ionization
FITC	Fluorescein isothiocyanate
FR	folate receptor
g	gram
GNR	gold nanorod
h	Hour
HATU	1-[Bis(dimethylamino)methylene]-1H-1,2,3-triazolo[4,5-b]pyridinium 3-oxide hexafluorophosphate
HER2	human epidermal growth factor receptor2
HRMS	High resolution mass spectrometry
HR-TEM	High-resolution transmission electron microscopy
Hz	Hertz
J	Coupling constant
LSPR	localized surface plasmon resonance
M	Molar
m	Multiplet
M^+	Molecular ion
4-MBA	4-mercaptobenzoic acid
max	Maximum
mg	Milligram
MGITC	melachite green isothiocyanate
MHz	Megahertz
min	Minutes
mL	Milliliter

mmol	Millimolar
MMP	Matrix metalloproteinases
MTT	3-(4,5-dimethylthiazol-2-yl)-2,5-diphenyltetrazolium bromide
MW	Molecular weight
n	Normal
NA	Numerical Aperture
Nd:YAG	Neodymium-doped Yttrium Aluminum Garnet
NHS	N-hydroxy succinimide
NIR	Near-infrared
NPs	nanoparticles
PAGE	Polyacrylamide gel electrophoresis
PBS	phosphate buffered saline
PEG	Polyethylene glycol
ppm	Parts per million
PTT	Photothermal therapy
RRS	Resonance Raman spectroscopy
RSM	Raman signature molecule
rt	Room temperature
s	Singlet
SAM	self-assembled monolayer
SDS	sodium dodecyl sulfate
SERRS	surface-enhanced resonance Raman scattering
SERS	Surface-enhanced Raman spectroscopy
SPPS	solid phase peptide synthesis
SPR	surface plasmon resonance
SQ	Squaraine dye
T	Temperature
t	Triplet
TEA	Triethylamine
THF	Tetrahydrofuran

TMS	Tetramethylsilane
TPL	two-photon luminescence
UV	Ultraviolet
Vis	Visible
λ	Wavelength
ε	Molar extinction coefficient
λ_{ex}	Excitation wavelength
μM	Micromolar
φ_f	Fluorescence quantum yield

PREFACE

Cancer is one of the life threatening diseases and second leading cause of death. The increased mortality rate reported for the cancer patients can be attributed to the failure of the early stage detection and diagnosis with the existing conventional tools. Development of advanced optical methods and tools for probing living cells and intracellular processes is a topic of rapidly growing interest in cell biology which intern helps in the diagnosis and prognosis of diseases like cancer. Fluorescence based techniques were used for the imaging of biological samples, but these techniques suffer significant limitations mainly related to a) photo bleaching of fluorescent labels, b) poor chemical selectivity c) phototoxicity etc. Recently surface enhanced Raman scattering (SERS) opened up exciting new windows for bio-imaging. SERS imaging technique is a powerful noninvasive technique with high specificity due to fingerprinting character. SERS spectra of single cells provides specific fingerprint that can be used to determine cell types (e.g., normal versus tumour), cell stages (e.g., normal versus apoptotic). SERS with excellent multiplexing ability and ultra high sensitivity offers exclusive advantages over other imaging modalities. SERS not only opens up new vistas for disease diagnosis and imaging but also provides strong platform to integrate therapy with diagnosis. Although significant achievements have been acquired in past few decades, it has not been fully exploited, as more advances in this technique can make a mark in biomedical applications. The first Chapter of the thesis describes the fundamentals of SERS along with basic fabrication strategies for SERS nanotags. In addition, some of the recent literature reports on SERS based theranostic nanoprobes are also briefly described in this chapter.

SERS-based immunoassays have established enormous applications in biochemical analysis and clinical diagnosis. At present, these SERS platforms are being applied for analyzing real samples and have become a significant tool for the accurate diagnosis of cancer. Chapter 2 of the thesis deals with the exploration of squaraine dyes as potential Raman signature molecule for the construction of SERS nanotags towards the early diagnosis of cervical cancer. The SERS fingerprinting of the six synthesized squaraine dyes revealed the similar spectral pattern which reflected the architectural design of squaraine dyes. Nanoprobes were prepared by conjugating anti-EGFR and p16/Ki-67 antibodies on PEG encapsulated spherical AuNPs. Next, SERS imaging of cervical cancer HeLa cells was carried out by incubating with antibody conjugated nanotags. When SERS nanotag conjugated with p16/Ki-67 dual antibody corresponding to the overexpressed nuclear receptor, nanotags were mostly localized to the nucleus as observed in color coded cluster map which confirmed the recognition with the nuclear receptor. When nanotag conjugated with anti-EGFR was treated on HeLa cells, nanotags were mostly localized on the cell surface indicating the selective recognition of cell surface EGFR as a biomarker. Thus the superiority of highly sensitive and ultrafast SERS technique over conventional immunocytochemistry technique is well explored.

In the third chapter of the thesis, synergistic photothermal chemotherapy using gold nanorod (GNR) conjugated doxorubicin (DOX) with particular emphasis to SERS based monitoring of apoptotic events in molecular level is described. Gold nanorod which acts both as a SERS substrate and a photo thermal agent was functionalized with MMP targeting peptide sequence attached squaraine dye along with pH-sensitive hydrazone bonded DOX-lipoic acid conjugate. In vitro photothermal chemotherapy was evaluated on human

fibrosarcoma HT1080 cells, and the apoptotic events were monitored by SERS spectral analysis. The decrease in the O-P-O stretching of the DNA backbone at $833cm^{-1}$ and the increase in the N 7-H vibration of adenine and guanine $(1450\text{-}1650 \text{ cm}^{-1})$ accounts for the single stand breakage of DNA upon photothermal chemotherapy, and the result was confirmed by the SERS analysis on isolated DNA from treated and un treated cells.

The fourth chapter of the thesis describes the construction of a targeted theranostic nano probe aiming to investigate synergistic photodynamic and photothermal therapy under single laser irradiation. The theranostic nanoprobe was able to detect exact location of breast tumour cells through targeting moiety i.e. monoclonal Her 2 antibody. Besides the fluorescence from the photosensitizer explored for the cell imaging, the target recognition of the nanoprobe was validated through SERS imaging. The conventional drawbacks of PDT using methylene blue (MB) as photosensitizer has been succeeded by encapsulating MB dimmers in CB [8] cavity. CB [8] acted as a rigid spacer Aligning GNRs end-to-end with a subnanometer distance between them for generating SERS hot spots. The designed nanoprobe exhibited excellent potential to perform in theranostic platform for efficient treatment in breast tumour cells under 808 nm laser irradiation.

In summary, we explored the high sensitivity, exceptional selectivity and excellent multiplexing ability of SERS as diagnostic modality. Significant modulations in diagnostic as well as theranostic aspects unfold a new avenue in realizing the potential of SERS in biomedical applications. The findings of this study will help towards construction of modern nanotheranostic platforms for efficient cancer treatment in clinics.

Chapter 1

An Introduction to Surface Enhanced Raman Scattering (SERS) Technique with Special Emphasis on Cancer Diagnosis and Treatment
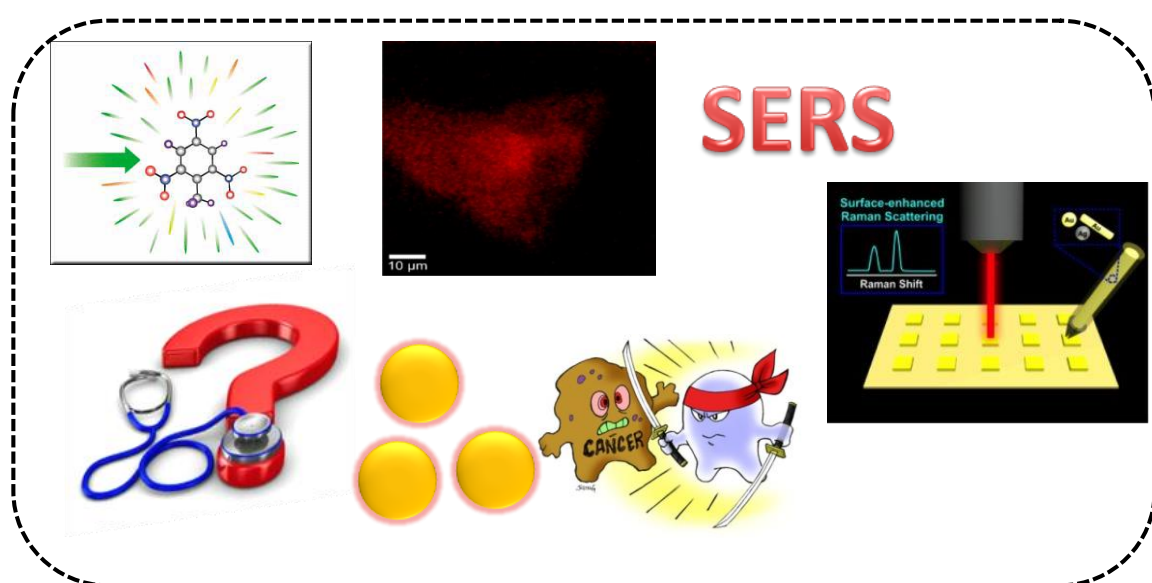
1.1. Abstract

Surface-enhanced Raman scattering (SERS) is an ultrasensitive vibrational spectroscopic technique to detect analytes even at single molecular level. The research on SERS has acquired great momentum due to its fingerprinting character and multiplexing ability. In recent years a great deal of attention has been paid for the development of targeted theranostic nanosystems utilizing SERS as one of the key diagnostic modalities. The present chapter gives an overview of the construction of SERS nanotags and its applications in cancer diagnosis and

theranostics. A few lines on the importance of monitoring therapeutic responses and combination of therapeutic strategies for cancer management are also included in the final part f the chapter.

1.2. Raman scattering

Scientific world witnessed tremendous advancements in the development of various spectroscopic tools during the last few decades. The 16th of March 1928 was a memorable day in the history of Indian science. It was on that day C.V Raman announced 'a new type of secondary radiation' observed by him to the world. The phenomenon attracted the attention of researchers all over the world and it became famous as 'Raman Effect'. The finger printing ability has transformed Raman scattering from an interesting observation to a powerful analytical tool. The dimension of research shifted from fundamentals to applications in diverse fields including analytical chemistry, chemical physics, solid state physics, biophysics and even medicine with enhanced interests. Investigation of scattered light up on interaction with matter to obtain the finger print of molecular vibration is the heart of Raman spectroscopy. Raman effect can be described in energy diagram as shown in **Figure 1.1**.[1] When a photon with energy *hv* interacts with molecule, the molecule will get excited to a virtual state. If the energy of excited photon is transferred to the molecule, stokes Raman scattering occurs. If energy is transferred from molecule to photon it is called anti-stokes Raman scattering. If there is no energy exchange then it is called Rayleigh scattering. Raman shift is the difference between incident and scattered frequencies and a typical Raman spectrum is a plot of intensity of the scattered

light in wave numbers relative to the incident laser excitation. Each chemical bond vibrates at a particular wavenumber and each molecule will have characteristic spectroscopic fingerprint.
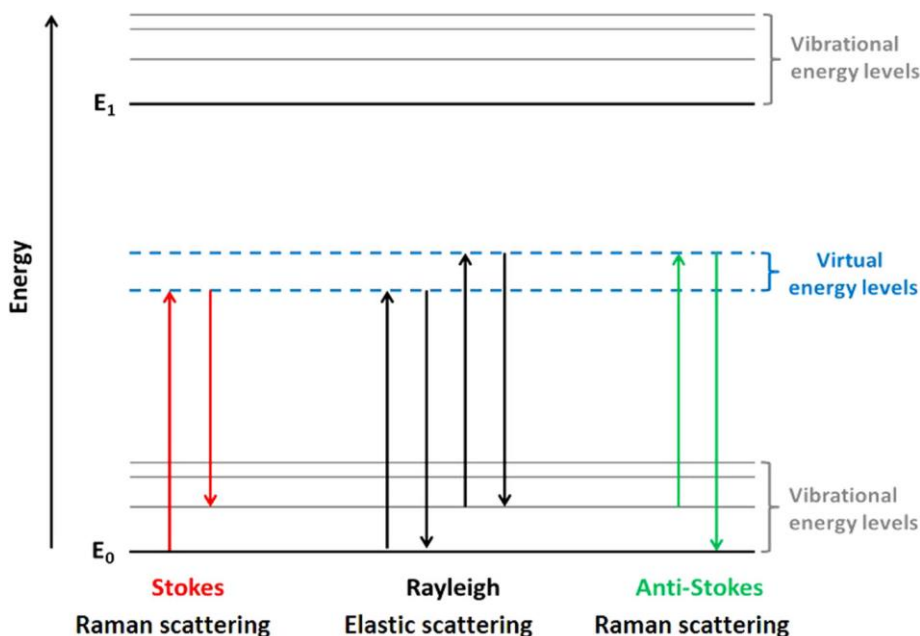
Figure1.1. "Jablonski" style diagram of energetic transitions involved in Raman scattering.[1]

Only one out off $\sim 10^8$ photons undergo Raman scattering.[2] Normal Raman scattering is very weak. So a large number of advanced versions of Raman spectroscopic techniques have been developed each with its own set of advantages and disadvantages.[3] This toolbox of Raman spectroscopic techniques with a brief description is summarized in **Table 1.1.**

1.3. Surface enhanced Raman scattering

The enhanced Raman signals from pyridine molecules on roughened silver film was observed by Fleischmann *et al*. in 1974[4], which led to the historical

development of an advanced version of Raman spectroscopy named as surface enhanced Raman spectroscopy (SERS).

Table 1.1. Summary of Raman spectroscopic techniques

Raman technique	Description	Advantages	Applications in biomedicine
Spontaneous Raman Spectroscopy	Detects intrinsic Raman scattering of molecules	Label free, non invasive and nondestructive	Diagnostics, guided surgery, molecular pathology, stem cell research
Resonance Raman Spectroscopy (RRS)	Excitation wavelength matches with electronic resonance of molecules	10^3–10^5 fold increase in signal to-noise ratio	Characterising specific biomolecules like carotenoids, cytochrome etc.
Surface Enhanced Raman Spectroscopy (SERS)	Raman signal is enhanced using roughened metal surface	10^6-fold increase in signal-to noise ratio	Cell based assays, immunoassays
Coherent Anti-Stokes Raman Spectroscopy (CARS)	Non-linear variants requiring pulsed	label free biomolecular imaging	Imaging specific molecules of interest like lipids, drugs

SERS was described as a new phenomenon with extraordinary enhancement of Raman signals from molecules that are in close proximity of metallic nanostructures. Since its discovery, the research in SERS has witnessed exponential growth over the past 44 years, benefitting from a series of discoveries, theories and technological advancements.

1.4. Fundamental theory of surface-enhanced Raman scattering

The mechanism of enhancement is primarily depending up on two main theoretical mechanism models, long-range electromagnetic (EM) enhancement and short-range chemical enhancement (CE). Collective oscillations of the NP's surface electrons designated as surface plasmon resonance (SPR) is initiated when noble metal nanoparticle surface is illuminated by incident light. When the frequency of incident light is in resonance with plasmon, the metal NP tuned in a dipolar field which is coherent with the exciting electric field. This process leads to a great enhancement of the EM field at specific positions around the NP called as "hot spots".[5] A molecule near to the hot spot experience much-enhanced electric field that excites its Raman mode. The scattered Raman signal will be further magnified in the same manner. EM enhancement is chemically nonselective as it provides the same enhancement for all molecules on or very close to the metal surface.

The EM enhancement mechanism can't absolutely explain the SERS phenomenon, therefore CE mechanism was proposed. These two key mechanisms together contribute to the total enhancement. CE deals with the interaction between chemisorbed molecules and metal surface which can be described in two ways. The first explanation is based on the development of charge-transfer intermediates that have higher Raman scattering cross sections compared to the analyte molecule. The other explanation is based on the charge transfer between a metal surface and analyte which generates Raman excitation

photons. Thus SERS signal intensity is highly reliant upon the interaction between adsorbed molecules and the surface of nanoparticles (NPs).

1.5. Direct versus indirect SERS identification

SERS based analysis can be performed either by directly collecting the signals that are characteristic of the target molecule (label free detection) or through indirect method.[6] Direct SERS analysis take an account of NPs whose surface has not been coated with a layer of stabilizing molecules. This method is extremely prevailing in the identification of analyte molecules with chemical structures rich in aromatic rings, double bonds, conjugated double bonds with heteroatoms and other functionalities. One of the main concerns of this approach is the aggregation of NPs on addition of molecules or even the analyte itself to the colloidal suspension. Owing to the complex biochemical composition of the specimen, the interpretation of SERS spectra is challenging and makes the direct identification of a particular biomolecule of interest, a trivial task.

On the other hand, indirect detection using SERS tags is a completely different approach which is appropriate for evaluation of highly complex cellular and tissue environments. SERS tags used for indirect analysis is a probe system constituted by metallic NPs and specific Raman reporter molecule, which can identify the presence and location of the target molecules and the traced SERS signal is realized from the Raman reporter (**Scheme 1.1**).[7]
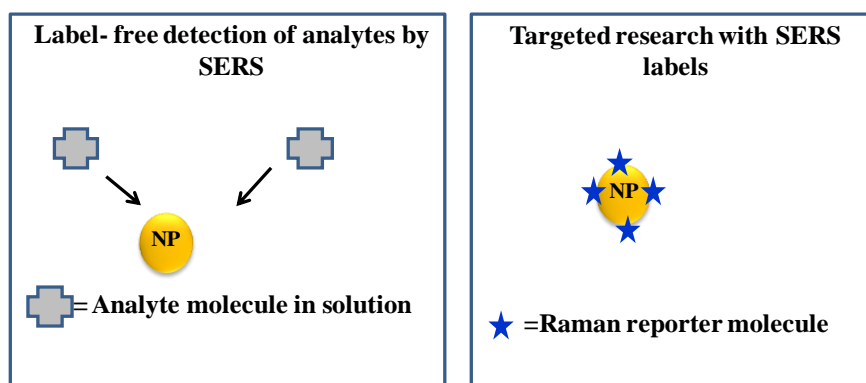
Scheme 1.1. Schematic representation of label free and label based SERS analysis

1.6. Synthesis of SERS Nanotags

SERS nanotags offer multiplexing capabilities, excellent signal specificity compared to other imaging modalities and high sensitivity (i.e. simultaneous identification of multiple targets). Other key advantages of SERS tags comprise of reduced toxicity, photostability and fingerprinting character. Moreover the narrow peaks originating from SERS tags are significantly appreciable than the broad, overlapping bands typical of fluorescence. The comparison between SERS tags, quantum dots, and conventional dyes is summarized in **Table1.2.**

Table 1.2. Comparison of SERS Tags, quantum dots, and conventional Dyes

Properties	SERS tags	Quantum dots	Conventional dyes
Physical principle	Raman scattering	Fluorescence emission	Electronic absorption/ fluorescence emission
Core composition	Au and Ag based NPs	CdSe and CdTe based NPs	Organic compounds
Size	~50 nm	~10 nm	~1 nm
Structural information	Fingerprint	Non fingerprint	Non fingerprint
Toxicity	Not toxic	Toxic	Toxic

The main components of SERS tags are 1) SERS substrates 2) Raman signature molecules (RSMs) 3) a stabilizing material and 4) a targeting moiety that will ensure selective binding of the tag to the specific target. Therefore the construction of SERS tags is a multistep process which requires intelligent fabrication strategies (**Figure 1.2**).

1.6.1. SERS substrates

Metal nanostructures can enhance Raman signals, and provide rigid foundations for engineering of SERS nanotags. The exceptional characteristics like low toxicity, air stability, ease of functionalization etc. made nanoformulations of gold (Au) and silver (Ag) as classic SERS substrates.[8] Further, the LSPRs of these materials extends over most of the visible and near infrared (NIR) wavelength range, where most Raman measurements are carried out which makes them suitable SERS substrates.[9] Representative nanosubstrates for SERS tags preparation are given in **Figure 1.3**.

1.6.1.1. Gold and Silver nanosphere

Gold and silver nanospheres are the most frequently used SERS substrates. Gold nanospheres are generally synthesized by the reduction of $HAuCl_4$ with citric acid as reported by Frens. Long-term stability, easily controlled size distribution, excellent biocompatibility etc. are some of the key advantages of gold nanospheres. Silver nanospheres are usually constructed by the reduction of silver nitrate ($AgNO_3$) either with hydroxylamine hydrochloride at room temperature or with sodium citrate in boiling condition. Compared to gold, silver is much more efficient SERS substrate which gives rise to Raman signal-enhancement of about

10 fold to 100 fold over similar gold nanostructures. On the other hand, silver nanospheres have poor biocompatibility, short-term stability and uncontrollable size distributions.
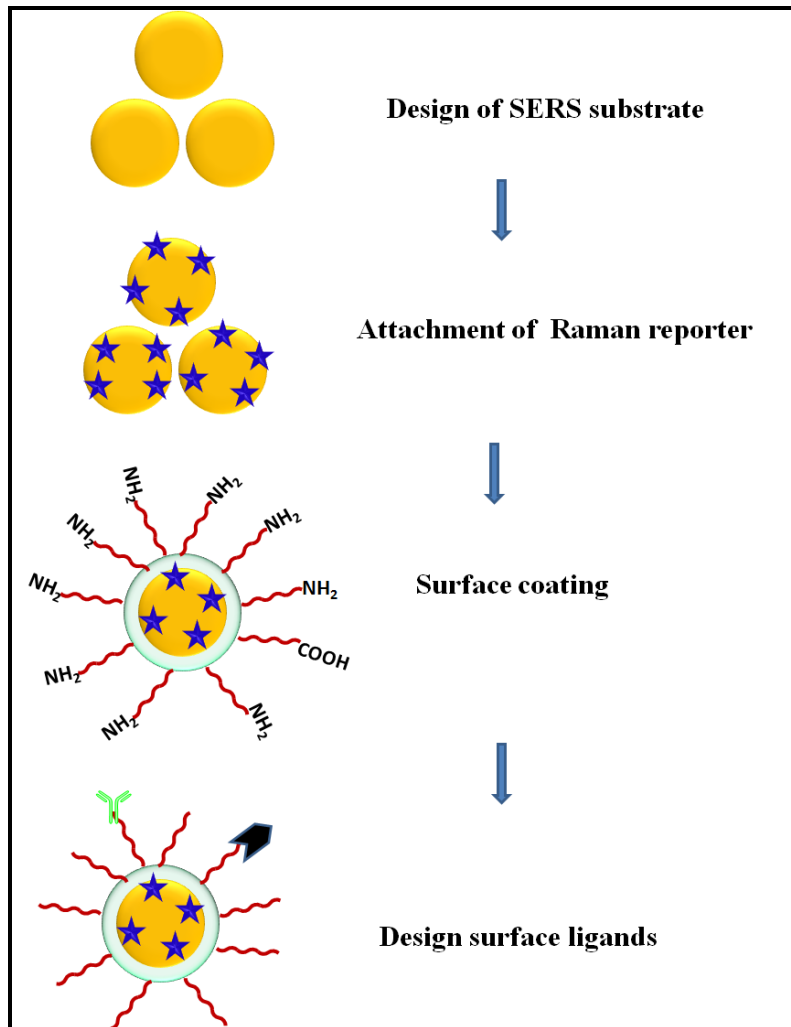
Figure 1.2. General steps and design criteria in engineering of SERS tags for biomedical applications.

1.6.1.2. Gold nanoshell

An assortment of metal nanoshell substrates comprising of silica-supported gold nanoshells, hollow gold nanoshells, and nanocages have been well explored.[10] These nanostructures possesses strong enhancement effects, sensitive

surface plasmon resonances (SPR) on the inner and outer shell radius and can be varied from the visible to the NIR region.[3]

1.6.1.3. Gold nanorod

Gold nanorods (GNRs) possess two SPR bands; a weak transverse band in the visible region that accounts for electron oscillation along the short axis and a strong longitudinal band in the longer wavelength region that represents electron oscillation along the long axis. The SPR of GNRs can be tuned by changing the aspect ratio further they have high theoretical permicrometer absorption coefficient compared to nanoshells. These peculiarities make GNRs as highly desirable Raman scattering substrates for biomedical applications, including *in vivo* cancer detection and imaging, and photothermal therapy (PTT).[11]

1.6.1.4. Multibranched metal nanoparticle

Multibranched plasmoic nanomaterials such as nanostars,[12,13] nanopopcorns, nanoflowers etc. are also well established SERS substrates holding exceptional SERS enhancement.[14] The number of RSMs that can be attached on multibranched NPs is higher than that of a sphere of equivalent size because of its higher surface area.

1.6.1.5. Gold−silver bimetallic nanoparticle

Au−Ag bimetallic NPs are another group of striking SERS substrates because of their composition-dependent physicochemical advantages.[15] Bimetallic Au@Ag core−shell NPs,[16] including Au@Ag nanosphers,[17] Au@Ag nanorods,[18]Au@Ag shells, and Au@Ag nanocages are fascinating group of

substrates synchronizing the higher SERS activity of silver and the homogeneous superiority of gold.

1.6.1.6. Nanoparticle cluster-based substrates

The strong EM field enhancements at the junctions between NP dimers and small clusters referred to as "Hot spots" are constructed by the mild aggregation of metallic NPs. The enhancement factor at hot spots is very high[19] and suitable for even single molecule detection.
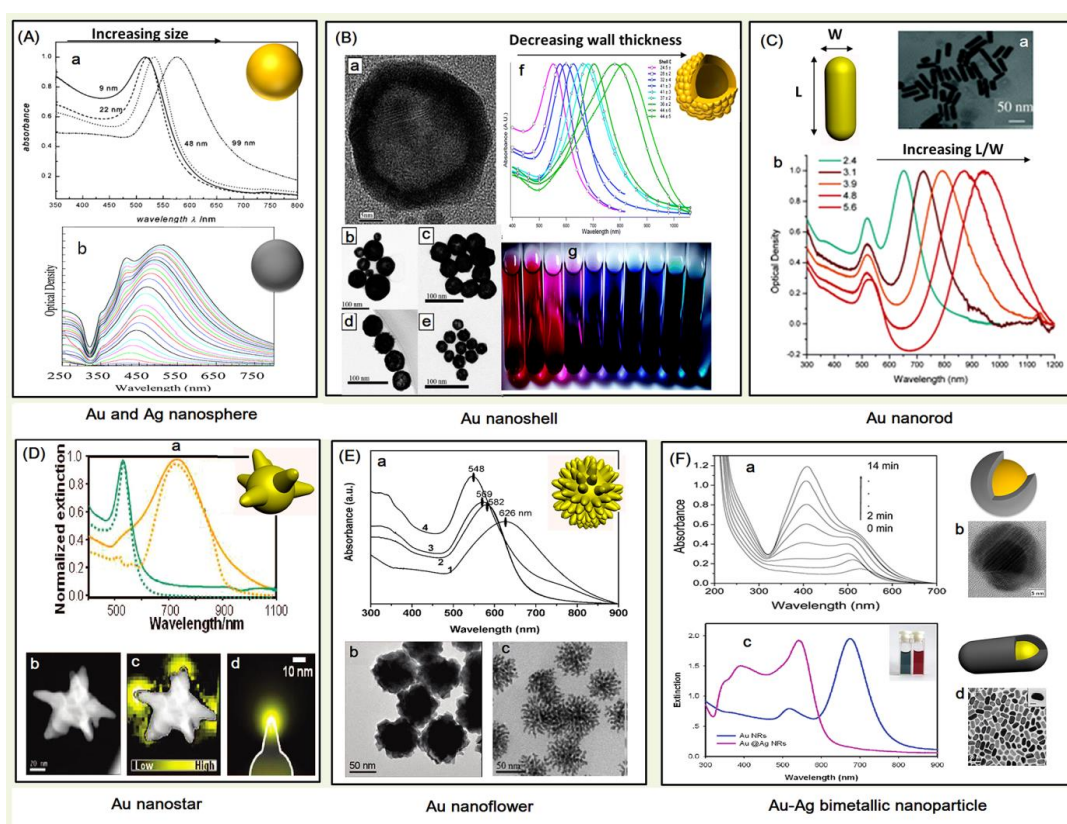
Figure 1.3 Representative nanosubstrates for synthesis of SERS tags[3]

1.6.2. Raman reporter molecules

Second step in the construction of SERS tags is the attachment of Raman reporter molecules with distinctive Raman spectral signature on SERS substrates. The interaction between the RSMs and metal substrate should be strong enough to prevent detachment during spectral evaluation. Nitrogen- or sulfur- containing

compounds are often employed as RSMs because of their high affinity to silver and gold. The reporter molecules should have a large Raman cross section. If the excitation-laser wavelength overlaps with the optical absorption of RSMs surface-enhanced resonance Raman scattering (SERRS) takes placewhich further increase the enhancement factor by 10^2 to10^3 folds. RSMs having nitrogen and sulfur are briefed in **Table 1.3.**

Table 1.3. Typical Raman Reporters Used for SERS Tag Preparation

Type	Example	Linking mode	Advantages	Disadvantages
Nitrogen-containing cationic dye	Crystal violet, Rhodamine B Rhodamine 6G, Nile blue	Electrostatic force, N−Au(Ag) interaction	Cheap, Large Raman cross section, Ready for SERRS	Weak affinity to metal, Weak signal stability,
Sulfur-containing dyes	3,3′-diethylthiadicarbo cyanine Iodide, malachite green isothiocyanate, tetramethylrhodamine-5-Isothiocyanate, rhodamine-5-(and-6)-isothiocyanate	S−Au(Ag) interaction	Strong binding affinity to metal, Suitable for further tag coating and modification, Ready forSERRS	Limited types, expensive
Thio-small molecules	4-aminothiophenol, 4-methylbenzenethiol, 2-naphthalenethiol, benzenethiol	S−Au(Ag) interaction	Cheap, strong binding affinity to metal,few Raman peaks is beneficial for multiplexing	Small Raman cross section, not ready for SERRS

1.6.3. Surface coating

Simple attachment of RSM on SERS substrates provides SERS signals which are often compromised by interfering molecules in the chemical or biological environment that are easily adsorbed on SERS substrates. In addition the RSM detachment from surface of SERS substrate is another concern. In order to address

12

these issues, an assortment of surface coating materials and encapsulation strategies were developed such as silica coating, biomolecule coating using bovine serum albumin (BSA), liposome coating, polymer coating with polyethylene glycol (PEG) etc. SH-PEG is a typical polymer coating as the pegylated NPs are not toxic and has a variable coating shell thickness, feeble affinity to interfering molecules, and exceptional *in vivo* biodistribution. Amphiphilic diblock copolymer, polystyrene block-poly(acrylic acid) was recently explored as a competent protecting material.[20] Liposomes are also unique protecting materials for NPs because of their capacity to self-assemble into ordered structures and intrinsic biocompatibility.[21] Silica coating ensures high stability, excellent water solubility, and simplicity of further modifications.[22,23] Recently Schlücker and co-workers reported a novel silica-coated nanotag with reproducible SERS signal based on self-assembled monolayer (SAM) of RSMs on the NPs.[24] In a similar report, poly(acrylic acid) was used to shield SAM reporter mlecule-covered Au nanoshells.[25]

1.6.4. Attachment of targeting molecules

SERS tags must be attached to antibodies, targeting peptide substrates, aptamers, or small-molecule ligands for specific recognition of biological targets. Stable covalent bonds can be made by carboxylic acid groups on the surface-coating molecules (such as BSA) and the amine groups in the antibody with the help of coupling reagents like 1-ethyl-3-(3-dimethylaminopropyl) carbodiimide (EDC) and N-hydroxysuccinimide (NHS). SERS tags functionalized with biotin are also

be used for coating as they can be easily attached to streptavidin-tagged biomolecules.

The assortment of SERS active platforms offers adequate choices for analyzing proteins, disease biomarkers, viruses, toxins, bacteria, cells and many more.[26–28] SERS tags are increasingly utilized in live-cell studies as they accomplish the requirements of live-cell imaging namely the exercise of low power lasers that can avoid light-induced damage of the cells, short data acquisition time, which enables dynamic and real-time monitoring of biological processes.

1.7.   SERS nanotags as diagnostic tool for tumor cell recognition both *in vitro* and *in vivo* detection

The diverse types and over-expression of cell surface receptors are generally considered as the manifestation of different diseases mainly cancer. Imaging of these cell-surface receptors with high specificity and sensitivity is a main road block in the diagnosis of this deadly disease. SERS nanotags have been successfully applied for specific recognition of cancer cells, multiplexed biomarker labeling, and real time monitoring of apoptotic processes.

Samanta and co-workers have designed a library of structurally modified tricarbocyanines with the aim to discover novel **SERRS** molecules for *in vivo* cancer detection. Eighty tricarbocyanine derivatives were prepared and termed as CyNAMLA library. The initial SERS screening made it clear that the intensities of CyNAMLA compounds varied considerably throughout the library, which indicated the dependence of SERS properties on the structure of RSM.

Nanoconstructs were constructed by conjugating two (human epidermal growth factor receptor-2) HER2-recognition motifs: a full anti-HER2 monoclonal and a single-chain variable fragment (scFv) anti-HER2 antibodies on BSA stabilized spherical gold nanoparticles (AuNPs) as illustrated in **Figure 1.4**.
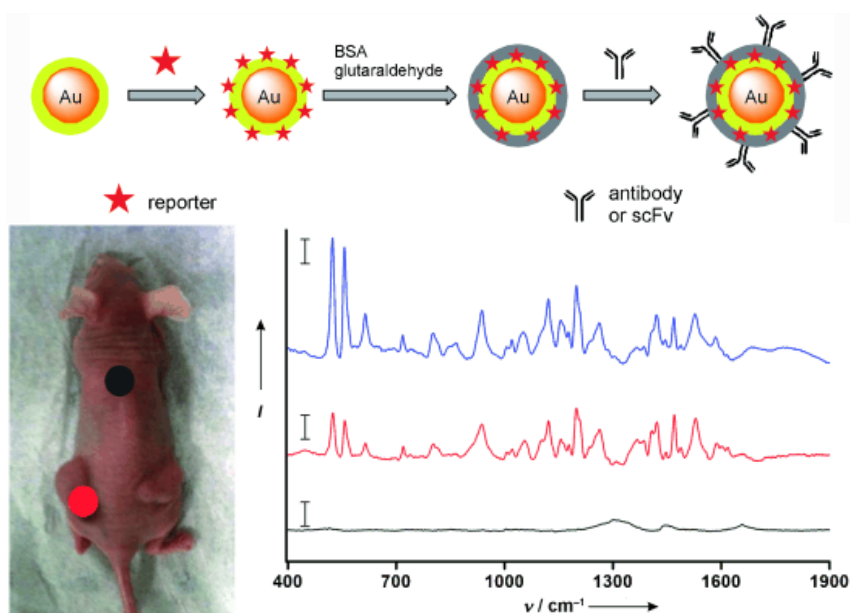
Figure 1.4. a) Construction of BSA-stabilized and antibody or scFv -conjugated SERS nanotags b) *In vivo* detection of HER2-positive tumors with scFv-conjugated SERS nanotags: SERS spectrum of pure nanotags (blue), and SERS signals of the tumor location (red) and an upper dorsal area (black).

SERS mapping on SKBR-3 cells after incubation with scFv-conjugated nanotag displayed high intensities. Further, the authors have injected the constructed nanotags into nude mice bearing xenografts produced from SKBR-3 cells. Five hours after the tail-vein injection, SERS spectrum at the tumor site through the skin was recorded and analyzed. The spectra of the tumor site absolutely matched the SERS spectra of the pure nanotag. The high sensitivity and tumor specificity of the nanotags confirms their outstanding potential as non-invasive diagnostic tools. [29]

The occurrence of circulating tumor cells (CTCs) indicates the incidence of a primary tumor or metastasis. The recognition of circulating breast cancer cells in blood by employing a combination of epithelial cell-specific antibody (epithelial cell adhesion molecule, anti-EpCAM)-attached magnetic nanoprobes and anti-HER2 antibody attached SERS tags was reported by Sha and co-workers.[30] Novel, standardized, no-wash assay platform was effected using nanoplex biotags in which magnetic beads were attached to anti-EpCAM and the SERS tags were conjugated to an anti-HER2 antibody to bind tumor cells for rapid and selective detection in human whole blood.
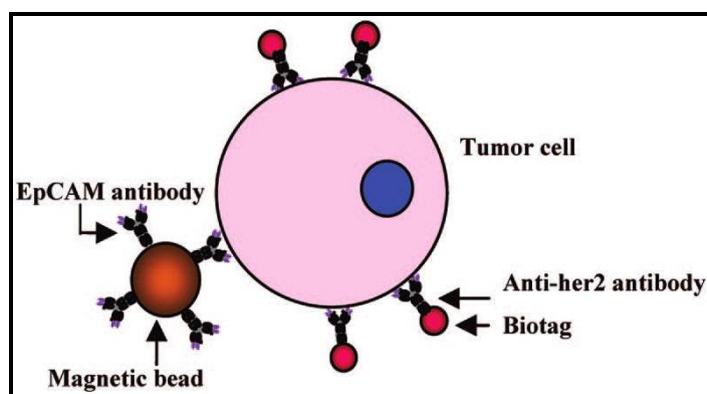
Scheme 1.2. Schematic illustration of the ternary immuno-complex formed by nanoplex biotags and magnetic bead conjugates binding to the model tumor cell.

As the breast cancer cell is of epithelial origin, the magnetic nanoprobes can selectively recognize these cells. Furthermore, as the HER2 receptor is over-expressed on the breast cancer cell surface, the SERS tags will specifically recognize these tumor cells. **Scheme 1.2** illustrates the concept in which magnetic beads conjugated to an epithelial cell specific antibody and the SERS tags conjugated to an anti-HER2 antibody bind to a tumor cell. Thus, by adding magnetic bead-EpCAM and SERS tag-HER2 conjugated to a patient's blood

sample, CTCs can be detected quickly with high sensitivity in presence of whole blood.

Signal enhancing techniques are required in order to detect CTCs since their concentration in blood is very low. Wu and co-workers proposed another novel SERS NP for the direct detection of CTCs in the blood. For obtaining the best possible signal intensity, differently shaped AuNPs were modified with a reporter molecule 4-mercaptobenzoic acid (4-MBA) as well as folic acid (FA) (**Scheme 1.3**).[31] The FA on the surface of NPs can recognize CTCs of ovarian, brain, kidney, breast, lung, cervical, and nasopharyngeal cancer, which over-express folate receptor alpha (FRα). Under optimized measuring conditions, CTCs were detected in blood without further enrichment.
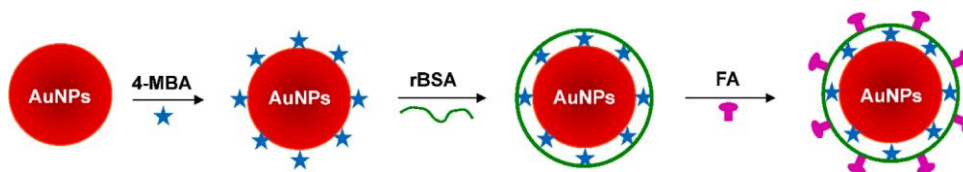
Scheme 1.3. Schematic Illustration for the Design of SERS Nanoparticles

Epidermal growth factor receptor (EGFR) has been recognized as an important prognostic marker expressed in cancer cells because its activation is associated with key features of cancer including tumor growth, survival, angiogenesis and metastasis. Cetuximab is the first monoclonal antibody drug that targets EGFR over-expressed in cancer cells. It easily binds to EGFR, thus down-regulating the receptor, blocking EGFR-mediated tyrosine kinase activity and inhibiting cellular proliferation. Thus, EGFR– cetuximab binding can be quantified to monitor receptor status and the prognosis of cancer therapy.

Recently, E. Chung *et al* reported SERS imaging to assess the inhibitory effect of cetuximab on EGFR expressed in cancer cells **(Scheme 1.4.)**. From SERS mapping images using silica-encapsulated gold nanotags, the localized spatial distribution of EGFR that was not inhibited by cetuximab was determined. Furthermore, EGFR expression was accurately quantified through the statistical analysis of SERS spectral data. The experimental data clearly demonstrated the feasibility of SERS imaging to improve the prognostic efficacy of cetuximab treatment.[32]
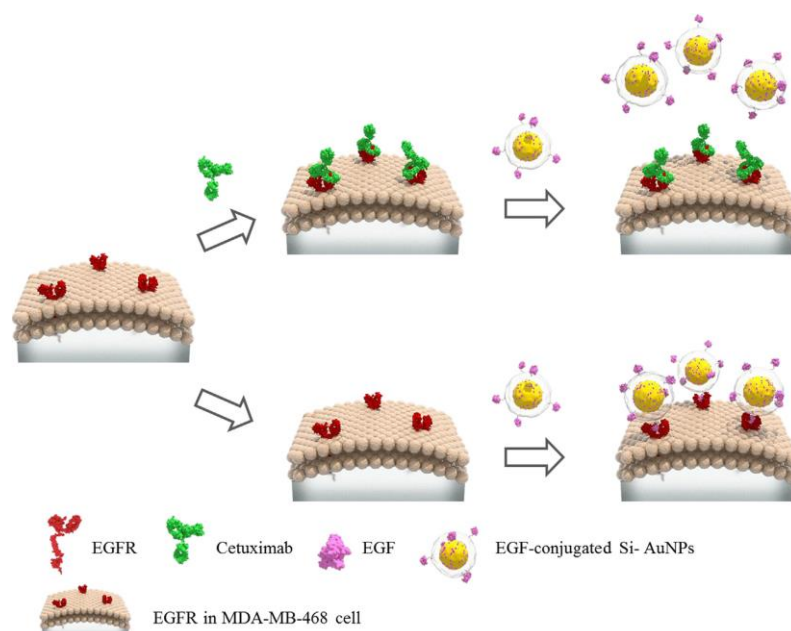
Scheme 1.4. EGFR detection using Si–AuNPs. After cetuximab treatment, EGF conjugated AuNPs cannot bind to EGFR on the membrane of MDA-MB-468 cells because of EGFR inhibition by cetuximab(top). EGF-conjugated AuNPs can efficiently bind to EGFR without cetuximab treatment (bottom).

Recently, L. Xiao *et.al* investigated expression, spatial distribution as well as the endocytosis of EGFR in single breast cancer cells using SERS.[33] By incubating anti-EGFR antibody conjugated GNRs with an EGFR-over-expressing cancer cell line, A431, EGFR localization was measured over time and found to be located

mostly at the cell surface. To further validate the constructed SERS probes they applied this SERS probes to detect the EGFR expression on breast cancer cells (MDA-MB-435, MDA-MB-231) and their counterpart cell lines in which EGFR expression was down-regulated by breast cancer metastasis suppressor 1 (BRMS1). The results showed that SERS method not only confirms immunoblot data measuring EGFR levels, but also adds new insights regarding EGFR localization and internalization in living cells which is impossible in immunoblot method. Thus SERS provides a new insight as a powerful tool to measure biomarkers in living cancer cells.

Zhong and co-workers reported a bifunctional nanocomposite probe for the detection of cancer biomarkers, demonstrating the viability of magnetic focusand SERS detection in a microfluidic platform.[34] The nanocomposite probe was composed of a magnetic nickel-iron core and a gold shell. Upon bioconjugation, the nanoprobes are magnetically focused on a specific spot in a microfluidic channel (**Figure 1.5**) enabling an enrichment of "hot spots" for SERS detection of the targeted carcinoembryonic antigen.
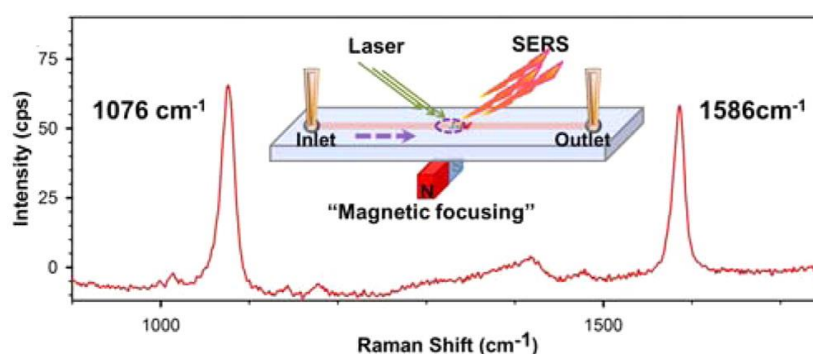
Figure 1.5. Illustration of magnetic focusing of bifunctional nanocomposite probe in a microfluidic channel.

Detection of hypersialylated tumors may be an efficient tactic to identify metastatic cancers because abnormal surface expression of sialic acid (hypersialylation) on tumors correlating with metastatic incidence and its involvement in tumorigenesis and progression is well known. Nagasaki and co-workers reported the application of phenylboronic acid-installed PEGylated AuNPs coupled with toluidine blue as SERS probes to target surface sialic acid.[35] Strong SERS signals from metastatic cancer cell lines (breast cancer; MDA-MB231) observed, contrary to non-metastatic MCF-7 cell. The detected SERS signals from various cancer cell lines correlated with their reported metastatic potential, implying that the developed SERS system was capable of distinguishing the metastaticity of cells.

Duan and co-workers reported the construction of bioconjugated plasmonic vesicles assembled from SERS-encoded amphiphilic AuNPs for cancer-targeted drug delivery.[36] The plasmonic assemblies with a hollow cavity played multifunctional roles as delivery carriers for anticancer drugs and SERS "ON/OFF" probe to recognize cancer cells and monitor intracellular drug delivery. The pH-responsive disruption of the plasmonic vesicle triggered intracellular drug release (**Figure 1.6**). The constructed plasmonic vesicle was envisioned to be a promising platform for targeted combination therapy by providing the chemotherapy with integrating PTT.

SERS has made significant advancement in cancer diagnosis *in vitro* and *in vivo*. Understanding various biochemical aspects of different cellular events can

enhance our knowledge about the cancer cell responses, and intern help to develop more efficient diagnostic and therapeutic progression in cancer cells and tumors.
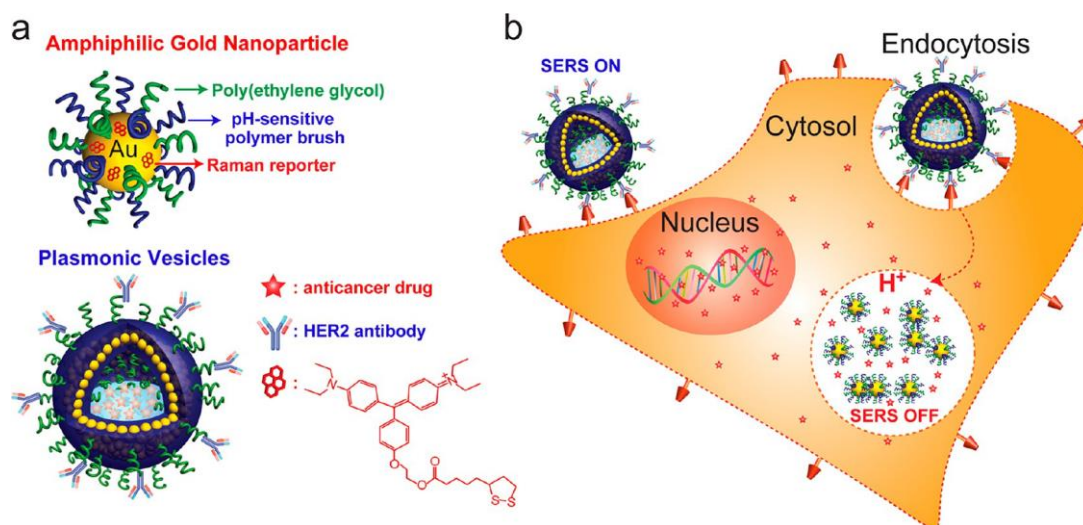
Scheme 1.6. a) Schematic illustration of the amphiphilic gold nanoparticle coated with Raman reporter b) The cellular binding, uptake, and intraorganelle disruption of the SERS-encoded pH-sensitive plasmonic vesicles

Though fluorescent probe-based techniques can be utilized for visualizing various cellular events, it is challenging to get the biochemical information on the whole process with this technique as the biomolecular modifications during cell cycle processes engage specific sensors for each enzymatic target. SERS is considered as a promising strategy for the investigation of live cells owing to its non-invasive nature and capable of providing fingerprint information on biomolecular components inside the cells.

1.8.   Tracing molecular snapshots of cellular process

Simultaneous visualization of various chemical and conformational modifications to the biomolecules involved in cellular processes is challenging due to its dynamic nature. El-Sayed and co-workers explored the plasmonically enhanced

light scattering properties of functionalized gold nanocubes (AuNCs) together with SERS to unravel the complex and dynamic biological processes involved in mitosis of healthy and cancerous cells from its molecular perspectives.[37] Relatively high rate of conversion of mitotic proteins from their α-helix structure to β-sheet conformation is possible in the cancer cells during meta-, ana-, and telophases. In the case of normal healthy cells, the existence of proteins in their β conformation was momentary and largely existed in the α-helix form. The chemical and conformational modifications of the proteins and lipids involved in mitosis were attained through this approach. New insights on the role of protein conformation dynamics during mitosis in the development of cancer and many other diseases is obtained through this approach.

Cellular apoptosis plays key roles in embryogenesis, aging, and various diseases. During apoptosis, cells endure a series of morphological and molecular events such as blebbing, cell shrinkage, proteolysis, and nuclear DNA fragmentation. Investigating these events on cellular level is vital for gaining complete understanding of the complicated mechanism of apoptosis. El-Sayed and co-workers monitored molecular events during apoptosis through SERS platform in real-time after the treatment with an apoptosis-inducing agent.[38] Spectroscopic investigation of the DNA/protein composition in the cell nucleus revealed the incidence and dynamics of three apoptotic molecular events: protein denaturation, proteolysis, and DNA fragmentation. DNA fragmentation in the form of DNA double-strand breaks (DSBs) was induced via UV irradiation in genomic DNA extracted from HSC-3 cells. The SERS spectra revealed pronounced bands at 730,

795, 838, 1239-1304, 1420-1480, and 1585 cm^{-1}, which were assigned to the nucleic acid adenine, cytosine, and thymine, O-P-O backbone, deoxynucleotides, C-H deformation of guanine and adenine and N$_7$-H stretch of guanine and adenine respectively. After UV exposure, the 838 cm^{-1} O-P-O backbone vibrations decreased while the 1585 cm^{-1} N$_7$-H vibration of guanine and adenine significantly increased as shown in **Figure 1.7**
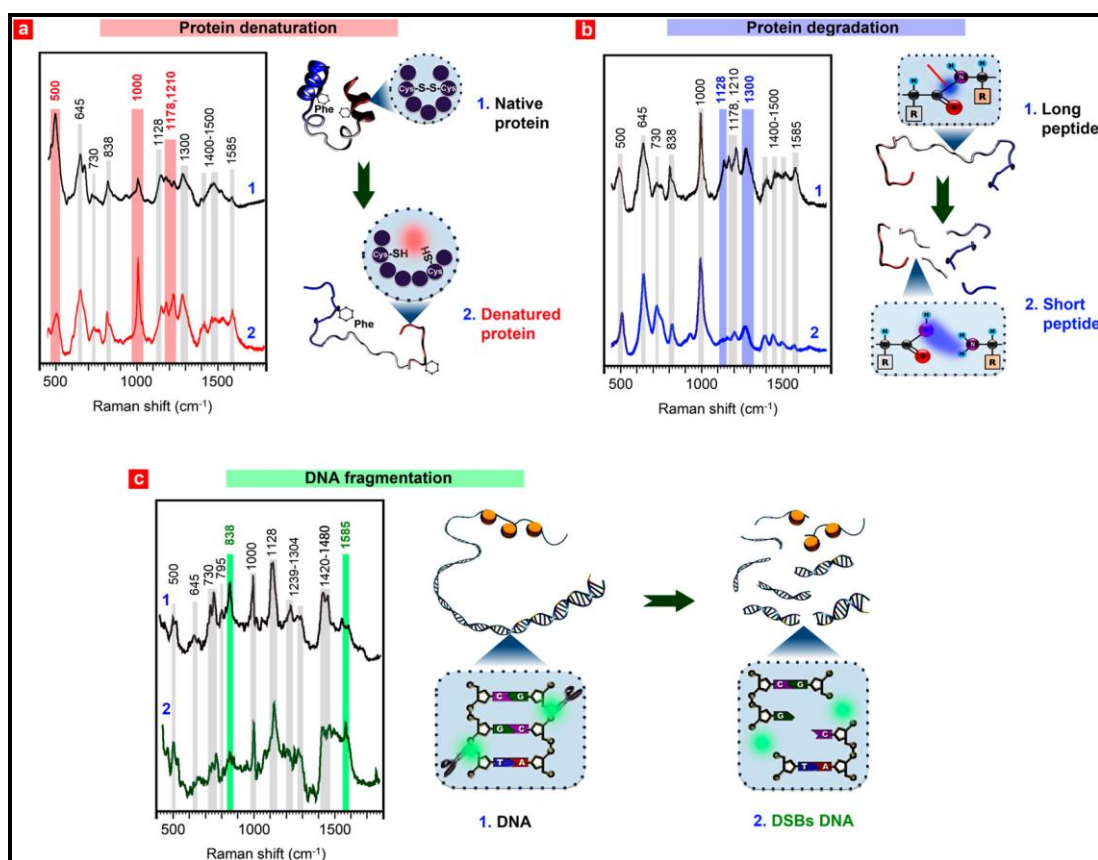
Figure 1.7. In situ reference spectra of apoptotic molecular events. (a) Protein denaturation : plasmonically enhanced Raman spectrum of highly ordered, folded proteins extracted from HSC-3 cells (top) and denatured proteins treated by β-mercaptoethanol (bottom). (b) Protein degradation: plasmonically enhanced Raman spectra of long, intact peptides (top) and short peptides treated by trypsin (bottom). (c) DNA fragmentation: plasmonically enhanced Raman spectra of undamaged, extracted DNA from cells (top) and damaged DNA in the form of double-strand breaks (DSBs) after 4 h treatment with UV light (bottom).

The current research endeavors in SERS are mainly focused on the development of theranostic agents, monitoring drug delivery, SERS guided surgery[39] etc.

1.9. SERS based theranostic platforms

Theranostic nanomedicine in which diagnostic and therapeutic functions are integrated into a single platform[40] has attracted increasing attention in recent years, because it offers great promises to provide personalized diagnostics and therapy with enhanced treatment efficacy and specificity. It provides an attractive means to improve cancer management by allowing tumor identification, real-time tracking of biodistribution, image-guided therapy and continuous monitoring of therapeutic responses. Owing to the unique characteristics of high sensitivity, fingerprinting nature, multiplexing capability and ultrafast detection SERS is effectively employed as an attractive tool for the construction of theranostic nanomedicine. SERS guided theranostic nanoplatforms based on intelligent construction of SERS tags have opened up new possibilities for spectroscopic detection and molecular imaging. In situ monitoring of drug release in cancer cells is a key factor for real-time assessment of drug release dynamics in chemotherapy. In situ monitoring of the intracellular anti-cancer drug delivery process was reported using SERS based biohybrid NPs.[41] The intracellular release of DOX from the biohybrid NP attached with HER2 antibody was continuously monitored by the time dependent changes in SERS signals of DOX internalized in breast cancer cells, SKBR-3.

In addition to monitoring the drug release in cancer cells, tracing the therapeutic responses ie, monitoring the molecular changes in cellular components with drug

treatment is also critical for the development of novel diagnostic strategies, and the improvement of the cancer therapeutic efficiency. A new strategy was proposed for *in situ* monitoring of the molecular changes of drug-treated cancer cell nuclei by combining dark-field and fluorescence co-imaging assisted by means of SERS. [42] Soma Gastric Cancer (SGC-7901) cell was treated with two model drugs, DNA binder (Hoechst33342) and doxorubicin (DOX) for the better understanding of the actual effect of drugs in molecular level. Nuclear targeting nanoprobes, NLS-PEG-GNRs with nuclear localizing signal peptides (NLS) around GNRs were prepared to achieve the amplified SERS signals of biomolecules to study the upshot of model drugs on main biomolecules in the cell nuclei (**Figure 1.8**). The results showed the great potential of this method to provide an improved understanding of the action effects of drugs.
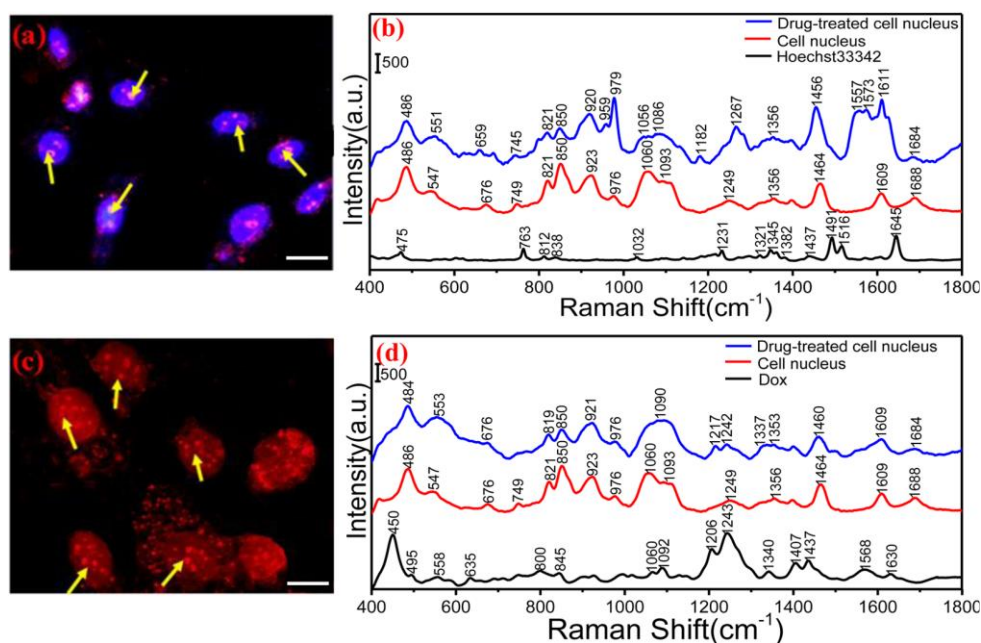
Figure 1.8. a,c) Dark-field/fluorescence coimages of SGC-7901 cells incubated with NLS-PEG-GNRs and then treated with Hoechst33342 and DOX, respectively; (b,d) Mean in situ SERS spectra of SGC-7901 cells before and after treatment with Hoechst33342 (10 μg/mL) and DOX (50 μM), respectively.

Wu and co-workers have reported Raman reporter 3,3′-diethylthiatricarbocyanine (DTTC)-coupled Ag core@Aushell nanostars (Ag@Au-DTTC) for NIR-triggered PTT and SERS imaging of breast cancers (**Figure 1.9.**). The cell viability of NPs was increased by coating Au nanostars onto AgNPs. The nanoconstruct exhibited high photostability and excellent photothermal conversion efficiency. The tumor volume of MCF-7 tumor-bearing nude mice injected with nanoconstruct and irradiated by an 808 nm laser was almost disappeared. This investigation demonstrated that the nanoconstruct is an excellent multifunctional agent for SERS imaging and NIR-triggered PTT of breast cancers.[43]
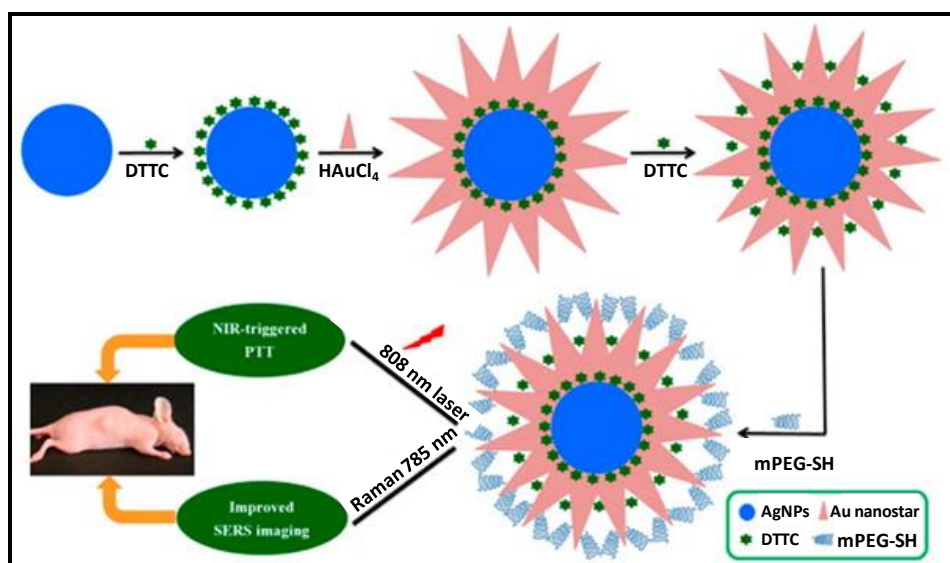
Figure 1.9. Scheme of Ag@Au-DTTC nanostars for *in vivo* improved SERS imaging and NIR-triggered PTT of breast cancers.

Gold coated fluorescent nano-mushrooms were fabricated as smart nanocarriers with high SERS enhancement for sequentially recognizing tumor cells, drug delivery, and real-time monitoring of biological responses.[44] The

surface-modified nano-mushrooms employed to target over-expressive glycoproteins (CD44) on the surfaces of cancer cells and release their loads via the cleavage of disulfide bonds in the cytoplasm. Raman mapping was used to demonstrate the nanoconstruct's superior biomolecule sensing ability.

A nanothermometer was fabricated by BSA stabilized gold nanostar-indocyanine green (ICG) nanoprobe to realize SERS imaging–based real-time sensitive monitoring of intracellular temperature in PTT (**Figure 1.10**). ICG can act as Raman reporter as well as a monitor of PTT in cells. The actively targeted nanotag induced SERS mapping-guided *in vitro* PTT of U87 glioma cells.[45]
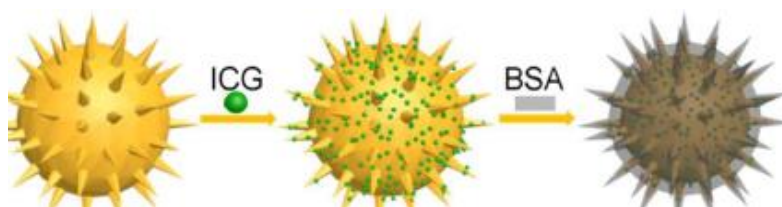
Figure 1.10. Schematic diagram of fabrication of nanothermometer.

Dinh and co-workers reported a unique quintuple-modality theranostic nanoprobe (QMT) with gold nanostars for SERS, magnetic resonance imaging (MRI), computed tomography (CT), two-photon luminescence (TPL) imaging and PTT.[46] The gold nanostars were tagged with a SERS reporter and linked with an MRI contrast agent Gd^{3+}. The results showed the potential of the nanoprobe for future imaging guided therapy applications.

Theranostic gold nanostar (GNS) probe was developed for multimodal imaging including SERS, CT, TPL, and PTT (**Figure 1.11.**). The potential of the probes for *in vitro* photothermal heating and *in vivo* photothermal ablation of primary sarcomas in mice was also demonstrated. The probe exhibited superior

photothermal conversion efficiency and potential to be used for *in vivo* biosensing and tracking using SERS, TPL, and CT at different spatial scales from whole body to the cellular level.[47]
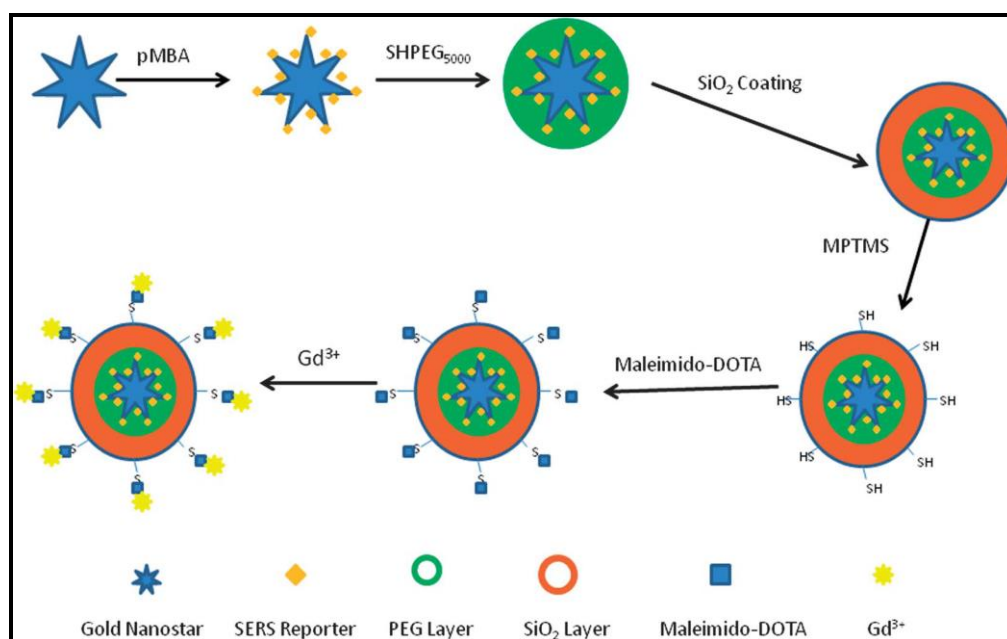
Figure 1.11. Schematic depicting the fabrication of the multifunctional QMT nanoprobe

Contag and co-workers reported the design and *in vivo* demonstration of a miniature, noncontact, opto-electro-mechanical Raman device as an accessory to clinical endoscopes that can provide multiplexed molecular data through a panel of SERS NPs.[48] Human and swine studies have demonstrated the potential of the devise for scanning of topologically complex luminal surfaces of hollow organs (e.g., colon and esophagus). The method offers excellent multiplexing potential by simultaneously detecting the unique spectral fingerprints of multiple SERS NPs and exhibits the capability to guide therapy by enabling sensitive quantitative molecular detection of small and otherwise hard-to-detect lesions.
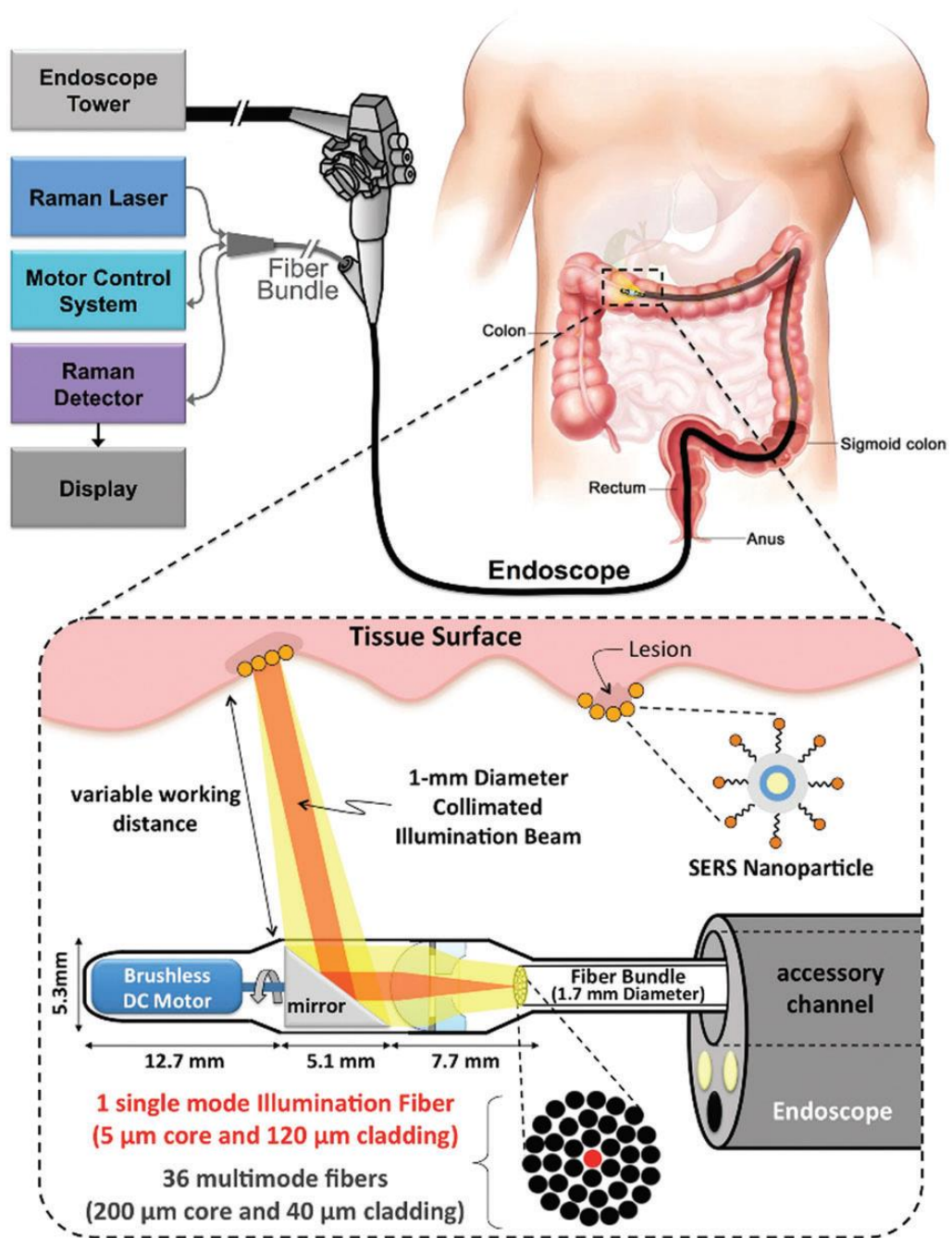
Figure 1.12. Schematic of Raman-imaging system being used in parallel with white-light endoscopy

It is to be noted that most of the well-known photosensitizers also possess reproducible and distinct Raman signatures and hence could be easily investigated in SERS theranostic platform.[49] A new type of 3D close-packed nanoassembly based on AuNPs loaded with methylene blue (MB) was explored in both Raman

and fluorescence lifetime imaging. A small population of MB molecules were located in very small areas between the aggregated NPs ("hot spots") to provide SERRS signal while the other population remains captured in Pluronic coating at a safer distance away from the nanosurface and preserves both its fluorescence signal and singlet-oxygen generation capability. Thus the nanoassemblies enabled the optical imaging of murine colon carcinoma cells (C-26) recording both Raman and fluorescence signals and enhanced photodynamic therapy (PDT).[50]

To enhance therapeutic efficacy, integrating SERS imaging function during PTT, has been accepted as a promising strategy[51] in cancer management due to its precise localization, and capability to trace therapeutic responses. PTT involves the rapid conversion of light into heat by plasmonic NPs[52] causing hyperthermia-induced cell death.[53] Zhou and co-workers reported gold nanobipyramids (Au NBPs) based SERS detection and PTT of MCF-7 cancer cells both *in vitro* and *in vivo* via bioconjugation with Raman reporter 2-naphthalenethiol (2-NAP) and FA. The bioconjugated Au NBPs exhibited enhanced Raman signal in MCF-7 tumor-bearing nude mice with high specificity and excellent photothermal performance in both *in vitro* and *in vivo* therapies.[54] Ray and co-workers demonstrated multifunctional nanotechnology-driven gold nanopopcorn based SERS assay for targeted sensing, nanotherapy treatment and in-situ monitoring of PTT response during the therapy process. In the presence of LNCaP human prostate cancer cell multifunctional popcorn shaped AuNPs generated several hot spots and provided a significant enhancement of the Raman signal intensity by several orders of magnitude. PTT induced irreparable cellular damage to the prostate cancer cell

(**Figure 1.13**). This was the first report on monitoring photo thermal nanotherapy response during therapy process through SERS intensity change. [55]
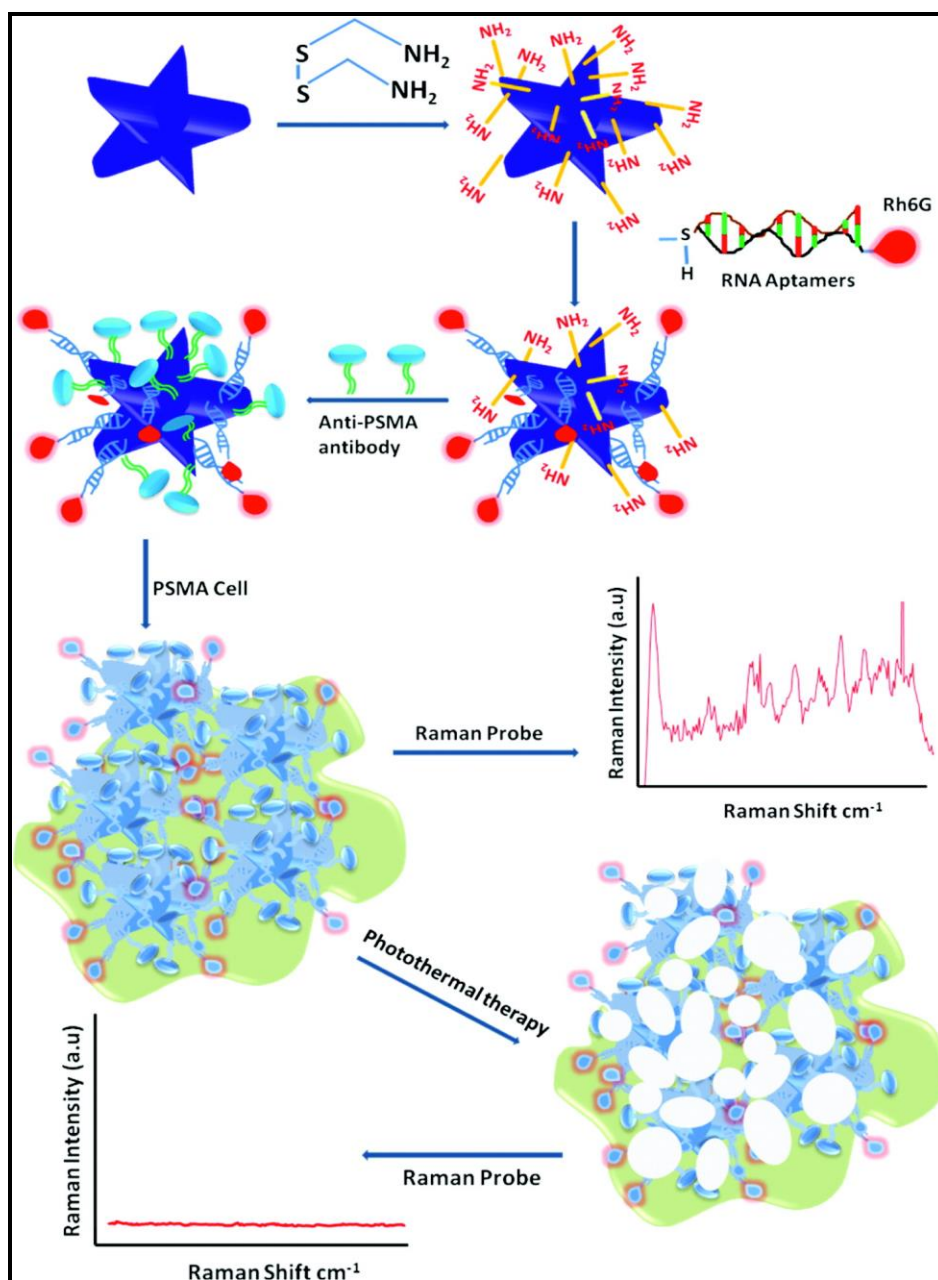
Figure 1.13. Schematic representation of the synthesis and working of aptamer-conjugated popcorn-shaped gold nanoparticles

El-Sayed and co-workers reported the use of actively targeted AuNPs, both to induce PTT cell death and to monitor the associated molecular changes through time-dependent SERS within a single cell. The changes caused by the heat

31

generated from the aggregated NPs absorbing NIR laser light caused modifications in the protein and lipid structures within the cell and ultimately led to cell death. The ability to trace PTT induced cell death in real-time will help to understand the molecular mechanisms involved in photothermal cancer cell death.[56]

An efficient theranostic system integrating Raman imaging and PDT effect was demonstrated by Dinh and co-workers. Well known photosensitizer protoporphyrin IX (PpIX) was loaded onto a Raman-labeled gold nanostar to make the nanoprobe (**Figure 1.14**). A cell-penetrating peptide trans-activating transcriptional activator (TAT) improved intracellular accumulation of the NPs. The nanoprobe was used for SERS imaging and PDT of BT-549 breast cancer cells. This was the first report which demonstrated the integration of SERS imaging and photosensitization from a theranostic nano construct.[57]
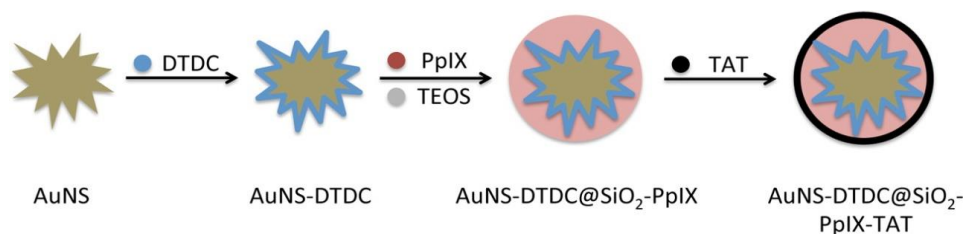
Figure 1.14 Schematic Depiction of the Nanocomposite Synthesis

McGoron and co-workers reported multifunctional silver nanoparticle-based system for cancer theranostics. The silver nanoparticles ware conjugated with a FA targeting ligand via an amide bond and also attached to the chemotherapeutic drug DOX via an acid-cleavable hydrazone bond. The silver nanoparticle carrier system exhibits PDT activity. pH triggered drug release and PDT contributes to

the increased therapeutic efficacy of this system. The multifunctional NPs can be probed intracellular region through SERS and fluorescence spectroscopy.[58]

Folate receptor (FR)-targeted theranostic nanoconstruct for SERS imaging and PDT was reported by Dinh and co-workers. Selective recognition of FR-positive cells was established using Raman imaging, exhibiting intense SERS signal from the FR-positive cells and little or no signal from the FR-negative cells. The results suggested that the gold nanostars coated with silica, and embedded with silver are a promising platform for the enhancement of future theranostic agents.[59]

A novel configuration to achieve *in vivo* multimodal tumor detection and PDT was demonstrated by He and co-workers. Two individual SERS and fluorescence "channels" were constructed by chemically doping SERS and fluorescence agents in different layers of a silica/polymer-coated GNR (**Figure 1.15**). Nanoconstruct intravenously injected into tumor-bearing mice accumulated inside the tumors allowing detection of the tumor by SERS and fluorescence measurements. Photosensitizer PpIX was also attached into the multilayered shell and PDT treatment was carried out right after the detection of the tumor.[60]
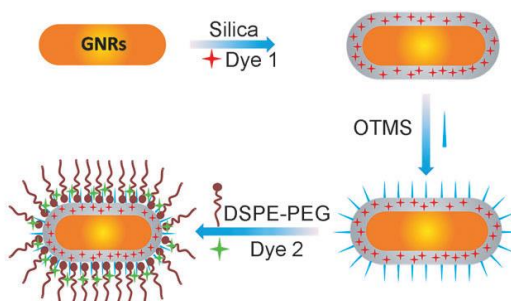
Figure 1.15. The synthesis procedures of Multifunctional GNR for SERS/ fluorescence integrated with PDT

Au core and graphene oxide nanocolloid (GON) shell for theranostic applications was reported by Min and co-workers (**Figure 1.16.**). The zinc phthalocyanine loaded core@shell NPs demonstrated excellent multifunctional properties for synergistic treatment of PTT and PDT in addition to Raman bioimaging with low cytotoxicity.[61]
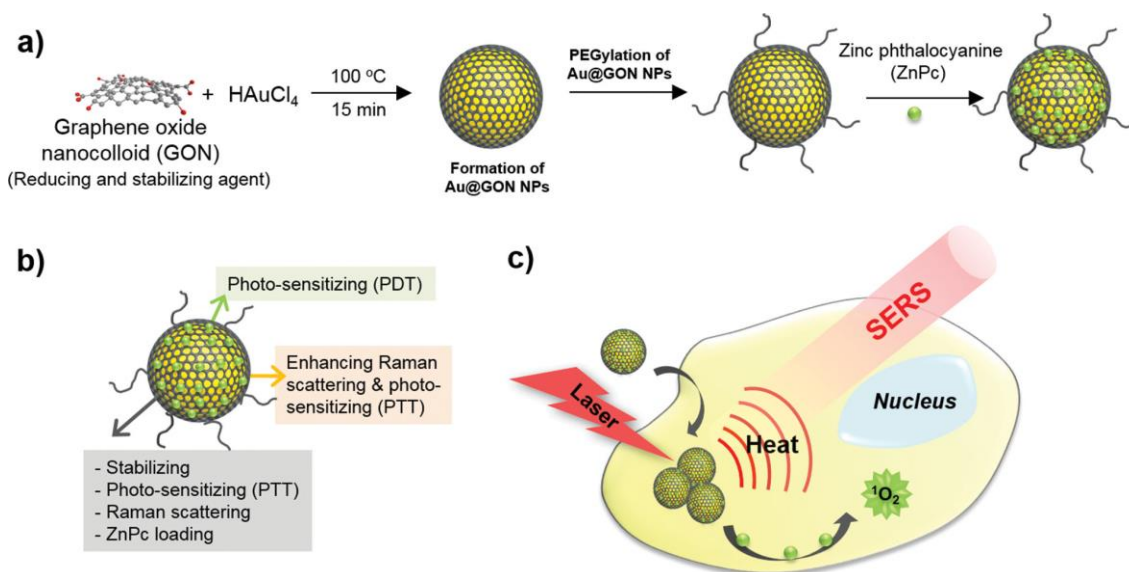
Figure 1.16. The synthetic procedure a), multifunctionality b) and theranosis process c) of core@shell nanoparticles.

SERS-based theranostic platforms have played a key role in the biomedical and clinical fields. SERS based multidisciplinary diagnoses and treatments have been employed to improve the efficacy of cancer therapy[62] by the monitoring of drug release as well as providing multimodal imaging and multifunctional capacity.[63] SERS with multiplex detection and multimodal imaging abilities holds high potential to be a promising tool for designing next generation surgical treatments.

1.10. Conclusion and present work

Raman spectroscopy has become an indispensable tool for the management of cancer right from early diagnosis up to monitoring the progress of therapeutic

responses. Owing to its unique advantages, SERS has been employed in elucidating the mechanisms associated with drug release and apoptosis on cancer cells. SERS guided fabrication of nanosystems for efficient drug loading and controlled and sustained release can be an effective tool for real time monitoring of the drug concentration to support and reduce the side effects of day to day chemotherapy. PTT assisted with SERS is an exceptionally promising technique in which temperature is increased around the nanostructures on laser irradiation. Squaraine dye aggregation that reflects on SERS intensity upon adsorption on nano-roughened gold surface is described in the second chapter. Nanotags conjugated with monoclonal antibodies specific to over-expressed receptors in cervical cancer cell, HeLa showed prominent SERS mapping intensity and selectivity towards cell surface and nucleus. The fast and accurate recognition obtained by antibody triggered SERS-nanotag has been compared with conventional time consuming immunocytochemistry technique. Development of a targeted theranostic nanoprobe capable of executing synergistic photothermal chemotherapy is described in chapter 3. Structural and functional variations of cellular components during cell death induced by targeted theranostic probe were effectively traced through SERS platform. Chapter 4 describes the development of targeted nanoprobe combining the photothermal treatment and photodynamic treatment in a single platform to further enhance the therapeutic efficiency for malignant carcinomas, because of the synergistic effects.

1.11.   References

(1)   Ember, K. J. I.; Hoeve, M. A.; McAughtrie, S. L.; Bergholt, M. S.; Dwyer, B. J.; Stevens, M. M.; Faulds, K.; Forbes, S. J.; Campbell, C. J. *npj Regen. Med.* **2017**, *2* (1), 12.

(2)   Pence, I.; Mahadevan-jansen, A. *Chem Soc Rev* **2016**, *45* (7), 1958.

(3)   Wang, Y.; Yan, B.; Chen, L. *Chem. Rev.* **2013**, *113* (3), 1391.

(4)   Moskovits, M. *Surf. Enhanc. Raman Scatt. Phys. Appl.* **2006**, *18*, 1.

(5)   Chen, H. Y.; Lin, M. H.; Wang, C. Y.; Chang, Y. M.; Gwo, S. *J. Am. Chem. Soc.* **2015**, *137* (42), 13698.

(6)   Cialla-May, D.; Zheng, X.-S.; Weber, K.; Popp, J. *Chem. Soc. Rev.* **2017**, *46* (13), 3945.

(7)   Fabris, L. *J. Opt.* **2015**, *17*, 114002.

(8)   Haynes, C. L.; Yonzon, C. R.; Zhang, X.; Van Duyne, R. P. *J. Raman Spectrosc.* **2005**, *36* (6–7), 471.

(9)   Sharma, B.; Frontiera, R. R.; Henry, A.-I.; Ringe, E.; Van Duyne, R. P. *Mater. Today* **2012**, *15* (1–2), 16.

(10)   Gao, Y.; Li, Y.; Wang, Y.; Chen, Y.; Gu, J.; Zhao, W. *Small* **2014**, *11*, 77.

(11)   Huang, X.; El-Sayed, I. H.; Qian, W.; El-Sayed, M. A. *J. Am. Chem. Soc.* **2006**, *128* (6), 2115.

(12)   Cao, X.; Shi, C.; Lu, W.; Zhao, H.; Wang, M.; Zhang, M.; Chen, X.; Dong, J.; Han, X.; Qian, W. *J. Nanosci. Nanotechnol.* **2016**, *16* (12), 12161.

(13)   Gao, Y.; Li, Y.; Chen, J.; Zhu, S.; Liu, X.; Zhou, L.; Shi, P.; Niu, D.; Gu, J.; Shi, J. *Biomaterials* **2015**, *60*, 31.

(14)   Fales, A. M.; Yuan, H.; Vo-Dinh, T. *Langmuir* **2011**, *27* (19), 12186.

(15)   Zhou, W.; Tian, Y. F.; Yin, B. C.; Ye, B. C. *Anal. Chem.* **2017**, *89* (11), 6120.

(16)   Fu, Q.; Liu, H. L.; Wu, Z.; Liu, A.; Yao, C.; Li, X.; Xiao, W.; Yu, S.; Luo, Z.; Tang, Y. *J. Nanobiotechnology* **2015**, *13* (1), 81.

(17)   Liu, K.; Bai, Y.; Zhang, L.; Yang, Z.; Fan, Q.; Zheng, H.; Yin, Y.; Gao, C. *Nano Lett.* **2016**, *16* (6), 3675.

(18)   Wu, L.; Wang, Z.; Zong, S.; Chen, H.; Wang, C.; Xu, S.; Cui, Y. *Analyst* **2013**, *138* (12), 3450.

(19)   Wang, A. X.; Kong, X. *Materials (Basel).* **2015**, *8* (6), 3024.

(20)   Yang, M.; Chen, T.; Lau, W. S.; Wang, Y.; Tang, Q.; Yang, Y.; Chen, H. *Small* **2009**, *5* (2), 198.

(21)   Ip, S.; MacLaughlin, C. M.; Gunari, N.; Walker, G. C. *Langmuir* **2011**, *27* (11), 7024.

(22)   Mulvaney, S. P.; Musick, M. D.; Keating, C. D.; Natan, M. J. *Langmuir* **2003**, *19* (11), 4784.

(23)   Brady, C. I.; Mack, N. H.; Brown, L. O.; Doorn, S. K. *Anal. Chem.* **2009**, *81* (17), 7181.

(24)   Küstner, B.; Gellner, M.; Schütz, M.; Schöppler, F.; Marx, A.; Ströbel, P.; Adam, P.; Schmuck, C.; Schlücker, S. *Angew. Chemie - Int. Ed.* **2009**, *48* (11), 1950.

(25)   Huang, J.; Kim, K. H.; Choi, N.; Chon, H.; Lee, S.; Choo, J. *Langmuir* **2011**, *27* (16), 10228.

(26) Cheng, Z.; Choi, N.; Wang, R.; Lee, S.; Moon, K. C.; Yoon, S. Y.; Chen, L.; Choo, J. *ACS Nano* **2017**, *11* (5), 4926.

(27) Han, X. X.; Huang, G. G.; Zhao, B.; Ozaki, Y. *Anal. Chem.* **2009**, *81* (9), 3329.

(28) Shanmukh, S.; Jones, L.; Driskell, J.; Zhao, Y.; Dluhy, R.; Tripp, R. A. *Nano Lett.* **2006**, *6* (11), 2630.

(29) Samanta, A.; Maiti, K. K.; Soh, K.-S.; Liao, X.; Vendrell, M.; Dinish, U. S.; Yun, S.-W.; Bhuvaneswari, R.; Kim, H.; Rautela, S.; Chung, J.; Olivo, M.; Chang, Y.-T. *Angew. Chemie Int. Ed.* **2011**, *50* (27), 6089.

(30) Sha, M. Y.; Xu, H.; Natan, M. J.; Cromer, R. *J. Am. Chem. Soc.* **2008**, *130* (51), 17214.

(31) Wu, X.; Luo, L.; Yang, S.; Ma, X.; Li, Y.; Dong, C.; Tian, Y.; Zhang, L.; Shen, Z.; Wu, A. *ACS Appl. Mater. Interfaces* **2015**, *7* (18), 9965.

(32) Chung, E.; Lee, J.; Yu, J.; Lee, S.; Kang, J. H.; Chung, I. Y.; Choo, J. *Biosens. Bioelectron.* **2014**, *60*, 358.

(33) Xiao, L.; Harihar, S.; Welch, D. R.; Zhou, A. *Anal. Chim. Acta* **2014**, *843*, 73.

(34) Li, J.; Skeete, Z.; Shan, S.; Yan, S.; Kurzatkowska, K.; Zhao, W.; Ngo, Q. M.; Holubovska, P.; Luo, J.; Hepel, M.; Zhong, C. J. *Anal. Chem.* **2015**, *87* (21), 10698.

(35) Shashni, B.; Horiguchi, Y.; Kurosu, K.; Furusho, H.; Nagasaki, Y. *Biomaterials* **2017**, *134*, 143.

(36) Song, J.; Zhou, J.; Duan, H. *J. Am. Chem. Soc.* **2012**, *134* (32), 13458.

(37) Panikkanvalappil, S. R.; Hira, S. M.; Mahmoud, M. A.; El-Sayed, M. A. *J. Am. Chem. Soc.* **2014**, *136* (45), 15961.

(38) Kang, B.; Austin, L. A.; El-Sayed, M. A. *ACS Nano* **2014**, *8* (5), 4883.

(39) Kircher, M. F.; Zerda, A. De; Jokerst, J. V; Zavaleta, C. L.; Kempen, P. J.; Mittra, E.; Pitter, K.; Huang, R.; Campos, C.; Habte, F.; Sinclair, R.; Brennan, C. W. *Nat. Med.* **2012**, *18* (5), 829.

(40) Kelkar, S. S.; Reineke, T. M. *Bioconjug. Chem.* **2011**, *22* (10), 1879.

(41) Hossain, M. K.; Cho, H.-Y.; Kim, K.-J.; Choi, J.-W. *Biosens. Bioelectron.* **2015**, *71*, 300.

(42) Liang, L.; Huang, D.; Wang, H.; Li, H.; Xu, S.; Chang, Y.; Li, H.; Yang, Y. W.; Liang, C.; Xu, W. *Anal. Chem.* **2015**, *87* (4), 2504.

(43) Zeng, L.; Pan, Y.; Wang, S.; Wang, X.; Zhao, X.; Ren, W.; Lu, G.; Wu, A. *ACS Appl. Mater. Interfaces* **2015**, *7* (30), 16781.

(44) Hsin-Yi, H.; Tsu-Wei, H.; Jian-Long, X.;Chung-Shi.; Y.; Chien-Cheng, C.; Chin-Chou, C.; Leu-Wei Lo.; Shenq-Hann, W.;Pen-Cheng, W.; Ching-Chang C.; Chau-Hwang, L.; Fan-Gang, T. *J. Mater. Chem* **2012**, *22* (155), 20918.

(45) Jing, C.; Zonghai, S.; Penghui, L.; Manxiang, W.; Nisi, Z. . X.-F.; .; Yuanwen, W.; Dehong, Hu.; Hairong, Z.; Guo, P. *Nanoscale* **2017**, *9*, 11888.

(46) Liu, Y.; Chang, Z.; Yuan, H.; Fales, A. M.; Vo-, T. *Nanoscale* **2013**, *5*, 12126.

(47) Liu, Y.; Ashton, J. R.; Moding, E. J.; Yuan, H.; Register, J. K.; Fales, A.

M.; Choi, J.; Whitley, M. J.; Zhao, X.; Qi, Y.; Ma, Y.; Vaidyanathan, G.; Zalutsky, M. R.; Kirsch, D. G.; Badea, C. T.; Vo-Dinh, T. *Theranostics* **2015**, *5* (9), 946.

(48) Garai, E.; Sensarn, S.; Zavaleta, C. L.; Loewke, N. O.; Rogalla, S.; Mandella, M. J.; Felt, S. A.; Friedland, S.; Liu, J. T. C.; Gambhir, S. S.; Contag, C. H. *PLoS One* **2015**, *10* (4), 1.

(49) Farhadi, A.; Roxin, Á.; Wilson, B. C.; Zheng, G. *Theranostics* **2015**, *5* (5), 469.

(50) Simon, T.; Potara, M.; Gabudean, A. M.; Licarete, E.; Banciu, M.; Astilean, S. *ACS Appl. Mater. Interfaces* **2015**, *7* (30), 16191.

(51) Aioub, M.; El-Sayed, M. A. *J. Am. Chem. Soc.* **2016**, *138* (4), 1258.

(52) Jain, P. K.; Huang, X.; El-sayed, I. H.; El-sayed, M. A. *Acc. Chem. Res.* **2008**, *41* (12), 7.

(53) Xie, W.; Schlücker, S. *Reports Prog. Phys.* **2014**, *77* (11), 116502.

(54) Feng, J.; Chen, L.; Xia, Y.; Xing, J.; Li, Z.; Qian, Q.; Wang, Y.; Wu, A.; Zeng, L.; Zhou, Y. *ACS Biomater. Sci. Eng.* **2017**, *3* (4), 608.

(55) Lu, W.; Singh, A. K.; Khan, S. A.; Senapati, D.; Yu, H.; Ray, P. C. **2011**, *132* (51), 18103.

(56) Aioub, M.; El-Sayed, M. A. *J. Am. Chem. Soc.* **2016**, *138* (4), 1258.

(57) Fales, A. M.; Yuan, H.; Vo-Dinh, T. *Mol. Pharm.* **2013**, *10* (6), 2291.

(58) Srinivasan, S.; Bhardwaj, V.; Nagasetti, A.; Fernandez-Fernandez, A.; McGoron, A. J. *J. Biomed. Nanotechnol.* **2016**, *12* (12), 2202.

(59) Fales, A. M.; Crawford, B. M.; Vo-Dinh, T. *ACS Omega* **2016**, *1* (4), 730.

(60)   Zhang, Y.; Qian, J.; Wang, D.; Wang, Y.; He, S. *Angew. Chemie - Int. Ed.* **2013**, *52* (4), 1148.

(61)   Kim, Y. K.; Na, H. K.; Kim, S.; Jang, H.; Chang, S. J.; Min, D. H. *Small* **2015**, *11* (21), 2527.

(62)   Zhang, W.; Wang, Y.; Sun, X.; Wang, W.; Chen, L. *Nanoscale* **2014**, *6*, 14514.

(63)   Deng, L.; Li, Q.; Yang, Y.; Omar, H.; Tang, N.; Zhang, J.; Nie, Z.; Khashab, N. M. *Chem. - A Eur. J.* **2015**, *21* (48), 17274.

Chapter 2

Aggregation Induced Raman scattering of Squaraine Dye: Fabrication of SERS Nanotag in Diagnosis of Cervical Cancer Dysplasia by Raman Imaging
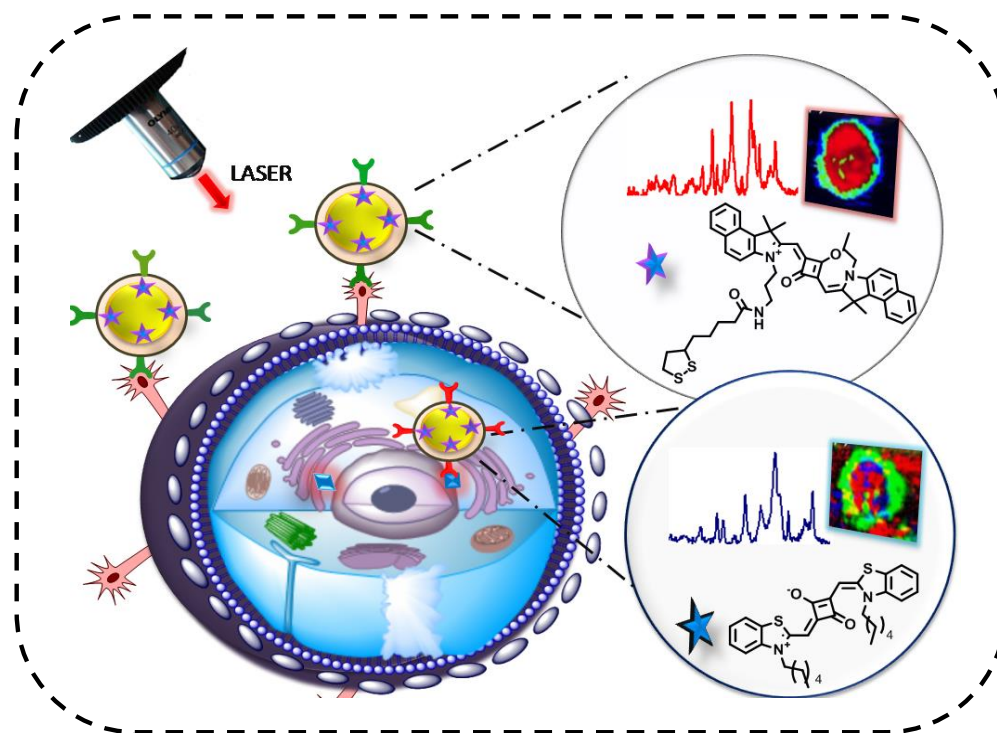
2.1 Abstract

The extent of squaraine dye aggregation which is reflected on SERS intensity upon adsorption on nano-roughened gold surface is described in this chapter. We have synthesized a series of six squaraine dyes consisting of two different electron donor moiety i.e. 1, 1, 2-trimethyl-1H-benzo[e]indole and 2-methylbenzo[d]thiazole which modulates the chemisorptions and hydrophobicity being designated as SQ1,

SQ2, SQ3, SQ4, SQ5 and SQ6. SQ2 (mono lipoic acid appended), SQ5 and SQ6 (conjugated with hexyl and dodecyl side chain) squaraine derivatives having more tendency of aggregation in Dimethyl sulfoxide (DMSO)-water mixed solvent system showed significant increase of Raman scattering in the fingerprint region when chemisorbed on spherical gold nanoparticles (AuNPs). Two sets of SERS nanotags were prepared with colloidal AuNPs (size: ~ 40-45nm) by incorporating Raman reporters SQ2 and SQ5 followed by thiolated Polyethylene glycol (PEG) encapsulation (SH-PEG, SH-PEG-COOH) denoted as AuNPs-SQ2-PEG and AuNPs-SQ5- PEG. Further conjugation of these nanotags with monoclonal antibodies specific to over expressed receptors, EGFR and p16/Ki-67 in cervical cancer cell, HeLa showed prominent SERS mapping intensity and selectivity towards EGFR on cell surface and p16/Ki-67 in nucleus. The fast and accurate recognition obtained by antibody triggered SERS-nanotag has been compared with conventional time consuming immunocytochemistry technique.

2.2 Introduction

The field of bioimaging attracts the interest of a vast scientific community as it provides extensive opportunities for early detection of deadly diseases and helps the facile monitoring of treatment efficacy in time.[1] Fluorescence imaging is one of the most versatile and widely used conventional imaging techniques in clinical practice and biomedical research.[2] Although extraordinary contrast and specificity provided by fluorescence imaging technique is greatly appreciated, there exists some intrinsic

limitations such as tissue absorption, scattering and autofluorescence.[3] Intense efforts are progressing to detect minute changes in the spectra of cells and tissues with abnormality and to develop medically approved methods which has superiority over classical diagnostic tools.[4-6] In this regard, application of Raman spectroscopy in biomedical field specially diagnosing infected cells, tissues and many bioanalytes is an emerging area of research which assure the accurate investigation by spectral cytopathology and spectral histopathology. In the present decade, SERS technique aroused as an active future competitor against fluorescence-based detection and imaging. [7-8] Raman fingerprints of the molecules consists of sharp peaks in contrast to the broad bands of fluorescent emission, allowing simultaneous multiplexed detection of a number of analytes or labels. SERS signal intensity of molecular vibration gets enhanced up to 10^8–10^{14} folds compared to simple Raman spectra when Raman active molecules are in close proximity to metallic nanoparticles like gold or silver.[9-10] Crystal Violet (CV), [11] malachite green isothiocyanate (MGITC),[12-13] 4-mercaptobenzoic acid (4-MBA),[14] Rhodamine 6G,[15] diethylthiatricarbocyanine (DTTC), [16] are some of the frequently used Raman reporter molecules.[17] Very few reporters are available which have been designed rationally and screened their Raman intensity for multiplexing detection in SERS platform.[18] In recent years Chang's group developed NIR Raman reporters with cyanine core through a solid phase library synthesis.[19-20] The significant Raman scattering of squaraine dyes in the fingerprint region have already been investigated.[21] Squaraines is a group of fascinating organic dyes, having resonance stabilized 1, 3-zwtitterionic donor–

acceptor–donor structure as the backbone with the central acceptor squaryl ring bound by donor aromatic rings on either side. It possesses a high extinction coefficient, intense fluorescence[22] and good photoconductivity. These features make them useful for a variety of applications in areas spanning from materials science to biology and medicine. Moreover, squaraine dyes are applied in photoconductive materials, organic solar cells,[23-25] light emitting field-effect transistors,[26] as active media for fluorescence patterning [27] and fluorescent probes and labels. However, in general it has the tendency to form aggregates under aqueous conditions which restricts their use in bioimaging due to the strong fluorescence quenching.[28-29] Several reports are available on the effect of SERS substrate aggregation influencing the SERS signal intensity but the reports on the influence of aggregation of reporter molecules on Raman signal intensity are rarely found so far.[30-31] In the present study, we revealed the aggregation property of a series of squaraine dyes which promotes them as effective Raman reporters by predicting their SERS signal intensity. We have synthesized six squaraine dyes from two types of donor moiety i.e., 1, 1, 2-trimethyl-1H-benzo[e]indole and 2-methylbenzo[d]thiazole designated as SQ1 to SQ6. Extensive photophysical studies including solvent dependent aggregation have been encountered. Based on the higher aggregation properties in DMSO-water system, SERS screening and nanotag preparation with AuNPs have been processed with SQ2 and SQ5 in order to evaluate the SERS signal intensity and multiplexing peak pattern. Further we have utilized the constructed SERS nanotags for detection and imaging of cervical precancerous conditions by tagging monoclonal antibody p16/Ki-67 and

EGFR. Conventional methods like immunocytochemistry have been utilized for long time in cancer detection.[32] Recently Nicolas et al reported that usage of p16/Ki-67 immunostaining kit is a sensitive method for the early detection of cervical cancer lesions[33] and its use increase the interest of many pathologists compared to human papillomavirus (HPV) testing and p16 single stain cytology.[34-37] Similarly, EGFR receptor is a biomarker which is over expressed in most of the cervical precancerous lesions. As immunocytochemistry is subjective, time consuming and requires trained cytotechnologists, novel approaches are essential to overcome the drawbacks of the cytologic diagnosis for clinically significant lesions. As a new insight the detection platform between dual antibodies conjugated SERS-nanotag (p16/Ki-67andEGFR) is compared with the conventional immunocytochemistry technique.

2.3. Results and Discussion

2.3.1. Synthesis of squaraine dyes

The synthesis of six squaraine dyes, SQ1 to SQ6 is based on the standard donor–acceptor strategy. [38] In brief, condensation reaction of a mixture of squaric acid and corresponding donor moiety in toluene–butanol eutectic mixture with continuous removal of water using Dean Stark apparatus afforded the squaraine dye in moderate to good yield. Synthetic route towards squaraine dyes are depicted in **Scheme 2.1** and the detailed characterization of squaraine dyes has been carried out through ^{1}H NMR, HR-MS analysis.
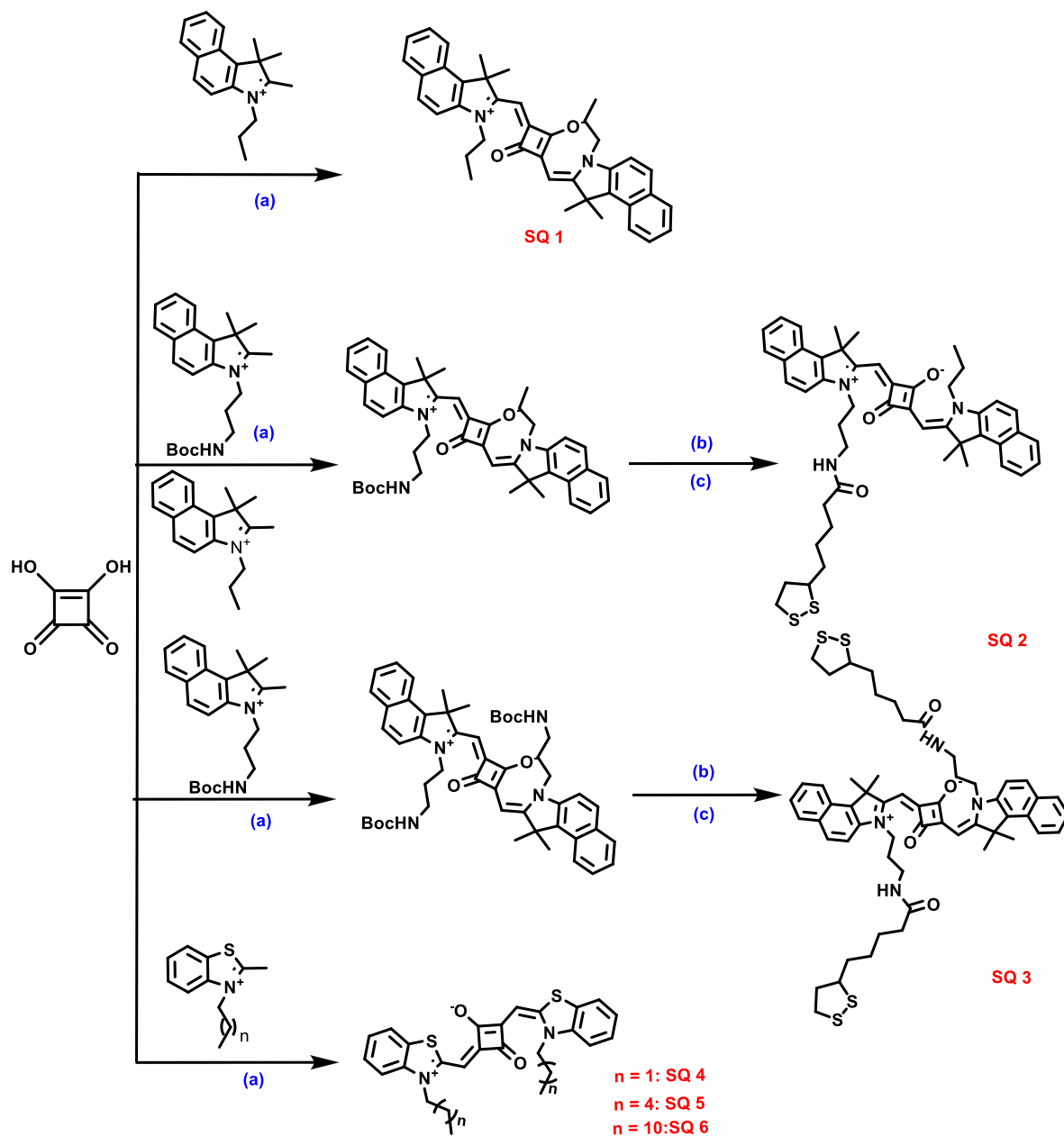
Scheme 2.1. General synthetic route of the squaraine dyes, SQ1–SQ6. (a) Dry toluene–butanol (1:4), 12h, Reflux; (b) DCM, 20%TFA, 3h; (c) lipoic acid succinimidylester, TEA, DCM, 12h.

The core structure of SQ1–SQ3 is constituted by 1, 1, 2-trimethyl-1H-benzo[e] indole moiety and that of SQ4–SQ6 is constituted by benzothiazole moiety. The basic design of SQ1–SQ3 varies in the number of attached lipoic acid units imparting the

48

degree of chemisorption while SQ4–SQ6 varies in the alkyl chain length enhancing the hydrophobicity.

2.3.2. Photophysical properties of squaraine dyes

2.3.2.1. Absorption and Emission Spectral Properties

All the synthesized squaraine dyes showed absorption maxima around 671 nm with high molar extinction coefficient.
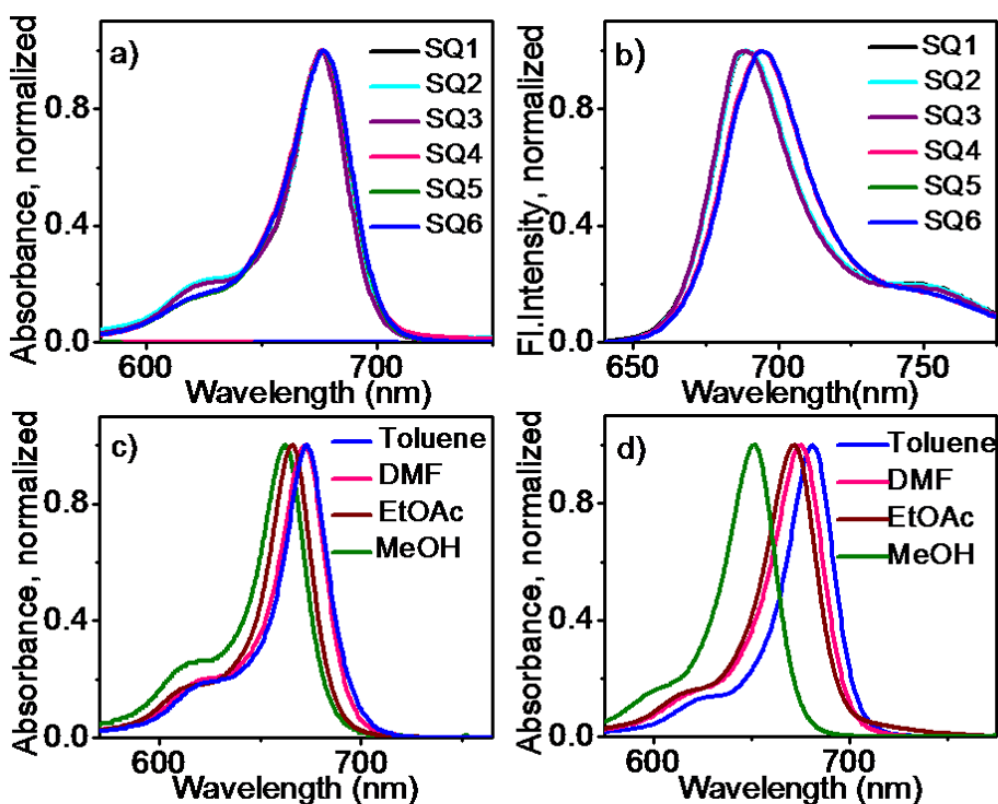
Figure 2.1. Normalized absorption (a) and emission (b) spectra of SQ1-6 in DMSO. Solvent dependent absorption spectra of SQ2 (c) and SQ5 (d) in toluene, DMF, EtOAc, MeOH.

The emission maxima of SQ1, SQ2 and SQ3 are centered at 689 nm and that of SQ4, SQ5 and SQ6 are centered at 694 nm. The normalized absorption and emission spectra of all dyes in DMSO are shown in **Figure 2.1 (a & b)**. The UV–

visible absorption spectra of SQ2 and SQ5 in toluene, DMF, ethylacetate and methanol showed almost similar spectral shape **(Figure 2.1 c &d).** With increase of solvent polarity, there is a blue shift which is attributed to difference in extent of stabilization of molecular orbital by different solvents. The details of photophysical properties are summarized in **table 2.1**

Table 2.1. Photophysical properties of the SQ1-SQ6

Squaraine dyes	λ_{abs} (nm)	ε_{max} ($M^{-1}cm^{-1}$)	λ_{em} (nm)	Φ_F
SQ1	675	2.1×10^5	689	0.22
SQ2	675	1.6×10^5	689	0.22
SQ3	676	1.8×10^5	689	0.15
SQ4	676	2.7×10^5	694	0.11
SQ5	676	2.5×10^5	694	0.36
SQ6	676	2.6×10^5	694	0.42

[*]Average of more than three independent experiments

2.3.2.2. Aggregation in solution

Squaraines have tendency to form both H-and J-aggregates in solution.[39] The monomer and aggregate bands can be clearly distinguished from absorption and emission spectral behavior. In ideal J aggregates, the molecular planes are stacked

side by side whereas for ideal H-aggregates molecular planes are face to face, i.e. α is 90°. On the basis of exciton coupling theory, J-aggregates exhibit red-shifted narrow bands and H-aggregates would have blue- shifted broad bands. In order to study the aggregation behavior of squaraine dyes, absorption spectra of squaraine dyes were measured in DMSO by varying the dye concentration. No change in position or shape of the spectrum with increasing dye concentration was observed **(Figure. 2.2).**
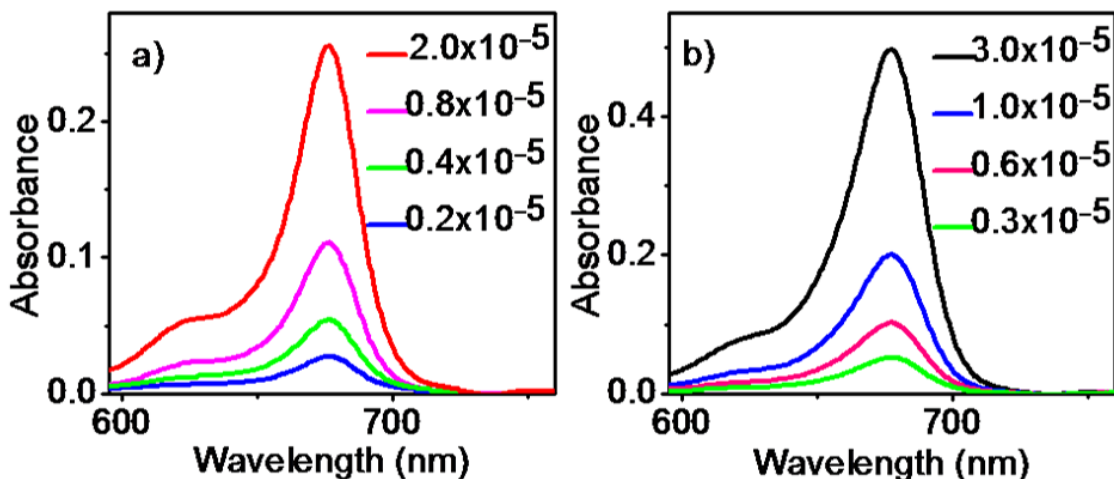
Figure 2.2. Absorption spectra of SQ2 and SQ5 in DMSO at various dye concentration. (Dye concentration (M) is shown in color bar).

This provides clear evidence for the lack of aggregate formation in DMSO even at excess dye concentration. Hence all the squaraine dyes exist as monomers in DMSO. Further, we have extended the aggregation studies in DMSO- water system with the intention to analyze the effect of aggregation on SERS intensity of the squaraine dyes adsorbed on AuNPs. Hence the absorption spectra of squaraine dyes in different DMSO- water concentration were recorded. With increase of water

percentage, there is an increase of absorbance around 620 nm and simultaneous decrease of absorbance at 676 nm for all SQ dyes are observed. The peak at 620 nm and 676 nm could be due to the formation of aggregates and monomers respectively. The formation of aggregates is relatively stronger in SQ2, SQ5 and SQ6 compared to other dyes. This may be attributed for the presence of greater hydrophobic nature induced by the long alkyl chain. Absorption spectra for the squaraine dyes SQ2 and SQ5 in DMSO-water are given in **Figure. 2.3**.
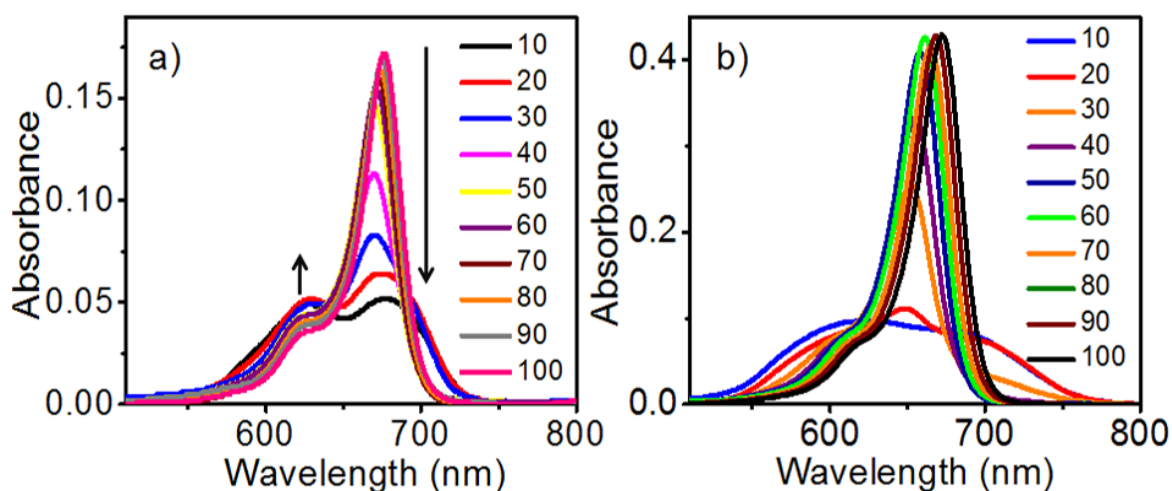
Figure 2.3. Absorption spectra of squaraine dyes a) SQ2 and b) SQ5 in DMSO-water system (Increase in DMSO composition in % is shown in color bar).

2.3.3 SERS spectra of SQ1–SQ6

We have investigated the SERS signal intensity and spectral pattern of all the six squaraine dyes under the particular solvent concentration producing maximum aggregates with emphasize to investigate the maximum SERS intensity and multiplexing peak pattern. The primary screening has been carried out by incubating

each dye with citrate stabilized AuNPs (size: ~ 40-50 nm) to measure the SERS spectra under a confocal Raman microscope.
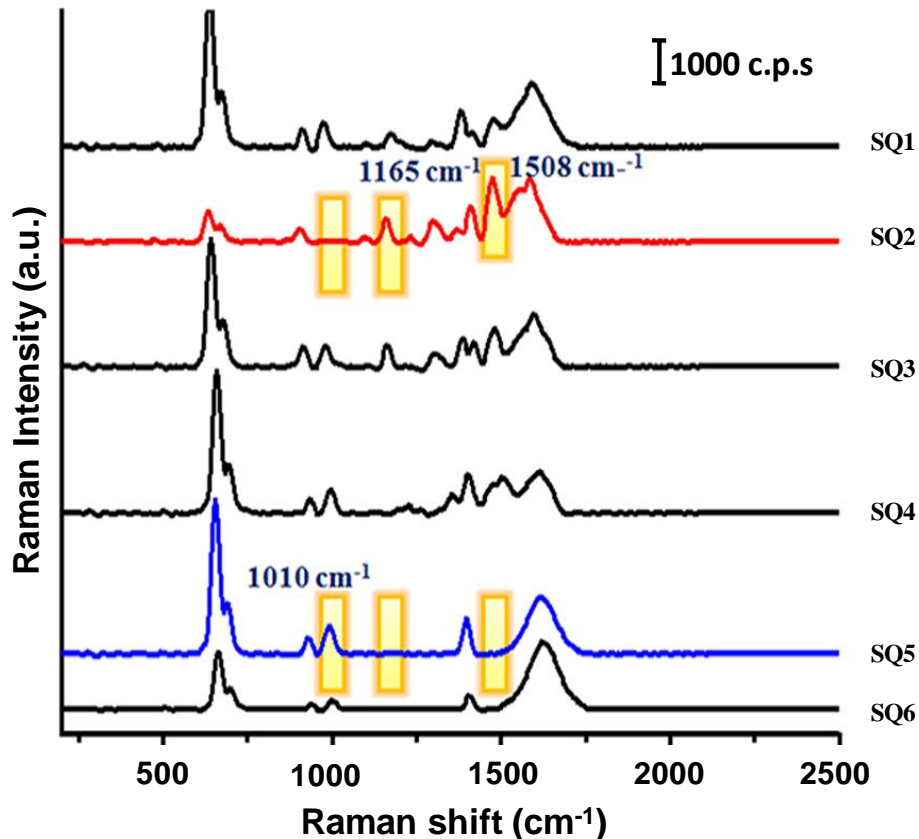
Figure 2.4. Relative intensities of SERS spectra of SQ1–SQ6. Spectra were measured under Raman microscope (532 nm laser excitation, 1.2 mW laser power, acquisition time: 0.5 s).

SERS spectra of all six squaraine dyes exhibited similar peak pattern with the most intense peaks appeared at 674, 1424 and 1624cm^{-1} (**Figure 2.4**). The spectral pattern reflects the architectural design of squaraine dye, especially peak at 674 cm^{-1} is due C–S stretching vibration. The peak at 1424 cm^{-1} is due to C–N stretching mode of carbon ring and bands at 1508 cm^{-1} and 1414 cm^{-1} to C=C stretching mode.[40] The distinct multiplexing bands at 940 cm^{-1}, 1010 cm^{-1} and 1414 cm^{-1} for SQ5 and bands

at 940 cm^{-1} and 1508 cm^{-1} of SQ2 utilized while Raman imaging experiments were performed. The bands at SQ2 and SQ5 exhibited distinct multiplexing peak pattern i.e. 1010 cm^{-1} (SQ5) and 1165 cm^{-1}, 1508 cm^{-1} (SQ2). Therefore, the substantial aggregation in DMSO-water system observed in SQ2, SQ5, and SQ6 also reflected on prominent SERS intensity with multiplexing peak pattern.

2.3.4 Construction of SERS nanotags

The first step in the construction of SERS nanotags was the incorporation of Raman reporters SQ2 and SQ5 on AuNP surface. Which was followed by encapsulation with thiolated PEG (PEG-SH, M.W PEG: 5000Da & SH-PEG-COOH, M.W PEG: 3000Da; RAPP Polymere GmbH). [41- 43] The carboxy functionality introduced by encapsulation with SH-PEG-COOH was utilized for conjugation with target specific monoclonal antibodies. The nanotags, Au-SQ2-PEG and Au-SQ5-PEG were activated with 1-Ethyl-3-(3-dimethylaminopropyl) carbodiimide (EDC), and the activated nanotags were incubated with anti EGFR and p16/Ki-67 antibodies respectively. The construction of the nanotags has been characterized by UV–vis absorption spectra which showed a shift in absorption maxima around 2–3 nm and further confirmed by high-resolution transmission electron microscopy (HR-TEM) and dynamic light scattering (DLS) studies (**Figure 2.5**). In HR-TEM image a thin layer of PEG of thickness 3–4 nm was clearly visible around AuNPs surface and the size increment after PEG encapsulation was also confirmed by DLS data.
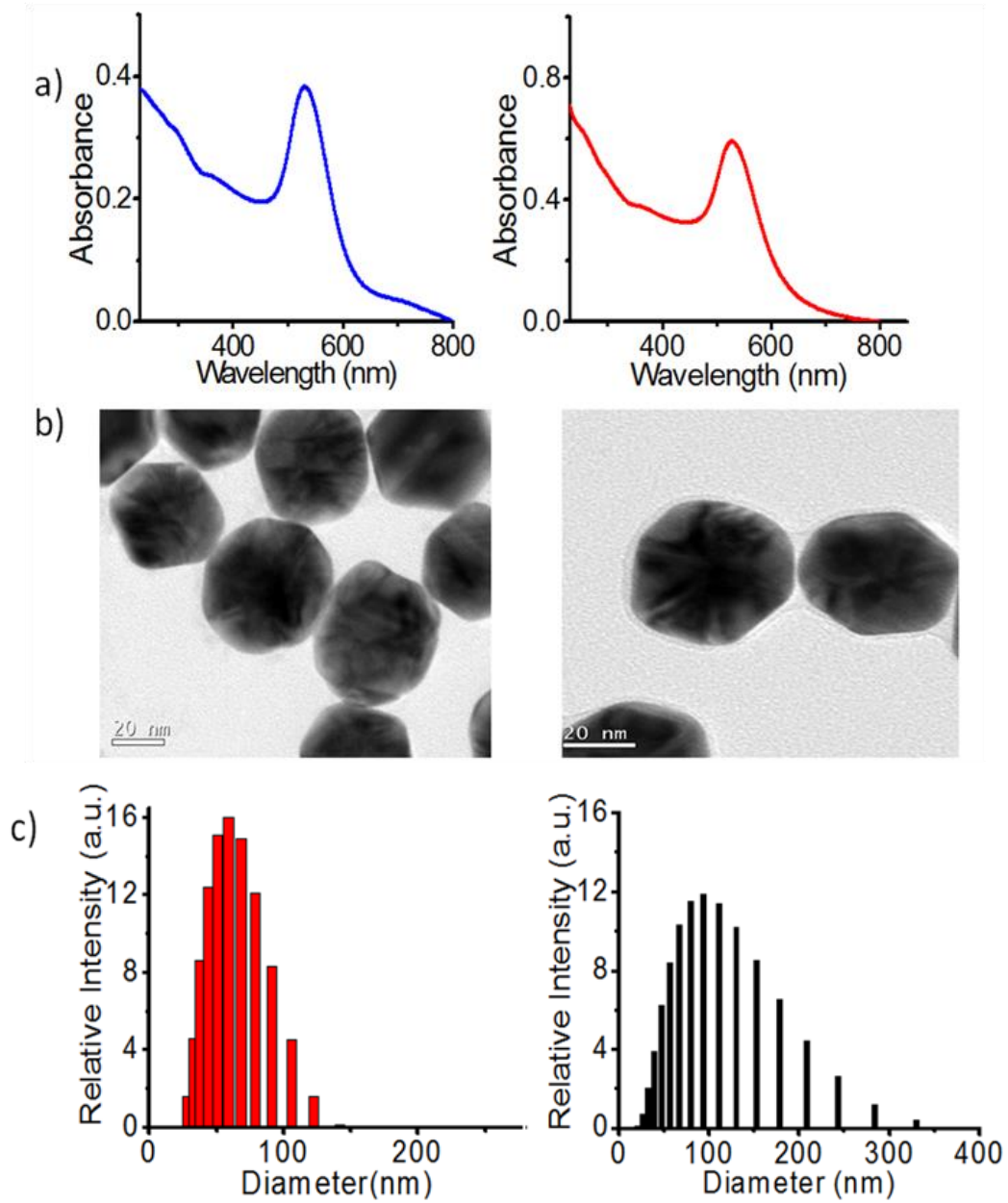
Figure 2.5. (a) UV–vis absorption spectra, **(b)** HR-TEM (scalebar:20 nm) and **(c)**dynamic light scattering image of Au-NPs (size:40nm) (left) and Au-NPs-SQ2-PEG (right).

However, for AuNPs-SQ2-PEG the size is higher in DLS because the PEG will retain more solvent around the particles and the hydrodynamic size will always be higher than the dry state size observed in HR-TEM.

2.3.5. Cell viability assay

Cytoxicity of the nanotags were evaluated before further studies through standard MTT assay, which is a colorimetric assay for measuring cell viability. Cellular oxidoreductase enzymes which are active in live cells are capable of reducing the tetrazolium dye 3-(4,5-dimethylthiazol-2-yl)-2,5-diphenyltetrazolium bromide (MTT) to insoluble formazan crystals, which shows purple color. The absorbance of the solution at 570 nm was recorded for determining percentage cell viability. Cytotoxicity of these nanotags i.e. Au-SQ2-PEG, Au-SQ5-PEG along with Au-NPs, and SQ2, SQ5 dyes alone were assessed in HeLa cells (cervical adenocarcinoma) where both p16/ Ki-67 and EGFR expression has been attributed.
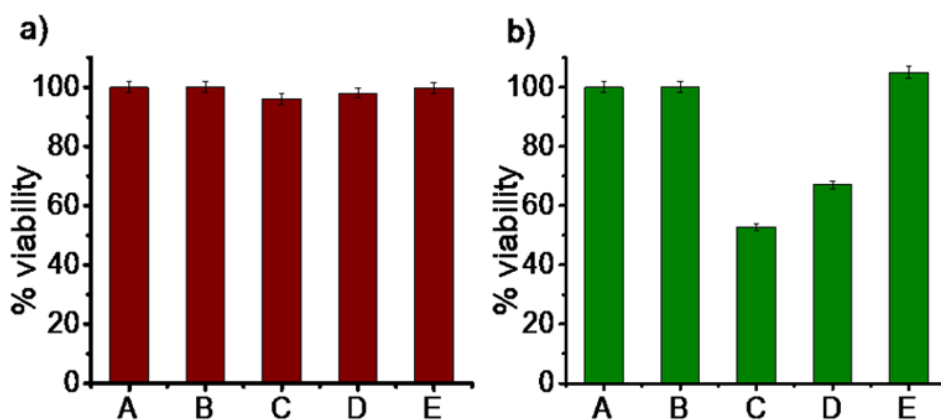
Figure 2.6. Cell viability of HeLa cells after 24h incubation with : A. control; B. Au-NPs (3.44 x 10-5 µM); C. SQ2 (30 µM) for (a) & SQ5 (30 µM) for (b) D. Au-NPs-SQ2 for (a) & Au-NPs-SQ5 for (b) (30 µM of SQ2 on 3.44 x 10-5 µM NPs); E. Au-NPs-SQ2-PEG for (a) & Au-NPs-SQ5-PEG for (b) (30 µM of SQ2 on 3.44 x 10-5 µM NPs).

Interestingly, we found that the Au- conjugates with SQ2 and even SQ2 alone did not show any noticeable cytotoxicity after 24 h; the cells were almost 100%

viable with respect to control (**Figure 2.6a),** where as SQ5 alone and AuNPs-SQ5 showed some extent of toxicity. However after PEG encapsulation the nanotag (AuNPs-SQ5-PEG) again regained 100% cell viability (**Figure 2.6b**). This may be due to the PEG encapsulation preventing the dye exposure at the surface of the nanotag. The cytotoxicity studies of rest of the dyes were carried out in which SQ1, SQ4, SQ6 showed similar trend to SQ5 and SQ3 resembled to that of SQ2.
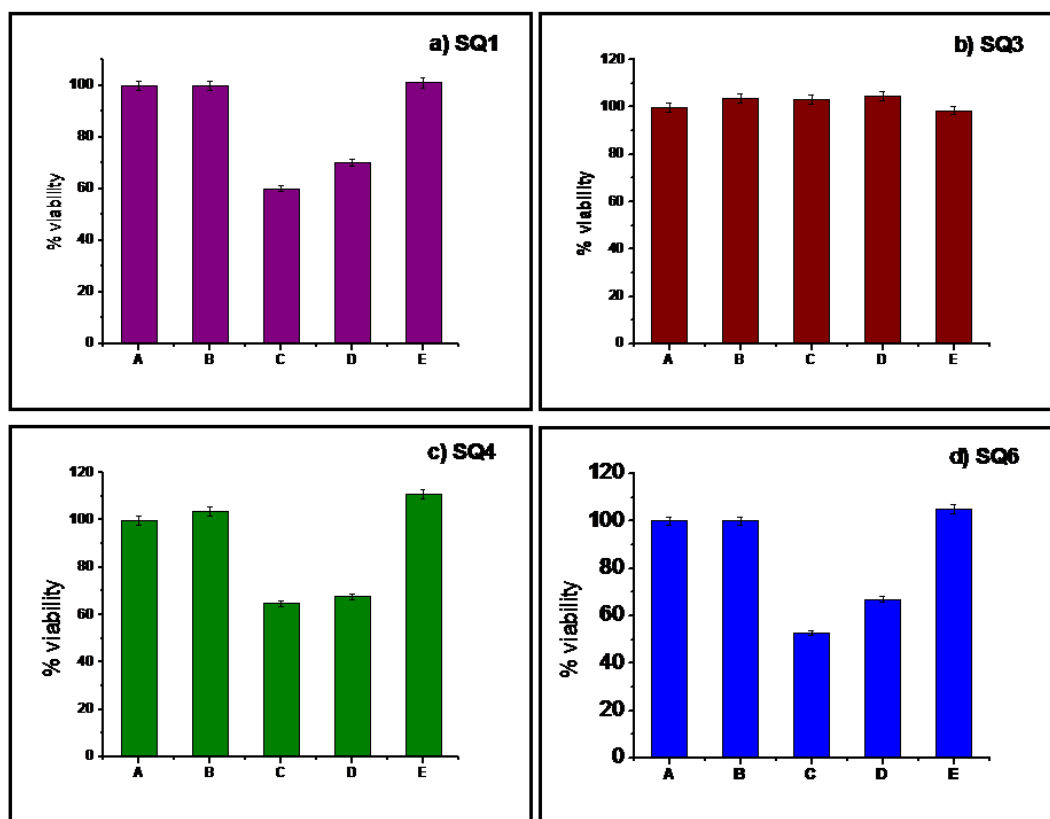
Figure 2.7. Cell viability of HeLa cells after 24h incubation with: A. control; B. Au-NPs (3.44 x 10^{-5} μM); C. SQ1 for (a), SQ3 for (b), SQ4 for (c), and SQ6 for (d) [Conc. 30 μM]; D. Au-NPs-SQ1 for (a), Au-NPs-SQ3 for (b), Au-NPs-SQ4 for (c), Au-NPs-SQ6 for (d) [30 μM of SQ2 on 3.44 x 10^{-5} μM NPs]; E. Au-NPs-SQ2-PEG for (a), Au-NPs-SQ3-PEG for (b), Au-NPs-SQ4-PEG for (c), Au-NPs-SQ6-PEG for (d) [30 μM of dye conc. on 3.44 x 10^{-5} μM NPs].

2.3.6. Preparation of antibody conjugated SERS nanotags

The two best multiplexing SERS nanotags AuNPs-SQ2-PEG and AuNPs-SQ5 PEG were utilized to investigate target specific recognition of HeLa cells as a model study of cervical adenocarcinoma. The terminal carboxy group (SH-PEG-COOH) of the nanotag was conjugated with mouse monoclonal antibody against epidermal growth factor receptors EGFR (Erb-B1) and dual anti-bodyp16/Ki-67 i.e.mouse monoclonal p16 (E6H4), rabbit monoclonal Ki-67 (274 11AC3). EGFR is overexpressed mostly in the cell surface where as p16/Ki-67 expression is mostly on the nuclear surface.
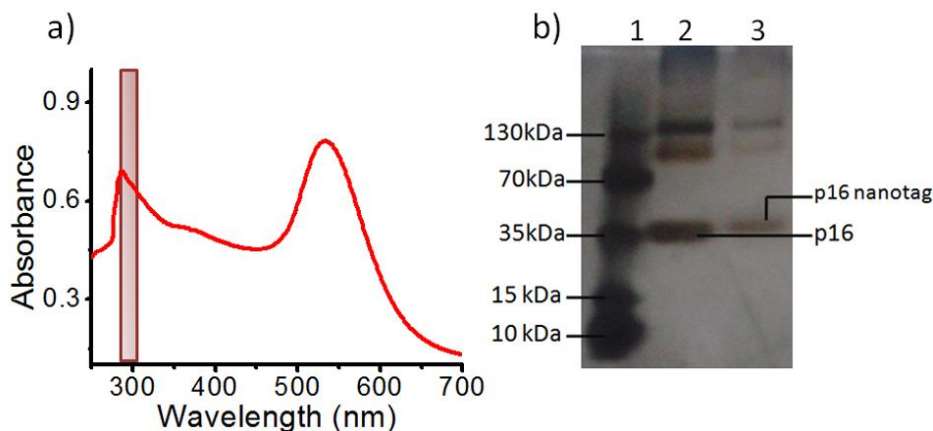
Figure 2.8. (a) UV-vis absorption spectra & (b) SDS PAGE image of nanotag conjugated antibody (Au-NPs-SQ5-PEG- p16/Ki-67); (b) (1) Ladder, (2) Pure p16/Ki-67 antibody (3) Nanotag conjugated antibody (Au-NPs-SQ5-PEG-Ab (p16/Ki-67).

Successful antibody conjugation was achieved by well established EDC-NHS coupling strategy which was finally confirmed by UV–vis spectroscopy and sodium dodecyl sulfate-polyacrylamide gel electrophoresis (SDS-PAGE).[44] UV–vis spectra of antibody conjugated SERS nanotags showed protein absorption peak nearly at 280

nm (**Figure 2.8a**).In SDS-PAGE, the conjugated antibodies in reducing SDS buffer were separated onto 12% polyacrylamide gel. After complete migration, proteins were then silver stained and the size was compared with page ruler plus pre-stained protein ladder 10–250 kDa. The p16 antibody was having size around 40 kDa and that of Ki-67 was around 345 kDa. The antibody conjugated nanotag showed the band nearly at the similar position of the (p16/Ki-67 and EGFR) respective pure antibody. The Ki-67 band was not visible as it may be stuck inside the well because of its high molecular weight (**Figure 2.8b).**

2.3.7 SERS based recognition by antibody conjugated nanotags

We have investigated the recognition with antibody conjugated SERS nanotags by incubating with AuNPs-SQ2-PEG-Ab (EGFR) and AuNPs-SQ5-PEG-Ab (p16/Ki-67)-nanotags in HeLa cells cultured in chamber slide. SERS mapping was carried out after washing with Phosphate-buffered saline (PBS) buffer to remove the unbound nanotags. Cells incubated with AuNPs-SQ2-PEG-EGFR were scanned using the confocal Raman microscope. White light image of a representative cell with the corresponding confocal Raman image is shown in **Figure 2.9a & b** respectively. The cluster analysis was performed on the characteristic Raman spectral scan obtained and the color coded Raman image is shown in **Figure 2.9c**.The corresponding Raman spectra as a result of cluster analysis of the cell are shown in **Figure. 2.9d**. The blue spectrum and region corresponds to the Raman nanotag (AuNPs-SQ2-PEG-Ab (EGFR) attached to the surface of the HeLa cell, red being

nucleus, green the cytoplasm and black region corresponds to the medium (buffer) and glass container. HeLa cells are recognized by targeted anti-EGFR nanotag reflecting strong mapping images where the nanoparticles are mostly localized around the cell surface corresponding to the multiplexed signals at 1508 cm^{-1} and 940 cm^{-1} which confirmed the recognition with the respective cell-surface receptor.
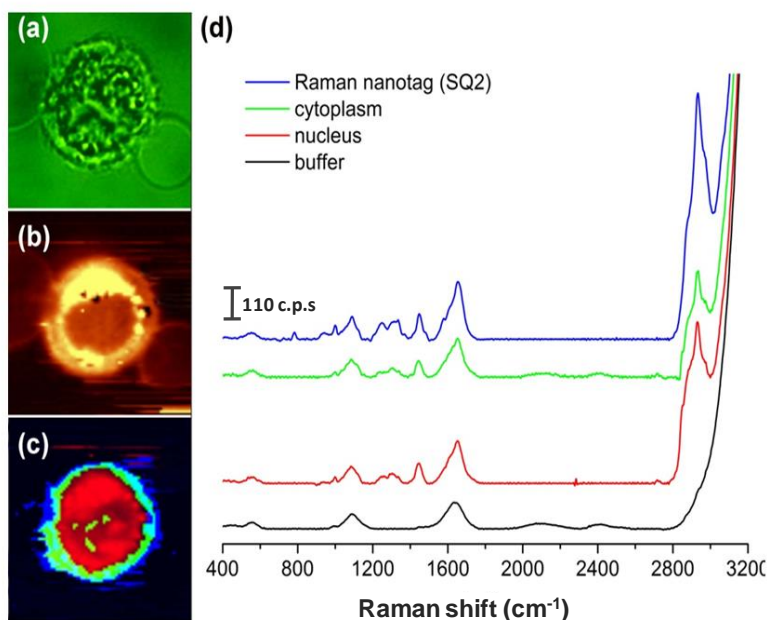
 Figure 2.9. Color coded Raman cluster map: (a) white light image; (b) the corresponding confocal Raman distribution image (2800-3100 cm^{-1}); (c) HeLa cell incubated with AuNPs-SQ2-PEG- Ab(EGFR) and the corresponding spectra (d) (demixed, blue: Raman nanotag (SQ2) on the surface, green: cytoplasm, red: nucleus, black: buffer).

Similarly, **Figure. 2.10 a & b** showed the white light image of the cell and corresponding confocal Raman mapping when HeLa cells were incubated with Au-NPs-SQ5-PEG-Ab (p16/Ki-67). The cluster analysis was performed on the characteristic Raman spectral scan obtained and the color coded Raman mapping

image is shown in **Figure 2.10c**. The corresponding Raman spectra as a result of cluster analysis of the cell are shown in **Figure 2.10d**.
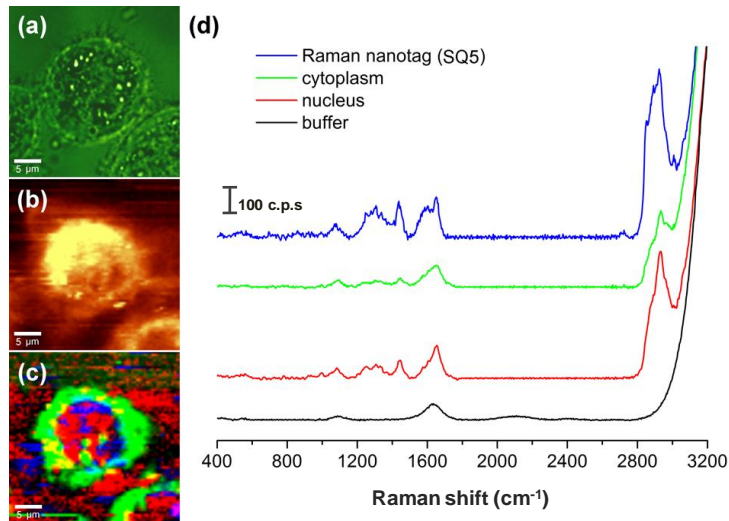
Figure. 2.10. Color coded Raman cluster map: (a) white light image; (b)the corresponding confocal Raman distribution image (2800–3100 cm^{-1}); (c) of HeLa cell incubated with AuNPs-SQ5-PEG-Ab(p16/Ki-67) and the corresponding spectra (d) (demixed, blue: Raman nanotag (AuNPs-SQ5-PEG-Ab(p16/Ki-67) around nucleus, green: cytoplasm, red: nucleus, black: buffer).

The blue spectrum and region corresponds to the Raman nanotag (AuNPs-SQ5-PEG-Ab (p16/Ki-67) around the nucleus, red being nucleus, green the cytoplasm and black region corresponds to the medium (buffer) and glass container. Dual anti p16/Ki-67 nanotag localized around the nucleus as generated from the mapping images corresponding to the multiplexed signals at 1414 and 1010 cm^{-1}.

The control experiment was performed in MCF7 cells (breast carcinoma) after incubating with the SERS nanotag, Au-NP-SQ2-PEG-Ab (EGFR). The Raman

spectral image showed only the presence of nucleus and the cytoplasm in the buffer

background and no recognition was observed in cluster analysis (**Figure 2.11**).
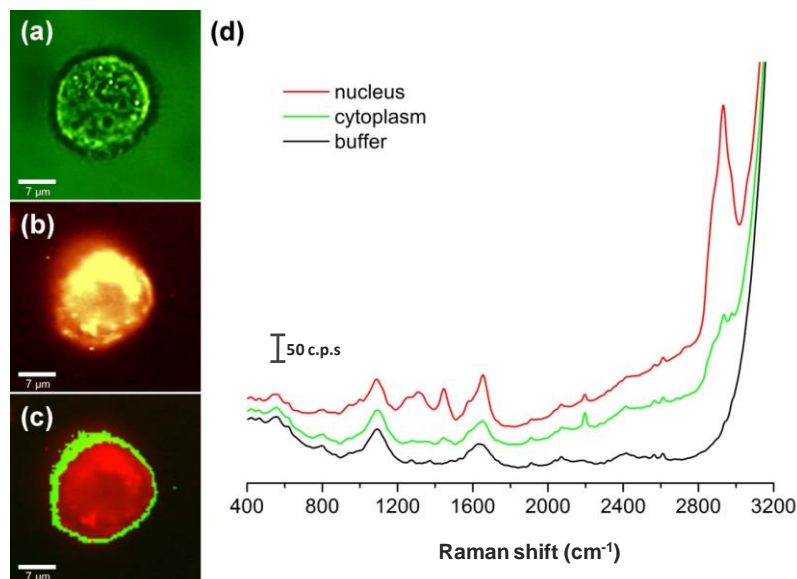
Figure 2.11. Color coded Raman cluster map: (a) white light image; (b) the corresponding confocal Raman distribution image (2800-3100 cm^{-1}); (c) MCF7 cells incubated with SERS-nanotag (Au-NPs-SQ2-PEG-Ab(anti-EGFR)) and the corresponding spectra (d) (demixed, green: cytoplasm, red: nucleus, black: buffer), as negative control.

2.3.8 Immunocytochemistry based recognition

SERS nanotag based recognition was compared with immunocytochemistry technique. Immunostaining of HeLa cells was done with dual p16/Ki-67 and EGFR primary anti-body individually (**Figure 2.12**). In case of dual antibody, p16/Ki-67, positive staining was observed when the cells were visualized with a brown cytoplasmic (p16) and a red nuclear (Ki-67) stain. When Immunostaining was performed using anti-EGFR, cell surface antibody highly expressed in cervical

carcinoma, the cell surface was stained with 3,3'-diaminobenzidine (DAB) and purple

colored nucleus counter stained by haematoxylin.
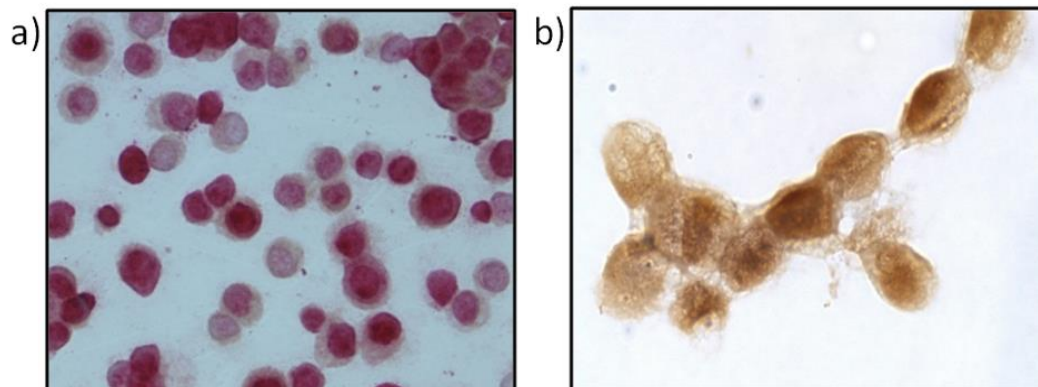
Figure 2.12. Immunostaining of HeLa cells: (a) Cells staining with DAB (for p16) designed by brown cytoplasm and staining with Fast red (for Ki-67) depicted as reddish nucleus. b) Cell staining with DAB (EGFR) designated by brown cell surface; DAB = 3, 3'-diaminobenzidine.

Moreover, EGFR negative MCF7 immunostaining was done as a negative control **(Figure 2.13)**.
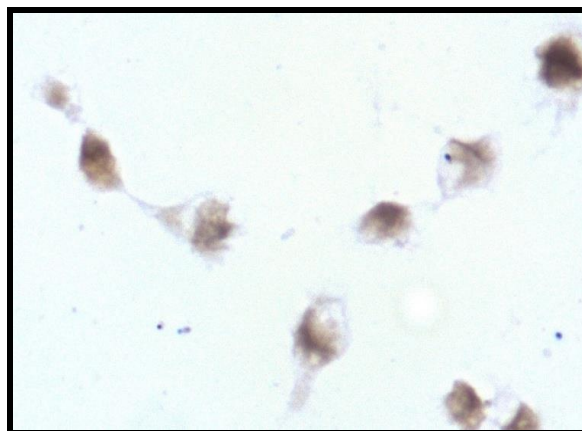
Figure 2.13. Immunostaining with MCF7 cells: Cells are stained with DAB (EGFR) for recognition of surface marker. No obvious brown staining observed from cell surface.

These immunostaining processes are time consuming, requires almost two days to complete and definitely requires high technical expertise to get accurate outcome.

2.4 Conclusion

In this work a series of six squaraine dyes were synthesized with 1,1,2-trimethyl-1H-benzo[e]indole and 2-methylbenzo[d]thiazole backbone and investigated their photophysical properties which includes the influence of dye aggregation on SERS signal pattern and it's enhancement. This phenomenon was observed in all the six squaraines (SQ1–SQ6) but more prominently observed on SQ5, SQ6 and SQ2. Subsequently polymer coated SERS nanotag were prepared (AuNPs-SQ2-PEG-Ab(EGFR) and AuNPs-SQ5-PEG-Ab(p16/Ki-67) by conjugation with monoclonal antibodies against EGFR and dual antibody, p16/Ki-67 for recognition of cervical cancer cells. SERS-mapping experiment (cluster mapping) confirmed two differential recognition on HeLa cells. Moreover, SERS based recognition has been compared with conventional immunocytochemistry using the same antibodies in HeLa cells which signifies the fast and accurate SERS technique for the detection of cervical malignancy. The encouraging results obtained using HeLa cells prompted us to extend the further studies in real patient cervical smear sample which could be a noninvasive, ultrafast diagnostic platform for early detection of cervical cancer dysplasia.

2.5. Experimental Section

2.5.1. Synthesis – General Procedures

All the chemicals (synthetic building blocks) and solvents were purchased from Sigma-Aldrich, AlfaAesar, Fluka, MERCK, and used without further purification. EGFR-IgG2a (sc-120) and p16/Ki-67 antibody was supplied by SantaCruz Biotechnology, CINtec® PLUS cytology kit, Roche respectively. The reactions were monitored using thin layer chromatography on silica gel 60 F254 (0.2 mm; Merck) and visualization was accomplished using a hand held UV-lamp (365 nm). Column chromatography was used to purify the reaction products in a glass column packed with silica gel of size, 100-200 microns.

2.5.1.1. Syntheses of squaraine dyes SQ1-SQ6

2.5.1.1.1.Synthetic intermediates towards squaraine dyes (SQ1 -SQ6)

2.5.1.1.1.1 Synthesis of 1, 1, 2-trimethyl-3-propyl-1H-benzo[e]indolium iodide (1)
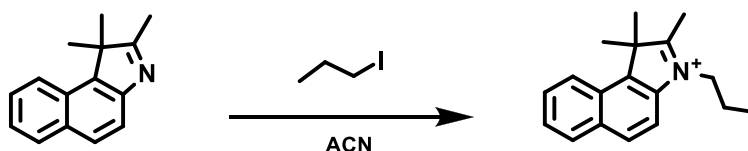
To a solution of 1, 1, 2-trimethyl-1H-benzo[e]indole (1 g, 4.7mmol) in acetonitrile 1-iodopropane (2.3ml, 23.9 mmol) was added and refluxed with continuous stirring for 15 h. The mixture was recrystallized in acetone to obtain the product as an off white solid (1g, yield =87 %). ^{1}HNMR (500 MHz, CDCl$_3$) δ 8.13-8.06 (m, 3H), 7.78-7.74(m, 2H), 7.69 (t, 1H, J=7.5 Hz), 4.83(t, 2H, J=7.5 Hz), 3.22(s, 3H), 2.11-2.07 (m,

2H), 1.90(s, 6H), 1.13 ppm (t, 3H, J= 7.5Hz). HR-MS: (FAB), m/z ($C_{18}H_{22}N^+$) calcd:

252.1747, found: 252.1750.

2.5.1.1.1.2. Synthesis of 3-(3-aminopropyl)-1, 1, 2-trimethyl-1H-benzo[e]indolium iodide (2)
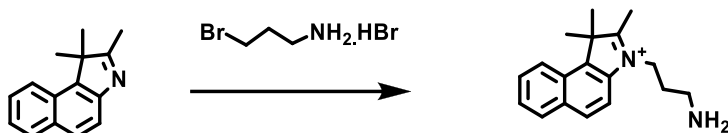
3-bromopoylamine hydro bromide (1g, 4.7 mmol) was added in a seal tube

containing 1, 1, 2-trimethyl-1H-benzo[e]indole (1g, 4.7 mmol) under N_2 atmosphere,

and was gently heated up to 110 ^{0}C in an oil bath. The mixture was kept for 10 h with

stirring. The reaction mixture was cooled to room temperature to form a solid cake

which was washed with diethyl ether (Et_2O) and a chloroform-Et_2O solution. The

resulting solid was then dried under high vacuum affording the product as an off

white solid (1.03g, 81 % yield). ^{1}HNMR (500 MHz, $CDCl_3$) δ 7.81(d, 1H, J= 9Hz),

7.73(d, 1H, J= 8.5Hz), 7.67 (d, 1H, J= 8.5 Hz), 7.39-7.35(m, 1H), 7.29-7.18(m, 1H),

6.89 (d, 1 H, J=10Hz), 4.12-3.98(m, 2H), 3.71(t, 2H, J= 6.5Hz), 3.28-3.23(m, 2H),

1.71 (s, 6H), 1.62 (s, 3H). HR-MS: (FAB), m/z ($C_{23}H_{31}N_2O_2^+$) calcd: 267.2380,

found: 267.2391.

2.5.1.1.1.3. Synthesis of 3-(3-(tert-butoxycarbonylamino) propyl)-1, 1, 2-trimethyl-1H-benzo[e]indolium iodide (3)
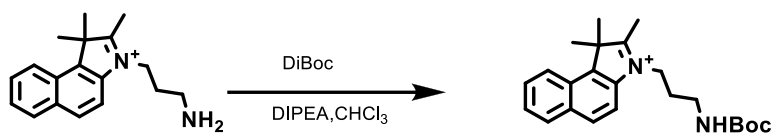
3-(3-aminopropyl)-1, 1, 2-trimethyl-1H-benzo[e]indolium iodide **(2)**, (0.9 g, 3.3 mmol), and di-tert-butyl dicarbonate (1.8 g, 8.4 mmol) were added to a mixture of dry chloroform (15 mL) and diisopropyl ethylamine (9 ml, 52 mmol,). The reaction mixture was gently heated to reflux and continued for 4h. The organic layer was extracted with Et$_2$O, dried over anhydrous Na$_2$SO$_4$, and concentrated under reduced pressure. Purification of the crude residue on a silica gel column using dichloromethane and methanol as an eluting solvent yielded the brown solid product (1.03g, yield = 84%). ^{1}HNMR (500 MHz, CDCl$_3$) δ 7.95(d, 1H, J= 9Hz), 7.75(d, 1H, J= 8.5Hz), 7.69 (d, 1H, J= 8.5 Hz), 7.40-7.37(m, 1H), 7.27-7.17(m, 1H), 6.97(d, 1 H, J=10Hz), 3.97-3.92(m, 2H), 3.67(t, 2H, J= 6.5Hz), 3.24-3.20(m, 2H), 1.66 (s, 6H), 1.58 (s, 3H), 1.45ppm (s, 9H). HR-MS: (FAB), m/z (C$_{23}$H$_{31}$N$_2$O$_2^+$) calcd: 367.2380, found: 367.2391.

2.5.1.1.1.4. Synthesis of 2-methyl-3-propylbenzo[d]thiazol-3-ium iodide (4)
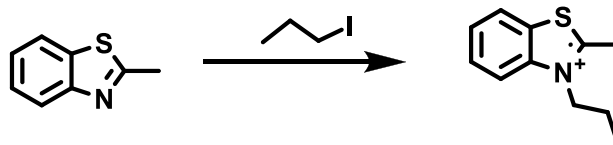
2-methylbenzo[d]thiazole (1g, 6.7 mmol) and propyl iodide (5.6 g, 33 mmol) were added to a seal tube and heated overnight at 110ºC under nitrogen atmosphere. Product was formed as a gray solid washed with Et$_2$O and dried under high vacuum. (1.12g, yield = 87%). ^{1}HNMR (500 MHz, CDCl$_3$) δ 8.36(d, 1H, J= 8Hz), 8.08 (d, 1H, J= 8.5Hz), 7.83(t, 1H, J= 8Hz), 7.72(t, 1H, J= 8Hz), 4.86(t, 2H, J= 8Hz), 3.46(s, 3H), 2.08-2.00(m, 2H), 1.12ppm (t, 3H, J=7.5Hz). HR-MS: (FAB), m/z (C$_{11}$H$_{14}$NS$^+$) calcd: 192.0847, found: 192.0850

2.5.1.1.1.5. Synthesis of 3-hexyl-2-methylbenzo[d]thiazol-3-ium iodide (5)
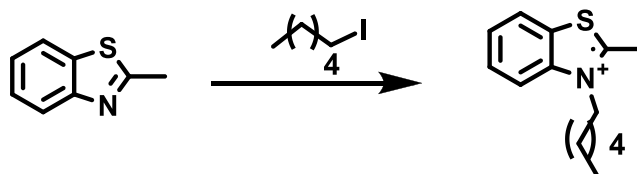
2-methylbenzo[d]thiazole (1g, 6.7 mmol) and 1-iodohexane (7.1 g, 33 mmol) were added to a seal tube and heated overnight at 110ºC under nitrogen atmosphere. Product was formed as a gray solid washed with Et$_2$O and dried under high vacuum. (1.39g, yield= 89%). ^{1}HNMR (500 MHz, CDCl$_3$) δ 8.39(d, 1H, J= 8Hz), 8.02 (d, 1H, J= 8.5Hz), 7.82(t, 1H, J= 8.1Hz), 7.70(t, 1H, J= 8Hz), 4.85(t, 2H, J= 8Hz), 3.46(s, 3H), 2.30-2.03(m, 2H), 1.97-1.91(m, 2H), 1.52-1.49(m, 2H), 1.42-1.24(m,4H), 0.73ppm (t, 3H, J= 7.5Hz). HR-MS: (FAB), m/z (C$_{14}$H$_{20}$NS$^+$) calcd: 234.3798, found: 234.3801.

2.5.1.1.1.6. Synthesis of 3-dodecyl-2-methylbenzo[d]thiazol-3-ium iodide (6)
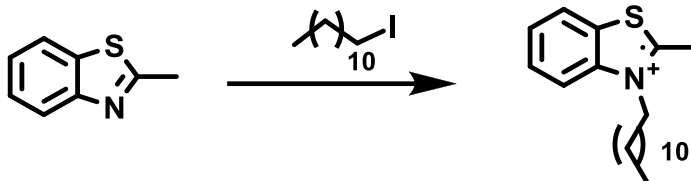
2-methylbenzo[d]thiazole (1g, 6.7 mmol) and 1-iodododeane (8.3 g, 33 mmol) were added to a seal tube and heated overnight at 110ºC under nitrogen atmosphere. Product was formed as a gray solid washed with Et_2O and dried under high vacuum. (1.8 g, yield= 87%). ^{1}HNMR (500 MHz, $CDCl_3$) δ 8.21(d, 1H, J= 8.5Hz), 8.159 (d, 1H, J= 8.5 Hz), 7.83(t, 1H, J= 8Hz), 7.72(t, 1H, J= 8Hz), 4.66(t, 2H, J= 8Hz), 3.13 (s, 3H), 1.91-1.84(m, 2H),1.46-1.40(m, 2H),1.35-1.29(m, 2H), 1.22-1.18(m, 14H) 0.79 ppm (t, 3H, J= 6.5Hz). HR-MS: (FAB), m/z ($C_{20}H_{32}NS^+$) calcd: 318.5398, found: 318.5401.

2.5.1.1.2. Synthesis symmetrical squaraine dye SQ1
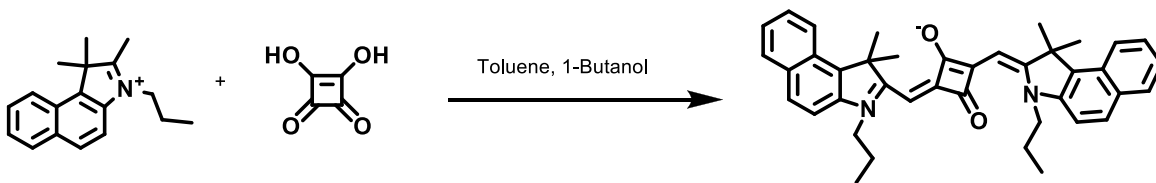
1, 1, 2-trimethyl-3-propyl-1H-benzo[e]indolium iodide (**1**), (250 mg, 0.99mmol,) was added to a solution of squaric acid (56 mg, 0.49 mmol) in a mixture of dry n-butanol (6ml) and dry toluene (4ml) in an round bottom flask equipped with a Dean Stark apparatus. Reaction mixture was refluxed for 12 h under N_2 atmosphere. A

deep green colored reaction mixture was concentrated and the crude product was purified by column chromatography using silica gel. Elution of the column with a mixture of DCM/ methanol (1:9) afforded the desired squaraine dyes as green solid (233mg, yield = 49 %). ^{1}HNMR (500 MHz, CDCl$_3$) δ 8.21(d, 2H, J= 8.5Hz), 7.91-7.86(m, 4H), 7.58(t, 2H, J= 7.5Hz), 7.42(t, 2H, J= 7.5Hz), 7.30(d, 2H, J= 10Hz), 6.04(s, 2H), 4.11(s, 4H), 2.09(s, 12H), 1.96-1.92(m, 4H), 1.09ppm (t, 6H, J= 7Hz). HR-MS: (FAB), m/z (C$_{40}$H$_{41}$N$_2$O$_2^+$) calcd: 581.3163 found: 603.2928 [M+Na]$^+$.

2.5.1.1.3. Synthesis of Unsymmetrical squaraine dye SQ2
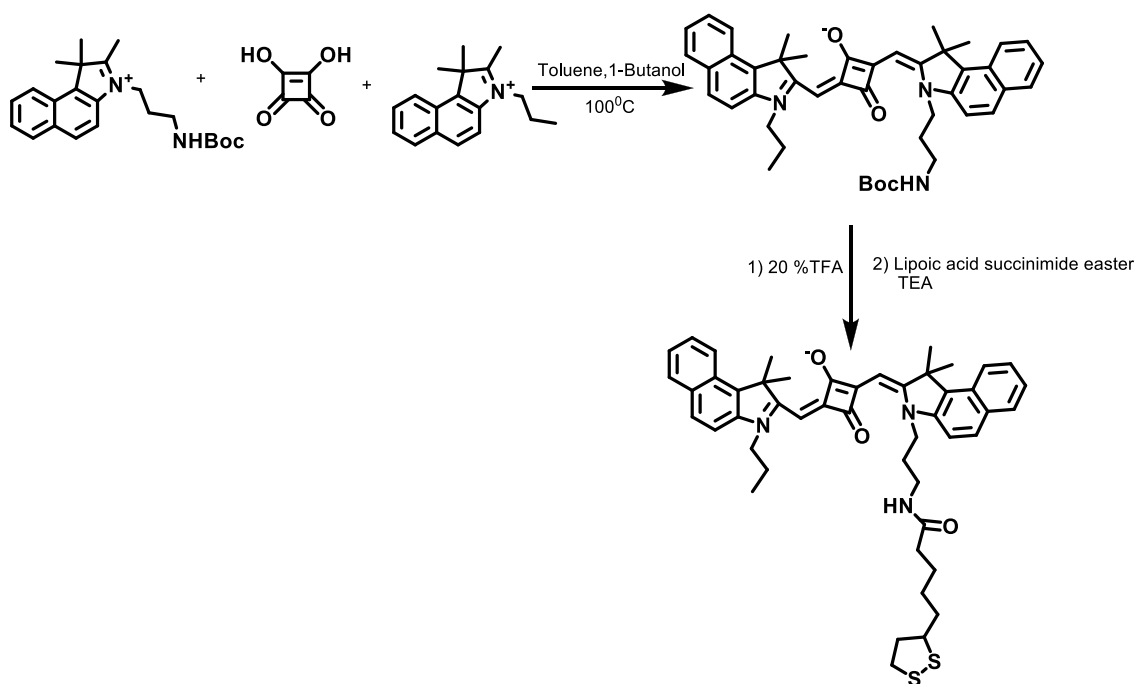
A mixture of 3- (3- (tert-butoxycarbonylamino) propyl)-1, 1, 2-trimethyl-1H-benzo [e] indolium iodide **(3)**, (0.2g, 0.55mmol), 1,1, 2-trimethyl-3-propyl-1H-benzo[e]indolium iodide **(1)**, (0.14g, 0.55mmol) and squaric acid (0.06g, 0.55 mmol) acid were refluxed in a mixture of dry toluene and 1-butanol (1:4) with azeotropic

distillation of water for 12 h under N_2 atmosphere. The solid residue obtained was purified by column chromatography using chloroform and methanol mixed solvent (9:1) afforded sticky green solid (0.15g, yield= 40%). ^{1}HNMR (500 MHz, CDCl$_3$): δ 8.198 (t, 2H, J = 9Hz), 7.91-7.85(m, 4H), 7.59-7.55(m, 2H), 7.44-7.40 (m, 2H), 7.31-7.27(m, 2H), 6.04(s, 1H), 5.99(s, 1H), 4.12(m, 4H), 3.32-3.31(d, 2H, J= 5Hz), 2.17(s, 3H), 2.08(s, 12H), 1.44(s, 10H), 1.26(s, 4H), 1.08ppm (t, 4H, J= 7.5). HR-MS: (FAB), m/z ($C_{45}H_{49}N_3O_4^-$) calcd: 695.3723, found: 696.3804[M+H] $^+$. Squaraine dye intermediate was treated with 10% TFA in DCM for 2 h to de-protect the Boc group. After removal of trifluoroacetic acid (TFA), free amine salt was dissolved in dry DCM followed by the addition of 0.2mL TEA. Lipoic acid succinimidyl ester was added after stirring with TEA and continued for overnight at room temperature. Product formed (SQ3) was purified by silica gel column chromatography using DCM-methanol mixture (9.5:0.5) yielded the product. (0.05g, yield= 40 %). ^{1}HNMR (500 MHz, CDCl$_3$): δ 8.22-8.16 (m, 2H) , 7.89(t, 4H, J= 9.5Hz), 7.61-7.56(m, 2H), 7.45-7.41(m, 2H), 7.32(t, 2H, J= 8Hz), 6.04 (s, 1H), 6.00(s, 1H), 4.15(s, 2H), 3.17-3.11(m, 12H), 2.33(t, 2H, J= 7.5Hz), 1.95-1.86(m, 4H), 1.74-1.66(m, 4H), 1.51-1.46 (m, 6H), 1.34(s, 9H), 1.07ppm (t, 3H, J= 7.5Hz). HR-MS: (FAB), m/z ($C_{48}H_{53}N_3O_3S_2$) calcd: 783.3528, found: 784.3603[M+H] $^+$, 806.3422 [M+Na]$^+$.

2.5.1.1.4. Synthesis of symmetrical squaraine dye SQ3
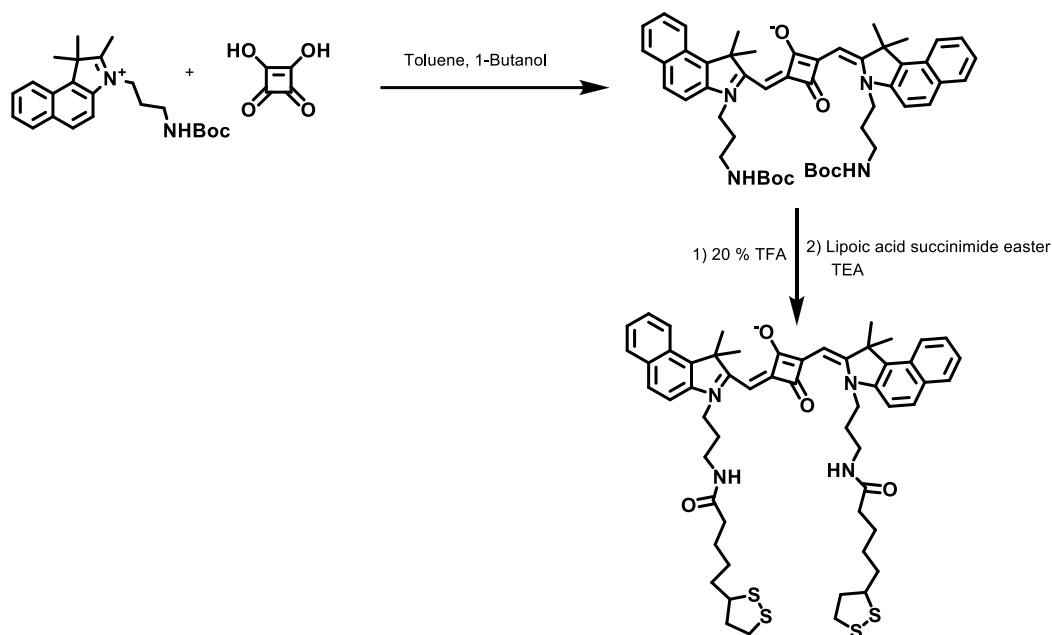
3- (3- (tert-butoxycarbonylamino) propyl)-1, 1, 2-trimethyl-1H-benzo [e] indolium iodide **(3)**, (0.3g, 0.81mmol) squaric acid (0.04g, 0.40mmol) and Quinoline (0.5ml) were refluxed in a mixture of dry toluene and 1-butanol with azeotropic distillation of water for 12 h under N_2 atmosphere. Reaction mixture was distilled off and the residue was purified by column chromatography. Elution of the column with (9:1) methanol and DCM afforded the symmetrical squaraine dye (0.27g ,yield= 42%). ^{1}HNMR (500 MHz, CDCl$_3$) δ 8.19(d, 2H, J= 8.5Hz), 7.92-7.87(m, 4H), 7.60-7.57(m, 2H), 7.45-7.42(m, 2H), 7.32(d, 2H, J= 10Hz)**,** 6.01(s, 2H), 4.22(s, 4H), 3.37-3.32(m, 4H), 2.11(s, 12H), 1.66(s,6H) 1.43ppm (s, 18H). HR-MS: (FAB), m/z ($C_{50}H_{58}N_4O_6$) calcd: 810.4356, found: 811.4432 [M+H] [+].Deprotection of Boc was carried out by treating the squaraine dye intermediate with 10% TFA in DCM (2 mL) for 3h. After removal of TFA free amine salt formed was dissolved in dry DCM followed by the

addition of 0.2 mL TEA. Lipoic acid succinimidyl ester was added after stirring for 10 minutes with TEA. Product formed (SQ2) was purified by column chromatography (0.15g, yield = 49%). ^{1}HNMR (500 MHz, CDCl$_3$): δ 8.16(d, 2H, J= 8.5Hz), 7.88(t, 4H, J= 8Hz), 7.56 (t, 2H, J= 7.5Hz), 7.41(t, 2H, J= 7.5Hz), 7.32(d, 2H, J= 9Hz), 5.98(s, 2H), 4.22(br.s., 4H), 3.55-3.52(m, 2H), 3.45(t, 4H, J= 6Hz), 2.43-2.39(m, 2H), 2.31(t, 4H, J= 7Hz), 1.89-1.85(m, 2H), 1.72-1.64 (m, 2H), 2.02ppm (s, 12H). HR-MS: (FAB), m/z (C$_{56}$H$_{67}$N$_4$O$_4$S$_4^-$) calcd: 987.4082, found: 1009.3863[M+Na]$^+$.

2.5.1.1.5. Synthesis of symmetrical squaraine dye SQ4
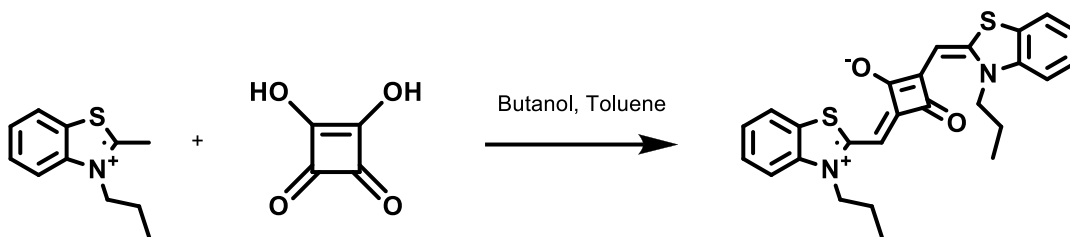
2-methyl-3-propylbenzo[d]thiazol-3-ium **(4),** (0.5g, 2.6 mmol) squaric acid (0.14g, 1.3 mmol), Quinoline (0.5mL) were refluxed in a mixture of dry toluene and 1-butanol for 8 h with azeotropic distillation of water. Solvent was removed under high vacuum and product obtained was purified by column chromatography. Elution of the column with a mixture of DCM/ methanol (1:9) afforded the desired squaraine dyes as green solid (0.5g, yield= 43%).^{1}HNMR (500 MHz, CDCl$_3$): δ 7.52(d**,** 2H, J= 7.5Hz), 7.35(t, 2H, J= 8Hz), 7.19(t, 2H, J= 7.5Hz), 7.12(d, 2H, J= 8Hz), 5.88(s, 2H),

4.03(t, 4H, J= 7.5Hz), 1.90-1.80(m, 4H), 1.06ppm (t, 6H, J= 7.5Hz). HR-MS: (FAB),

m/z ($C_{26}H_{24}N_2O_2S_2$) calcd: 460.1279, found: 461.1342[M+H] $^+$, 483.11746 [M+Na]$^+$.

2.5.1.1.6. Synthesis of symmetrical squaraine dye SQ5
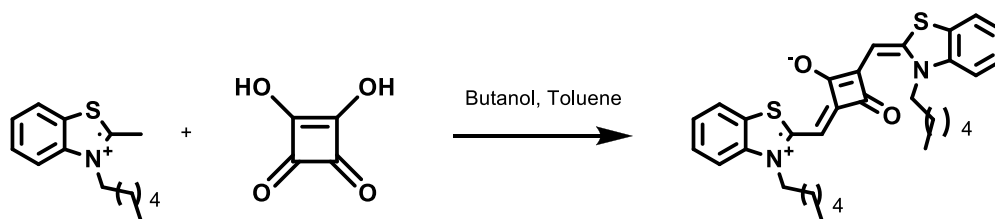
3-hexyl-2-methylbenzo[d]thiazol-3-ium **(5), (**0.25g, 1.0mmol) squaric acid (0.06g,

0.53mmol), Quinoline (0.5mL) were refluxed in a mixture of dry toluene and 1-

butanol for 8h with azeotropic distillation of water. Solvent was removed under high

vacuum and product obtained was purified by column chromatography. Elution of the

column with a mixture of DCM/ methanol (1:9) afforded the desired squaraine dyes

as green solid (0.28g, yield= 49 %).^{1}HNMR (500MHz, CDCl$_3$): δ 7.53(d**,** 2H, J=

8Hz), 7.36(t, 2H, J= 7.5Hz), 7.19(t, 2H, J= 7.5Hz), 7.12(d, 2H, J= 8Hz), 5.87(s, 2H),

4.06(t, 4H, J= 8.1Hz), 1.84-1.78(m, 4H), 1.46-1.42(m, 4H), 1.35-1.32(m, 8H),

0.91ppm (t, 6H, J= 6.5Hz). HR-MS: (FAB), m/z ($C_{32}H_{36}N_2O_2S_2$) calcd: 545.7704,

found: 545.2293 [M+H] $^+$, 567.2119[M+Na]$^+$.

2.5.1.1.7. Synthesis of symmetrical squaraine dye SQ6
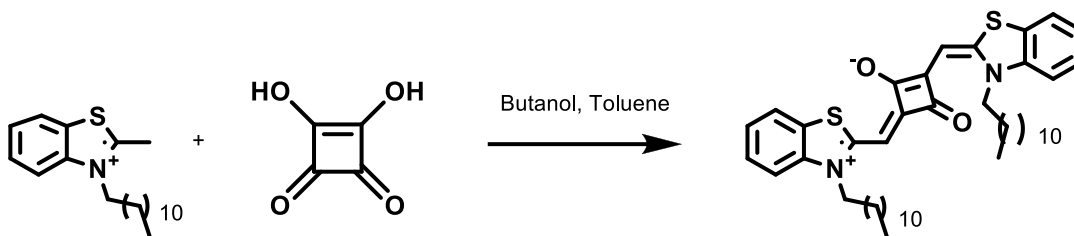
3-dodecyl-2-methylbenzo[d]thiazol-3-ium **(6),** (0.5g, 1.5 mmol) squaric acid (0.089 g, 7.8 mmol), Quinoline (0.5 mL) were refluxed in a mixture of dry toluene and 1-butanol for 8 h with azeotropic distillation of water. Solvent was removed under high vacuum and product obtained was purified by column chromatography. Elution of the column with a mixture of DCM/ methanol (1:9) afforded the desired squaraine dyes as green solid. (0.50g, yield= 45%).^{1}HNMR (500 MHz, CDCl$_3$): δ 7.53(d**,** 2H, J= 8Hz), 7.36(t, 2H, J= 7.5Hz), 7.19(t, 2H, J= 7.5Hz), 7.12(d, 2H, J= 8Hz), 5.87(s, 2H), 4.06(t, 4H, J= 8Hz), 1.84-1.78(m, 8H), 1.45-1.40(m, 4H), 1.37-1.26(m, 12H), 0.88ppm (t, 3H, J= 6.5Hz). HR-MS: (FAB), m/z (C$_{44}$H$_{60}$N$_2$O$_2$S$_{2)}$ calcd: 713.0894, found: 736.40222 [M+Na]$^+$.

2.5.1.2. Preparation of SERS-nanoprobe

2.5.1.2.1 Thiolated PEG encapsulation

Gold nanoparticles (Au-NPs, size: ~ 40-50 nm) was prepared by well established citrate reduction method. The squaraine Raman reporter molecules SQ2 and SQ5 (30 mM) were mixed with Au-NPs (3.44 x 10^{-5} µM NPs) in 1:9 ratio (v/v). The mixture

was incubated for 10 min in order to get maximum adsorption on Au-colloids. All the squaraine dyes except SQ1 contains sulfur which has strong binding affinity to gold surface. So the adsorption of squaraine dyes on gold surface is mainly by chemisorption. In the case of SQ1, adsorption on gold surface is by noncovalent interaction i.e. physisorption. The hetero functional linker SH-C_2H_4-CONHPEG-C_3H_6-COOH (PEGMW: 3000 Da; RAPP Polymer GmbH) solution (10mM) was added to a same ratio (1:9) of gold- squaraine (Au-SQ) solution in a polypropylene tube with rapid mixing. After 15 min of mixing the Au-colloid was exposed to excess of CH_3-PEG-SH (PEGMW: 5000 Da; RAPP Polymer GmbH) (10 mM) to maximize its surface coverage and to stabilize the PEG. Excess PEG-SH was removed after 3h of through mixing by three rounds of centrifugation (4000 rpm, 15 min) and resuspended in milli-Q water. For antibody conjugation water was replaced by PBS for covalent conjugation at the carboxyl terminal of hetero functional PEG. Successful PEG encapsulation was confirmed by UV–vis absorption studies and HR-TEM.

2.5.1.2.2. Antibody conjugation of PEG encapsulated Au-NP

The antibodies were purified by filtration using Amicon Ultra 3K centrifuge filters (Millipore) to remove the sodium azide. The carboxylic groups of the PEG encapsulated nanotag were activated by EDCN-(3-(dimethylamino)-propyl)-N′-ethylcarbodiimide (EDC, 25 mM) and N-hydroxy succinimide (NHS, 25 mM). After 30 min incubation, excess of EDC and NHS was removed by 3 rounds of

centrifugation (8000 rpm, 15 min), and re-suspended in PBS using Amicon Ultra 3K centrifuge filters (Millipore). The activated nanotags Au-SQ2-PEG and Au-SQ5-PEG were incubated with antibody EGFR (25 mL, 200 mg/ mL) and p16/Ki-67(100mL) at 25°C for 2 h respectively. Antibody conjugated nanotags were stored at 4°C overnight. Further unbound antibodies were removed by a five round of centrifugation at 10000 rpm 5 min. The pellet containing the antibody conjugated nanotags were then again resuspended in PBS and stored at 4°C. Antibody conjugation was further confirmed by UV–vis Spectroscopy and SDS- PAGE.

2.5.1.2.3. SDS- polyacrylamide gel electrophoresis

To confirm the antibody conjugation SDS polyacrylamide gel electrophoresis was done. A 12% resolving and 5% stacking gel was used for the separation of conjugated and pure antibodies.

2.5.2. Cell culture and SERS based recognition

Human cervical cancer cell, HeLa and human breast adenocarcinoma cell line, MCF7 ware obtained from American Type Culture Collection (ATCC, USA). The cells were grown at 37°C in DMEM medium supplemented with 10% Fetal Bovine Serum and Antibiotics (100UmL^{-1} penicillin/100 µg mL^{-1} streptomycin mixture) in a CO_2 incubator. Cells were cultured in 4 well chamber slide made of glass at a seeding density of 10^4 cells/mL. AuNPs-SQ2- PEG-EGFR andAuNPs-SQ5-PEG-Ab (p16/Ki-67) were added (~500pM) to the wells separately including control (media alone) and

was incubated overnight at 37 °C. Further the cells were washed in PBS three times. These live cells in physiological medium (PBS) were investigated with the Spectral Imaging Mode of the confocal Raman microscope (alpha300R, WITec Inc.Germany). A spectrum at every pixel was taken (Scan Range: 40 x 40 μm^2, 100x100pixel, 10,000 spectra) using a 60 x Nikon (NA=1.0) water objective. The sample was excited with a 10mW power 532 nm frequency doubled Nd:YAG laser. Using the integrated video camera, a suitable cell was focused and scanned with an integration time of 0.5 s. The imaged data was evaluated utilizing the cluster analysis feature of Witec Project Plus software.

2.5.3. Recognition by immunostaining using HeLa cells

2.5.3.1. Immunocytochemistry of HeLa cells using p16/Ki-67 dual antibody

Immunostaining of HeLa cells was done using CINtec Plus Kit according to manufacturer's instructions. First the cells were fixed in absolute alcohol followed by washing in TBS buffer and treatment with antigen retrieval buffer for exposing the antigenic sites. Then a ready to use primary antibody mix of a mouse monoclonal (E6H4™ clone) and a rabbit monoclonal antibody (274-11AC3 clone) targeted against human p16INK4a(p16) protein and Ki-67 protein respectively were added. After 45 minute incubation followed by washing with TBS, a polymer reagent conjugated with horse radish peroxidase (HRP) and affinity purified goat anti-Mouse Fab' antibody fragments were directed for p16 detection. Polymer re agent conjugated with alkaline phosphatase and affinity purified goat anti-rabbit Fab' antibody

fragments were directed for Ki-67 detection. The counter stain used was alcohol free hematoxylin followed by wet mounting of the sample followed by DPX permanent mounting.

2.5.3.2. Immunocytochemistry of HeLa cells using EGFR antibody

The HeLa cells were fixed in absolute alcohol, kept in methanol for 15 min followed by 70% ethanol, distilled water for 5 min each and sodium deoxy cholate for15 min.Washing was done with distilled water for 5min followed by treatment with antigen re trieval solution made of trisodiumcitrate. After blocking the peroxidase activity and protein block treatment, primary EGFR antibody was added and kept for overnight incubation. Next day postprimary block was added and then washed followed by incubation with novolink polymer. The DAB chromogen was then added for 5 min and then washed with distilled water. The counterstaining was done with haematoxylin, dehydrated using a series of treatment of the slide with 50%ethanol, 95%ethanol, absolute ethanol and Xylene. Finally permanent mounting was done using DPX.

2.5.4. Cell viability assay

HeLa cells were seeded at a density of 5000 cells/well in a 96 well plate and incubated at 37 °C for sufficient growth. The AuNPs, Au-NPs-SQ-dye, Au-NPs-SQ-dye-PEG construct (3.44 x 10^{-5} µM of Au-NPs on 30 µM of SQ-dye), SQ-dye (30 µM) were added to the wells separately. The treated cells were then incubated for 24

h. The cells were exposed to MTT at a concentration of 50 mg/well and incubated for 3h.The working solution of MTT was prepared in Hanks balanced salt solution (HBSS). After viewing formazan crystals under the microscope, the crystals were solubilized by treating the cells with DMSO: isopropanol at a ratio of 1:1 for 20 min at 37 °C. Finally the absorbance was measured by plate reader at 570 nm. The relative cell viability in percent was calculated as: Absorbance of treated/Absorbance of control x 100.

2.6. References

(1)   Arunkumar, E.; Fu, N.; Smith, B. D. *Chemistry*, **2006**, *12*, 4684.

(2)   Ntziachristos, V. *Annu. Rev. Biomed. Eng.* **2006**, *8*, 1.

(3)   Leblond, F.; Davis, S. C.; Valdés, P. A.; Pogue, B. W. J. *Photochem. Photobiol. B, Biol.***2010**, *98*, 77.

(4)   Romeo, M. J.; Boydston-White, S.; Matthäus, C.; Miljković, M.; Bird, B.; Chernenko, T.; Lasch, P.; Diem, M. *In Handbook of Vibrational Spectroscopy*; John Wiley &Sons, Ltd: **2006**.

(5)   Bassan, P.; Byrne, H. J.; Bonnier, F.; Lee, J.; Dumas, P.; Gardner, P. *Analyst* **2009**, *134*, 1586.

(6)   Mohlenhoff, B.; Romeo, M.; Diem, M.; Wood, B. R. *Biophys. J* .**2005**, *88*, 3635.

(7)   Mattley, Y.; Allen, M. W. Optik & Photonik **2013**, *8*, 44.

(8)   Huang, H.; Wang, J. H.; Jin, W.; Li, P.; Chen, M.; Xie, H. H.; Yu, X. F.; Wang,

H.; Dai, Z.; Xiao, X.; Chu, P. K. *Small*, **2014**, *10*, 4012.

(9) Maiti, K. K.; Dinish, U. S.; Samanta, A.; Vendrell, M.; Soh, K.-S.; Park, S.-J.;

Olivo, M.; Chang,Y.-T. *Nano Today*, **2012**, *7*, 85.

(10) Katrin, K.; Harald, K.; Irving, I.; Ramachandra, R. D.; Mi chael, S. F. *J. Phys.:*

Condens.Matter. **2002**, *14*, R597.

(11) Yap, F. L.; Thoniyot, P.; Krishnan, S.; Krishnamoorthy, S. *ACS Nano* **2012**, *6*,

2056.

(12) U. S, Dinish.; Fu, C. Y.; Soh, K. S.; Ramaswamy, B.; Kumar,A.; Olivo, M.

Biosens.Bioelectron. **2012**, *33*, 293.

(13) Chung, E.; Lee, J.; Yu, J.; Lee, S.; Kang, J. H.; Chung, I. Y.; Choo, J. *Biosens.*

Bioelectron.**2014**, *60*, 358.

(14) Xiao, L.; Harihar, S.; Welch, D. R.; Zhou, A. *Anal. Chim. Acta* **2014**, *843*, 73.

(15) Kudelski, A. *Chem. Phys. Lett.* **2005**, *414*, 271.

(16) Silva, W. R.; Keller, E. L.; Frontiera, R. R. *Anal. Chem.* **2014**, *86*, 7782.

(17) Amendola, V.; Meneghetti, M. *Adv. Funct. Mater*. **2012**, *22*, 353.

(18) Wang, y.; Yan, B.;Chen, L. *Chem. Rev.***2013**, *113*, 1391.

(19) Samanta, A.; Maiti, K. K.; Soh, K.-S.; Liao, X.; Vendrell, M.; Dinish, U. S.;

Yun, S.-W.; Bhuvaneswari, R.; Kim, H.; Rautela, S.; Chung, J.; Olivo, M.;

Chang, Y.-T. *Angew. Chem. Int.Ed*. **2011**, *123*, 6213.

(20) Maiti, K. K.; Samanta, A.; Vendrell, M.; Soh, K.-S.; Olivo,M.; Chang, Y.-T.

Chem.Commun. **2011**, *47*, 3514

(21) Stokes, R.J.; Ingram, A.; Gallagher, J.; Armstrong, D.R.; Smith W.E.; Graham,

D. *Chem.Commun.* **2008**, 5, 567.

(22) Kim, S.-H.; Kim, J.-H. Cui, J.-Z.; Gal, Y.-S.; Jin, S.-H.; Koh,K. *Dyes Pigments* **2002**, *55*,1.

(23) Yum, J.-H.; Walter, P.; Huber, S.; Rentsch, D.; Geiger, T.; Nüesch, F.; De Angelis, F.; Grätzel, M.; Nazeeruddin, M. K. *J. Am.Chem. Soc.* **2007**, *129*, 10320.

(24) Shafeekh, K. M.; Das, S.; Sissa, C.; Painelli, A. J. *Phys. Chem.B.* **2013**, *117*, 8536.

(25) Maeda, T.; Nitta, S.; Na kao, H.; Yagi, S.; Nakazumi, H. *J. Phys. Chem. C.* **2014**, *118*,16618.

(26) Smits, E. C. P.; Setayesh, S.; Anthopoulos, T. D.; Buechel, M.; Nijssen, W.; Coehoorn, R.; Blom, P. W. M.; de Boer, B.; de Leeuw, D. M. *Adv. Mater.* **2007**, *19*, 734.

(27) Liu, L. H.; Nakatani, K.; Pansu, R.; Vachon, J. J.; Tauc, P.; Ishow, E. *Adv. Mater.* **2007**, *19*, 433.

(28) Gassensmith,J.J.; Baumes,J.M.; Smith,B.D. *Chem. Commun.***2009**, 6329

(29) Sreejith, S.; Ma, X.; Zhao, Y. *J. Am.Chem. Soc*. **2012**, *134*,17346.

(30) Feng, Y.; Wang, Y.; Wang, H.; Chen, T.; Tay, Y. Y.; Yao, L.;Yan, Q.; Li, S.; Chen, H. *Small* **2012**, *8*, 246.

(31) Gaufres E; Tang, N. Y. W.; LapointeF; CabanaJ; Nadon, M. A.; CottenyeN; RaymondF; SzkopekT; MartelR *Nat Photon*. **2014**, *8*, 72.

(32) Painter, J. T.; Clayton, N. P.; Herbert, R. A. *Toxicol pathol.***2010**, *38*, 131.

33) Wentzensen, N.; Schwartz, L.; Zuna, R. E.; Smith, K.; Ma thews, C.; Gold, M. A.; Allen, R. A.; Zhang, R.; Dunn, S. T.;Walker, J. L.; Schiffman, M. *Clin. Cancer Res.* **2012**, *18*, 4154.

(34) Matos, L. L.; Trufelli, D. C.; de Matos, M. G.; da Silva Pinhal, M. A. *Biomark Insights* **2010**, *5*, 9.

(35) Conesa-Zamora, P.; Torres-Moreno, D.; Isaac, M. A.; Pérez- Guillermo, M. *Exp. Mol. Pathol.* **2013**, *95*, 151.

(36) Schmidt, D.; Bergeron, C.; Denton, K. J.; Ridder, R.; for the European, C. C. S. G. *Cancer Cytopathol.* **2011**, *119*, 158.

(37) Waldstrøm, M.; Christensen, R. K.; Ørnskov, D. *Cancer Cytopathol.* **2013**, *121*, 136.

(38) Avirah, R. R.; Jayaram, D. T.; Adarsh, N.; Ramaiah, D. *Org. Biomol. Chem*., **2012**, *10*, 911.

(39) Xu, Y.; Li, Z.; Malkovskiy, A.; Sun, S.; Pang, Yi. *J. Phys. Chem. B.***2010**, *114,* 8574.

(40) Sajanlal, R.P.; Steven, M.H.; Mahmoud, A. M.; Mostafa, A.; Sayed, EI. *J. Am.Chem. Soc*. **2014***, 136,* 15961.

(41) Maiti, K. K.; Dinish, U. S.; Fu, C. Y.; Lee, J.-J.; Soh, K.-S.; Yun, S.-W.; Bhuvaneswari, R.; Olivo, M.; Chang, Y.-T. *Biosens. Bioelectron*. **2010**, *26*, 398.

(42) Lee, S.; Chon, H.; Lee, M.; Choo, J.; Shin, S. Y.; Lee, Y. H.; Rhyu, I. J.; Son, S. W.; Oh, C. H. *Biosens. Bioelectron.* **2009**, *24*,2260.

(43) Yang, L. L.; Mao, H.; Wang, Y. A.; Cao, Z. H.; Peng, X. H.; Wang, X. X.;

Duan, H. W.; Ni, C. C.; Yuan, Q. G.; Adams, G.; Smith, M. Q.; Wood, W. C.;

Gao, X. H.; Nie, S. M. *Small.* **2009**, *5*, 235.

(44) Samanta, A.; Maiti, K. K.; Soh, K.-S.; Liao, X.; Vendrell, M.; Dinish, U. S.;

Yun, S.-W.; Bhuvaneswari, R.; Kim, H.; Rautela, S.; Chung, J.; Olivo, M.;

Chang, Y.-T. *Angew. Chem.Int. Ed.* **2011**, *50*,6089.

Chapter 3

Investigation of Apoptotic Events at Molecular Level Succeeding Theranostic SERS Nanoprobe guided Targeted Photothermal Chemotherapy
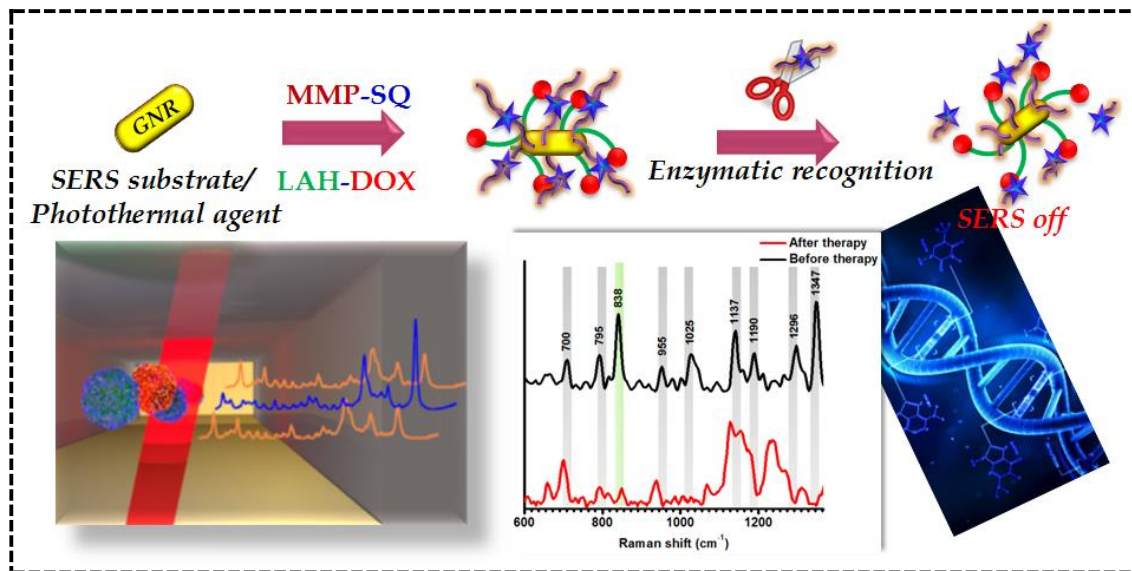
3.1. Abstract

In this chapter, the structural and functional alterations of cellular components during cell death induced by a targeted theranostic SERS-nanoprobe exerting synergistic photothermal-chemotherapy is described.   Localized photothermal-chemotherapy was initiated by gold nanorod (GNR) conjugated to (i) Raman signature molecule (RSM) i.e. squaraine dye (SQ) attached target specific peptide substrate susceptible to matrix metalloproteinases (MMP2 & MMP9), over-expressed in extracellular matrix of cancer cells; (ii) secondly, lipoic acid appended

*doxorubicin, conjugated through acid labile hydrazone linkage (LAH-DOX). The designed theranostic SERS-nanoprobe **MMP-SQ@GNR@LAH-DOX** acts as surface enhanced Raman scattering (SERS) "on/ off" probe in peace with the vicinity of MMP protease and prompted apoptotic cell death on low-power-density 808 nm laser irradiation (0.1 W/cm²) in MMP over-expressing cancer cells. Profiling the biochemical and molecular events during cell death induced by therapy is challenging and requires meticulous efforts with the assistance of ultra-sensitive techniques. The variations in chemical environments and associated modifications of cellular components during therapy were successfully traced through SERS platform. Disappearance of the significant SERS peak at 838 cm⁻¹ which corresponds to the phosphodiester backbone of DNA was perfectly in accordance with ladder formation of DNA isolated after photothermal chemotherapy. Although further detailed investigations are necessary, the results of current study confirmed the potential of SERS to investigate biochemical processes during cell death induced by different causes and thus to monitor the therapeutic efficiency through an insightful approach.*

3.2. Introduction

Cancer detection, treatment and effective follow up of therapeutic responses prolonged to be significant hurdles over the past few decades.[1,2] Although an assortment of strategies exist to screen the progress of treatment, many of them are unable to offer a clear picture of the structural alterations of cellular components during therapy from its molecular perspectives. A

sensitive and consistent technique capable of providing an in-depth understanding of the modifications at cellular level during therapy can offer new insights to optimize therapeutic efficiency. Recently surface enhanced Raman scattering (SERS) technique with its ultrahigh sensitivity and multiplexing capability which is lacking for conventional light and magnet based imaging techniques has came out as an ideal diagnostic modality capable of unravelling the bio-molecular snapshots of cellular events.[3] The fingerprint information attained from Raman micro-spectra were explored for the better understanding of biochemical and pathological transforms in cells.[4,5] Real-time monitoring of cellular responses of cancer cells towards UV irradiations through SERS platform was recently reported by El Sayed and co-workers.[6] The impact of SERS in biomedical field is expected to be ground breaking.

The multi-functional roles played by nanomaterials makes it possible to incorporate SERS image-guided diagnosis and therapy within a reasonably simple nanoplatform.[7] Most of the noble metal nanoparticle (NP) based SERS substrates namely, gold nanorod (GNR),[8,9] gold nanocage[10,] and gold nanopopcorn[11] can play the dual role as excellent photothermal agents[12]. Photothermal therapy (PTT) is a promising cancer treatment where plasmonic nanoparticles convert NIR light to heat leading to hyperthermia induced cell death. When plasmonic nanoparticles are irradiated with resonant light, the electron excitation causes fast non-equilibrium heating.[13] The first excitation of electrons is

followed by relaxation at sub-picosecond timescales through electron–electron scattering which causes a quick enhancement in the surface temperature of the metal nanoparticles **(Scheme 3.1)**. The quick heating process is followed by cooling to equilibrium by energy exchange between the electrons and the lattice phonons. Then the lattice cools via phonon–phonon coupling resulting in heat dissipation into the medium surrounding the nanostructure. This ultimately results in a rapid temperature increase of the biological medium which accounts for cell death.
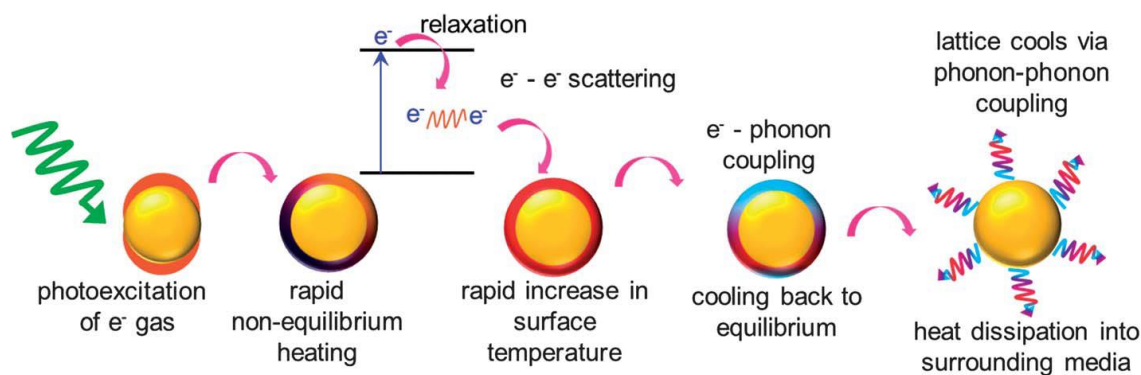
Scheme 3.1. Schematic representation of the principle of photothermal conversion of light to heat by metal nanoparticles.[13]

Massive efforts have been made to analyze the cell death profile subsequent to photothermal therapy. Recently El-Sayed and co-workers demonstrated real time SERS monitoring of alterations in cellular components during cell death resulted by PTT.[14] Presently, Photothermal therapy using gold NPs for cancer treatment is in clinical trials.[15] But, for diffused cancerous cells localised photothermal cytotoxicity is not sufficient for complete tumor ablation. Hence

the integration of different therapeutic strategies with different mechanisms is a promising strategy to enhance the therapeutic efficacy.[15,16] The spatio-temporal synchronization of chemotherapy and PTT[17,18] can be adopted as an insightful approach for enhancing treatment efficacy.[19,20] The synchronization of PTT with chemotherapy was accounted to regress, multidrug resistance and arouse the therapeutic efficiency in drug resistant tumors.[21,22]

Multifunctional theranostic nanoconstructs which can specifically recognize cancer cells with negligible adverse effects on normal cells and tissues need intelligent fabrication strategies with tumor targeting ligands. Matrix metalloproteinases (MMP) is a group of zinc-dependent proteins vastly articulated in a variety of human cancers and is generally considered as a potential target for cancer detection.[23,24] An efficient fluorescent imaging probe for the specific recognition of MMP and simultaneous PTT[23] was fabricated by Ahn and co-workers. Detection of MMPs can offer valuable information in cancer progression and an assortment of imaging modalities were designed with this intention.[25] In this context, a targeted theranostic nanoprobe which can spot MMP expressing cancer cells selectively were constructed. The nanoprobe designated as **MMP-SQ@GNR@LAH-DOX** can perform targeted photothermal-chemotherapy by integrating the photothermal effects of GNRs and site specific cytotoxic action of anticancer agent doxorubicin (DOX).
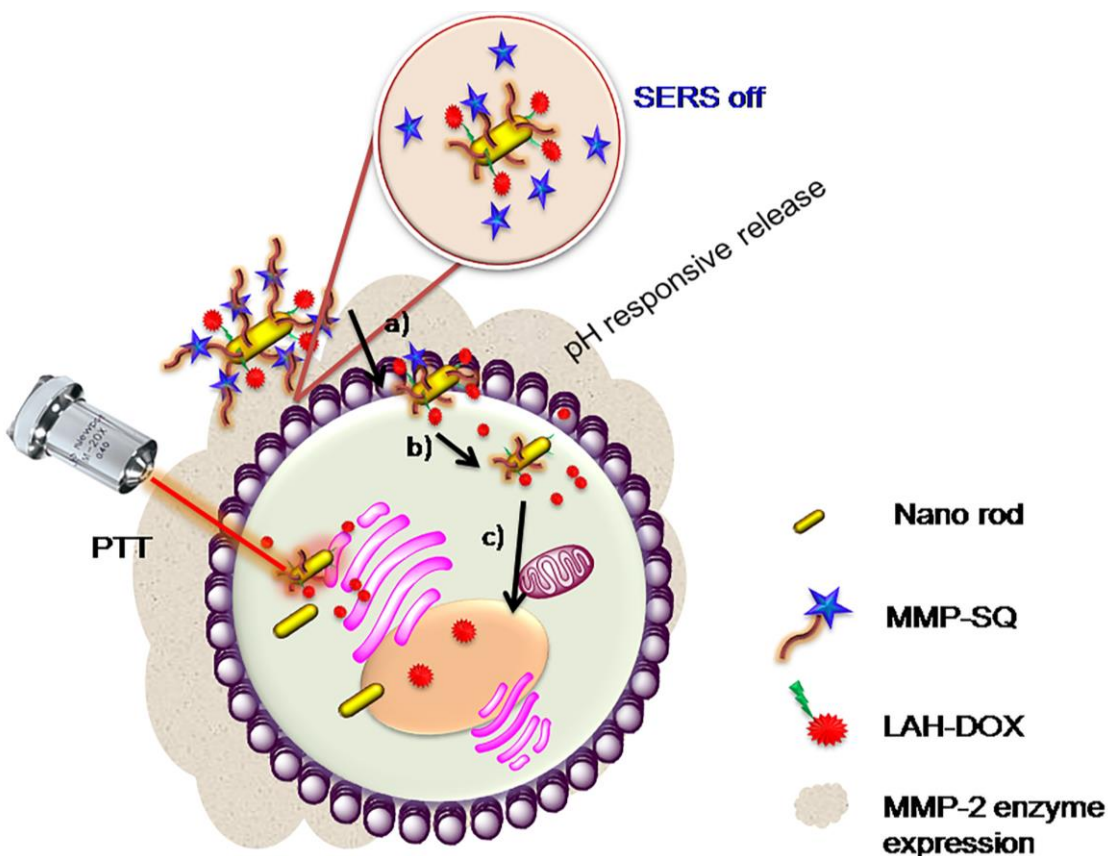
Scheme 3.2.Schematic representation of targeted theranostic probe for simultaneous imaging and photothermal-chemotherapy.(a) endocytosis of LAH-DOX@GNR, (b) DOX release at lysosomal pH and (c) successful penetration and colocalization of DOX into the nucleus.

SERS guided theranostic nanoprobe for the treatment of MMP over-expressing cancer cells has not been reported till date. In this work, multiple functions were incorporated into a single nano platform and meticulous investigations were performed for tracing the molecular events promoted by targeted theranostic nanoprobe utilising the strong diagnostic platform afforded

by SERS. The style of action of the theranostic nanoprobe for imaging and photothermal-chemotherapy is elucidated in **scheme 3.2**.

3.3. Results and Discussion

3.3.1. Synthesis and Characterization of MMP peptide substrate attached SQ & LAH-DOX tethered GNRs, (MMP-SQ@GNR@LAH-DOX)

The construction of nanoprobe has been initiated with the synthesis of squaraine dye (SQ) as Raman reporter by the condensation reaction of a mixture of squaric acid and 2,3,3-trimethyl indoline in toluene-butanol eutectic mixture with continuous removal of water using Dean Stark apparatus.[26,27] MMP peptide substrate with the specified amino acid sequence Pro-Leu-Gly-Leu-Ala-Gly-Cys was synthesized by solid phase peptide synthesis (SPPS),[28] which was further conjugated to SQ free amine terminal by amide coupling to generate SQ attached MMP peptide substrate (MMP-SQ).To obtain a rapid response to the lower pH of acidic organelles, we have introduced an acid labile hydrazone linker between the doxorubicinyl group and lipoic acid moiety denoted as LAH-DOX. The detailed characterizations of the intermediates of MMP-SQ and LAH-DOX were carried out by ^{1}H NMR and ESIMS. MMP-SQ and LAH-DOX was anchored onto the surface of GNR via strong Au-S covalent interactions generating **MMP-SQ@GNR@LAH-DOX** (**Figure 3.1A**), which was purified by repeated centrifugation to remove free LAH-DOX and unbound MMP-SQ. The morphology of GNR was examined with HR-TEM (**Figure 3.1B**). HR-TEM images showed uniformly dispersed GNRs of aspect ratio approximately 4 (length/width). By tuning the aspect ratio, the strong localized

surface plasmon resonance (LSPR) was adjusted to the NIR region to minimize absorption by tissue and maximize laser (808 nm) absorption by GNR.
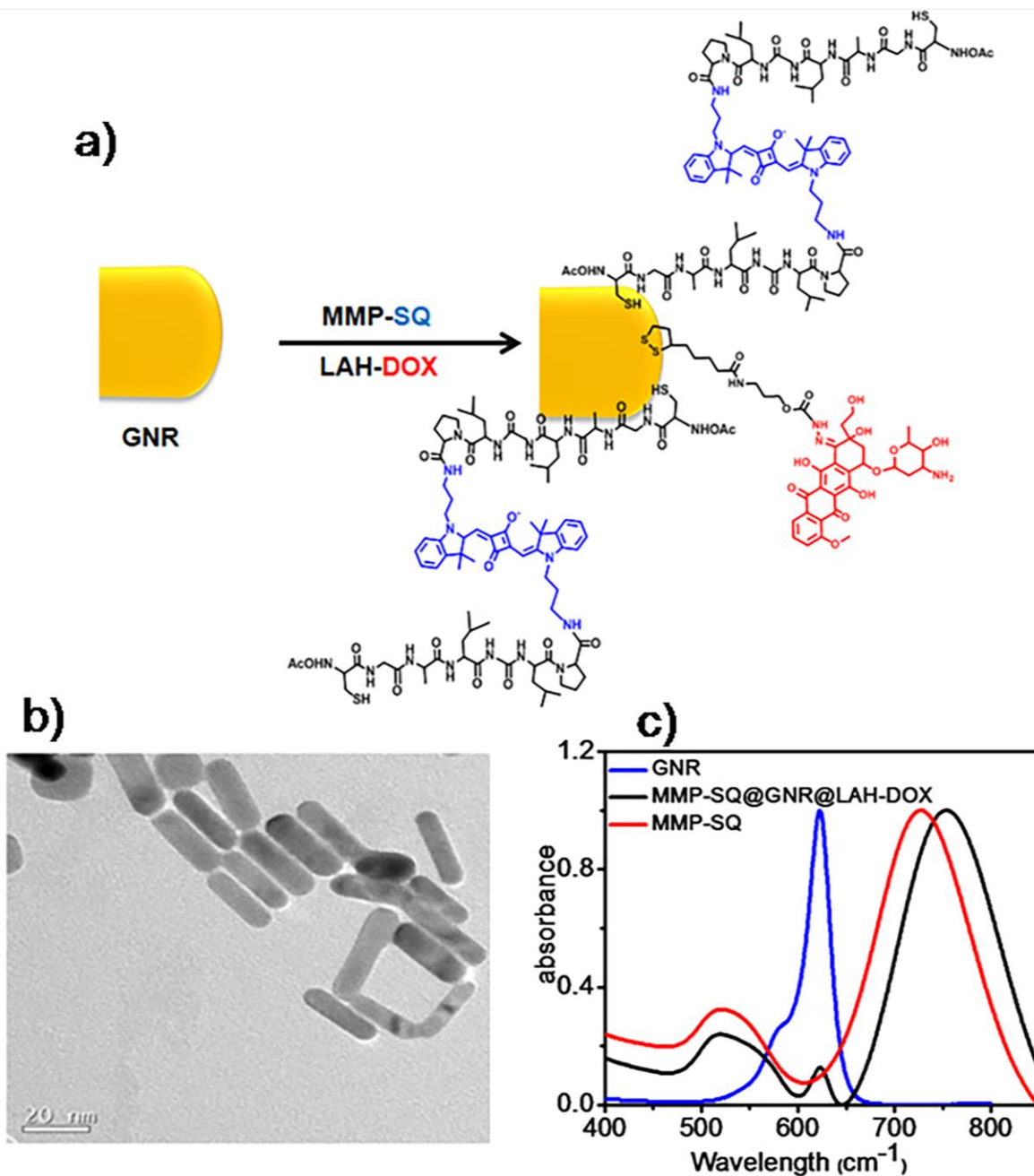
Figure 3.1.a) Synthetic route towards MMP-SQ@GNR@LAH-DOX, b) TEM image of GNR and c) UV-Vis spectra of MMP-SQ, GNR andMMP-SQ@GNR@LAH-DOX.

No self aggregation was observed during the conjugation of MMP-SQ or LAH-DOX

to the surface of GNRs, and the DOX-tethered GNRs could be easily re-suspended in

aqueous solution. Both the longitudinal and transverse LSPR of the GNR were

slightly red shifted after conjugation. The absorption band corresponding to MMP-

SQ centered at 620nm, remains consistent with the spectra of **MMP**-

SQ@GNR@LAH-DOX, which indicated the successful conjugation of MMP-SQ on

the surface of GNR (**Figure 3.1C**).

3.3.2. SERS spectral evaluation of MMP-SQ@GNR@LAH-DOX
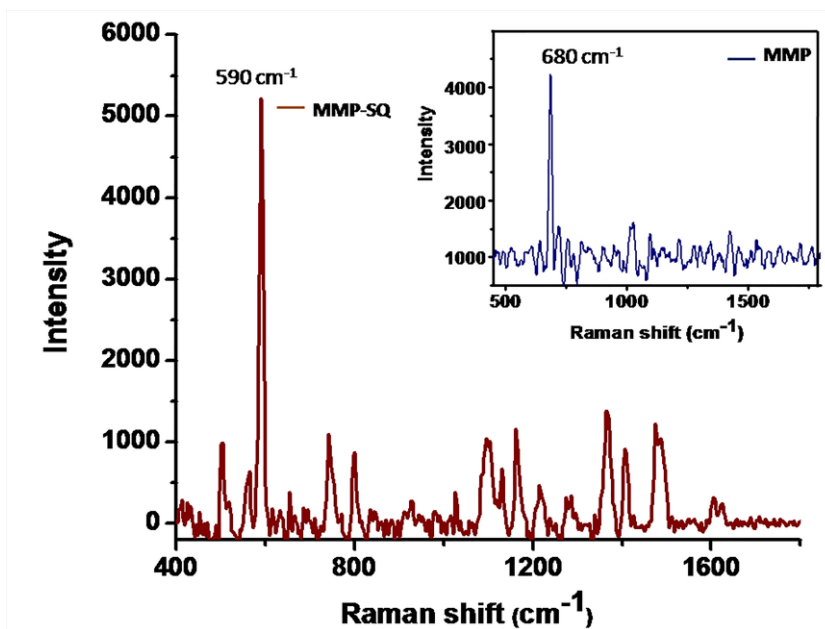
Figure 3.2: SERS spectrum of MMP-SQ. Inset SERS spectrum of MMP peptide substrate
alone.

SERS spectral features of MMP-SQ@GNR@LAH-DOX were evaluated under

confocal Raman microscope at 633 nm laser wavelength (**Figure 3.2**). The SERS

spectrum of MMP-SQ@GNR@LAH-DOX consisted of peaks from MMP peptide

substrate and attached squaraine dye. The shift in position of secondary amide NH deformation vibration of MMP peptide substrate at 680 cm^{-1} to 590 cm^{-1} confirms the successful conjugation of MMP peptide substrate with SQ. Additionally, the peaks at 741, 1093, 1474 cm^{-1} corresponds to C-H out of plane bending, aromatic vibration of the polycyclic structure, and g anti-symmetric stretching (CH$_3$-C) respectively. The peak appeared at 1366 cm^{-1} resembled the typical stretching vibration of indole rings.[27]

3.3.3. Enzyme recognition of MMP-SQ@GNR through SERS

MMP-SQ@GNR conjugate is believed to be a strong SERS "ON/OFF" nanoprobe. The excellent SERS spectral features exhibited by MMP-SQ@GNR was found to be decreasing in intensity when it approaches target protease because the enzymatic recognition results in the cleavage of the MMP peptide substrate, which ultimately detaches Raman signature molecule (RSM) from GNR surface leading to the gradual decrease in SERS signal intensity. The incubation of MMP-SQ@GNR with activated MMP 2 enzyme (50 ng/mL, 37 ^{0}C, 40 min) resulted in significant decrease in the SERS signal intensity noticeably the peaks at 590 cm^{-1} along with all other characteristic spectral signatures of squaraine dye (**Figure 3.3a**). The decrease in the SERS intensity of MMP-SQ@GNR was induced from the specific cleavage of peptide substrate because no remarkable change in SERS intensity was observed in the presence of the MMP 2 inhibitor (**Figure 3.3b**).
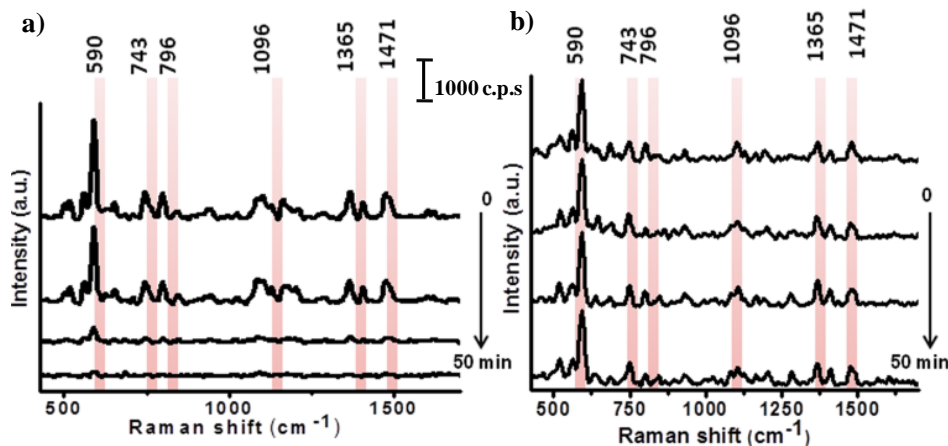
Figure 3.3. SERS spectra of MMP-SQ@GNR at different time intervals measured under confocal Raman microscope. a) in the presence of MMP-2 enzyme b) in the presence of MMP-2 inhibitor.

The enzyme selectivity of MMP-SQ@GNR was evaluated with various other MMP enzymes (MMP 7, 9) by recording SERS spectra in different time intervals after incubating with respective enzymes.
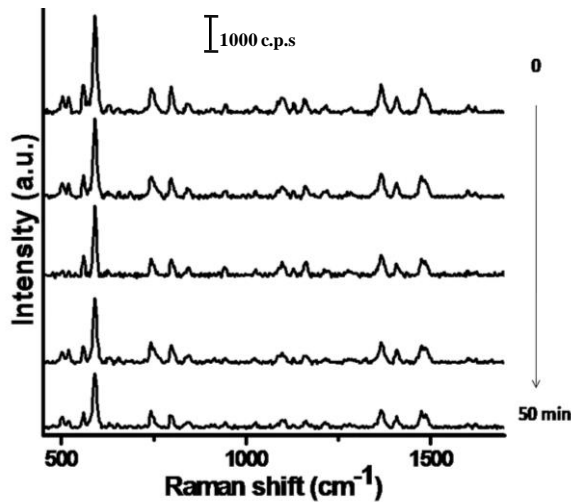
Figure 3.4. SERS spectra of SQ-MMP@GNR in presence of MMP 7 enzyme measured under confocal Raman microscope.

SERS intensity of MMP-SQ@GNR decreased with time on incubation with the respective enzymes at 37 ^{0}C for 50 min (**Figure 3.4 & 3.5).**
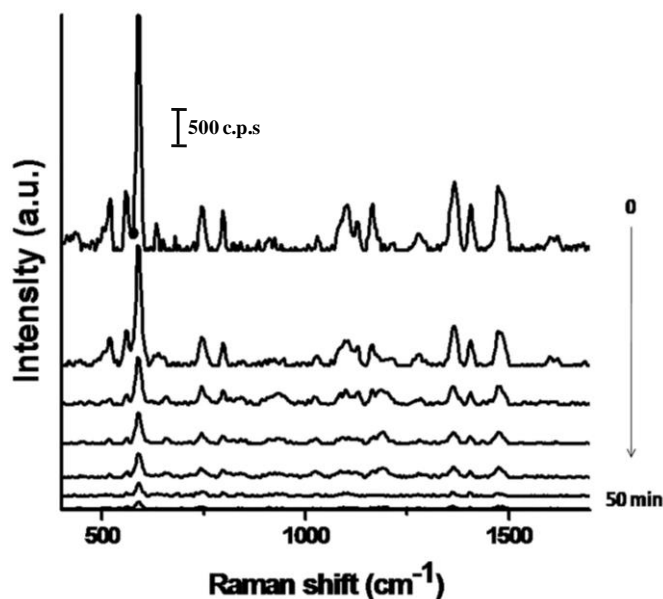
Figure3.5. SERS spectra of SQ-MMP@GNR in presence of MMP-9 enzyme measured under confocal Raman microscope.

3.3.4. Evaluation of the photothermal conversion efficiency of MMP-SQ@GNR@LAH-DOX

After evaluating the sensitivity of the probe towards MMP, photothermal conversion efficiency of **MMP-SQ@GNR@LAH- DOX** was monitored by recording the temperature changes under NIR laser irradiation at 0.1 W/cm^2 with time using a thermocouple integrated multimeter. The temperature of **MMP-SQ@GNR@LAH-DOX**, MMP-SQ@GNR and GNR rapidly increased to 57 ^{0}C within 6 min of laser irradiation, while water alone showed almost no heating effect (**Figure 3.6**). Such an increased variation of temperature can lead to an irreversible damage to tumor cells.
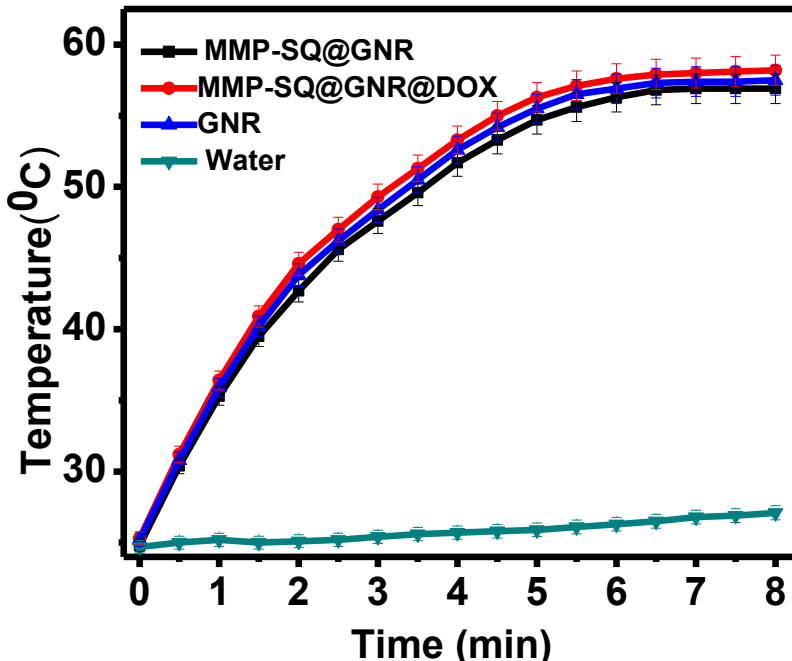
Figure 3.6. Temperature changes of GNR,MMP-SQ@GNR, **MMP-SQ@GNR@ LAH-DOX** irradiated with an 808 nm laser at a power density of 0.1 W/cm^2 as a function of time.

3.3.5. DOX release and Cellular uptake

Then the cleavage of hydrazone bonds of LAH-DOX moiety at lower pH was investigated. The quenched fluorescence of DOX due to the attachment of LAH-DOX on GNR surface recovered gradually once it is detached from GNR.[29] The release of DOX from **MMP-SQ@GNR@LAH-DOX** was monitored with time in acetate buffer (pH 5.0, 0.02 M) which showed a maximum release within 4 h of incubation (**Figure 3.7a**). These data demonstrate the release of DOX from **MMP-SQ@GNR@LAH-DOX** responsive to acidic pH. However, incubation of **MMP-SQ@GNR@LAH-DOX** in phosphate buffered saline (PBS) at pH 7.4 did not exhibit any significant fluorescence recovery even after 12 h of incubation (**Figure 3.7b**).

97
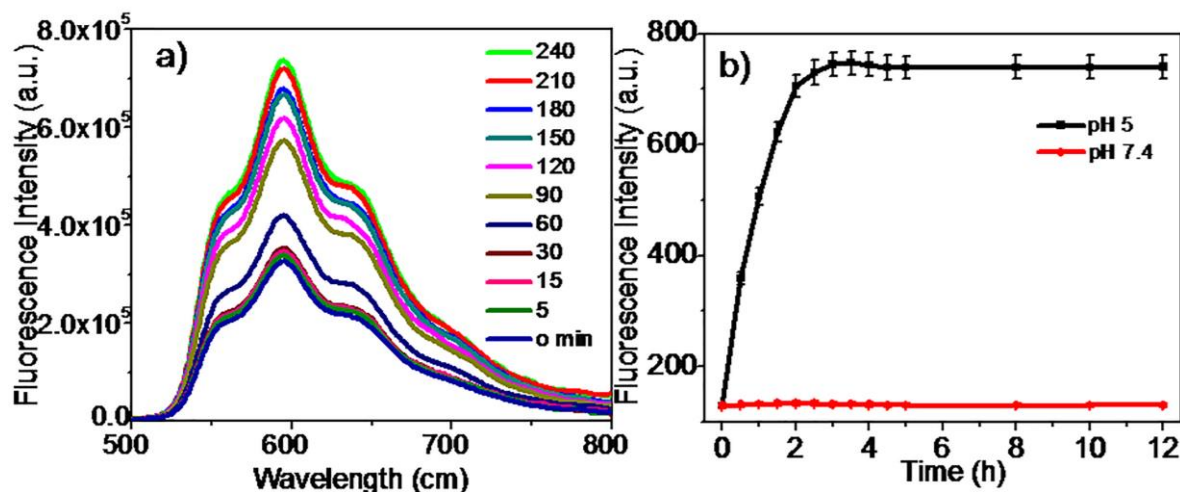
Figure 3.7 a) Emission spectra of **MMP-SQ@GNR@LAH-DOX** in acetate buffer (pH 5.0, 0.02 M) at different time intervals. **b)** DOX release from **MMP-SQ@GNR@LAH-DOX** at pH 5 and pH 7.4.

The cellular uptake and intracellular drug release efficiency of **MMP-SQ@GNR@LAH-DOX** was studied using fluorescence microscopy in human fibrosarcoma cell line HT1080, which over-expresses MMPs **(Figure 3.8).** When **MMP-SQ@GNR@LAH-DOX** approaches the target cells, enzymatic recognition causes the cleavage of MMP peptide substrate followed by the hydrazone bond cleavage from LAH-DOX conjugate occurring in acidic tumor micro environment results in DOX release. HT1080 cells incubated with nanoprobe for 3 h, showed red fluorescence from doxorubicin mainly localized in the nucleus which was confirmed by co-localization with nuclear staining dye Hoechst. The cellular uptake study was also carried out in 3T3-L1 cells which showed minimal expression levels of MMP (**Figure 3.8**). The release of

DOX in acidic pH will exert cytotoxicity at the tumor cells excluding normal cells which will significantly reduce side effects.
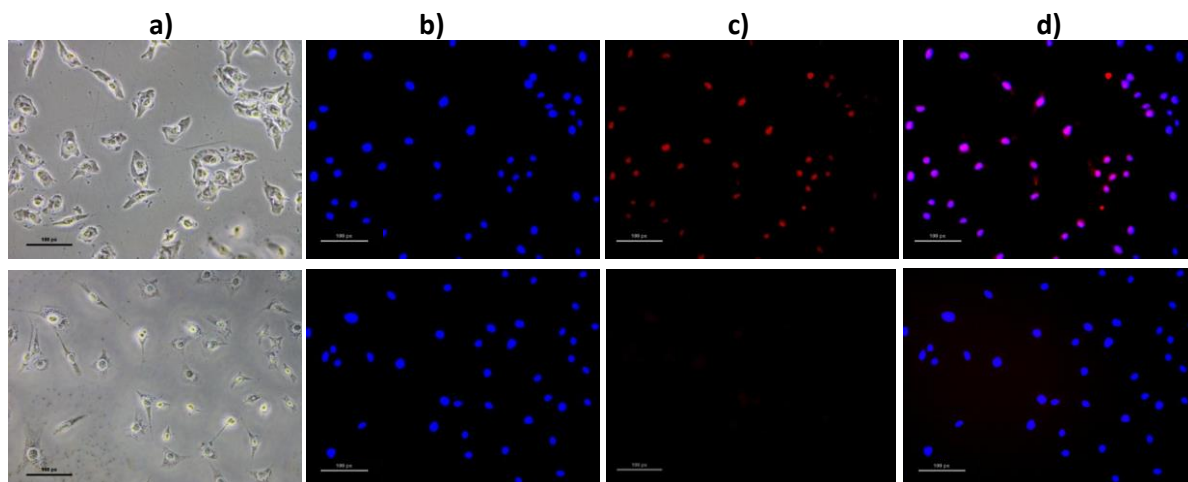
Figure 3.8. Co-localization study in HT1080 (first row) and 3T3-L1 (second row) cells. a) Bright field image b) Nuclei stained with hoechst c) Fluorescence image of cells incubated with **MMP-SQ@GNR@LAH-DOX** after 3 h d) Merged image of b &c.

3.3.6. *In vitro* evaluation of phototoxicity of MMP-SQ @GNR@LAH-DOX

Cytotoxic potential of the nanoconstruct was evaluated in HT1080 cells by MTT assay.
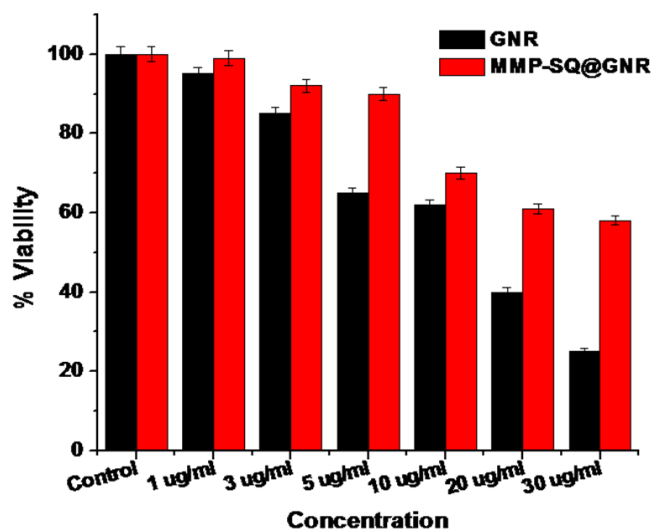
Figure 3.9. HT1080 cell viability after 4 h of incubation with increasing concentration of GNR and MMP-SQ@GNR.

Cytotoxicity of CTAB coated GNR was reduced upon conjugation with MMP-SQ as large portion of CTAB was replaced with MMP-SQ (**Figure 3.9**). Maximum cytotoxic effect was observed upon laser irradiation after 4h incubation with **MMP-SQ@GNR@LAH-DOX.** The superior cytotoxic effect observed under laser irradiation highlights the combined effects of PTT and chemotherapy with MMP targeted nanoprobe (**Figure 3.10a**). However minimum cytotoxic effect was observed in normal fibroblast cell 3T3-L1 incubated with nanoprobe (**Figure 3.10b**).These results indicated the targeting efficiency of **MMP-SQ@GNR@LAH-DOX** towards HT1080 cells.
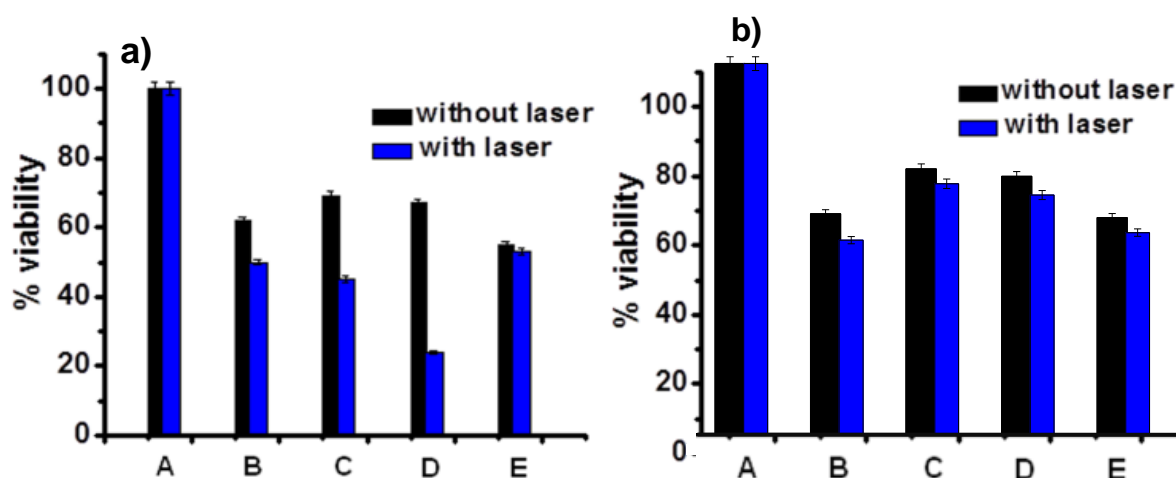
Figure 3.10 In vitro cytotoxicity with or without laser irradiation a) in HT1080 cells b) in 3T3-L1 cells A) control, B) GNR, C) MMP-SQ@GNR, D) MMP-SQ@GNR@LAH-DOX, E)DOX. (808 nm laser, power density 0.1 W/cm^2, irradiation time 2 min).

To investigate the cell death mechanism induced by our SERS-nanoprobe in cancer cells, various apoptotic assays were conducted. In comparison with the respective controls, acridine orange ethidium bromide dual staining displayed a change in colour

from green to yellow/red, which is associated with other apoptotic features such as the presence of apoptotic bodies, damaged cell membrane and nuclear condensation upon treatment (**Figure 3.11a**).
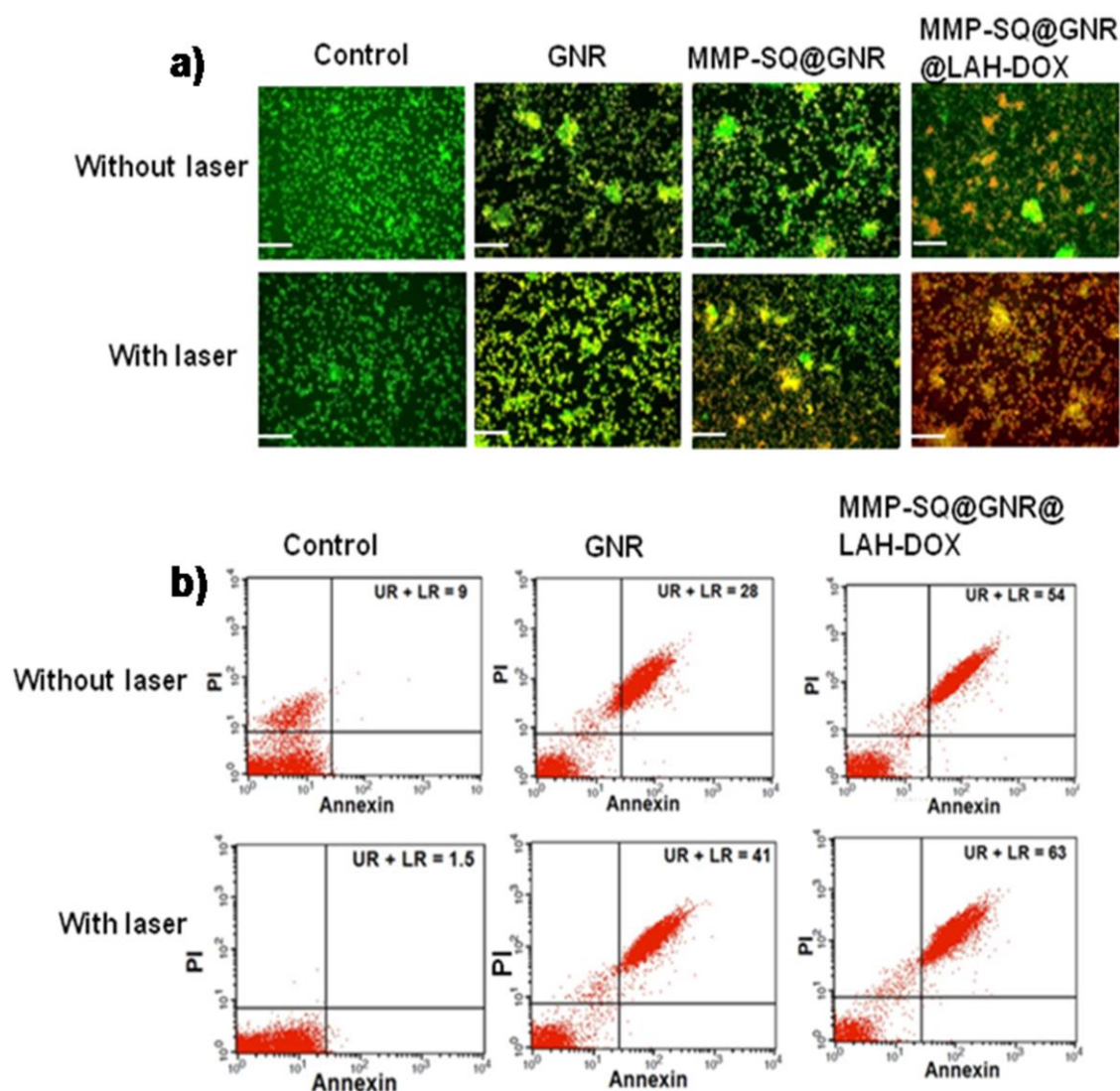
Figure 3.11. a) AO/EtBr dual staining, scale bar corresponds to 200 µm b) Annexin V-FITC staining by flow cytometry.

In concordance with the toxicity study, cells treated with targeted theranostic nanoprobe after irradiation displayed pronounced indications of apoptosis.

Morphological changes observed with staining were further confirmed by Annexin V-FITC assay, using flow cytometry. HT1080 cells were treated with **MMP-SQ@GNR@LAH-DOX** for 4 h with or without laser irradiation, and labeled with PI as well as Annexin V. The percentage of apoptotic cells after drug treatment or negative control are represented in **Figure 3.11b**. There was a significant (P <0.001) increase in the Annexin V positivity with the combined effect of DOX and laser irradiation upon treatment with **MMP-SQ@GNR@LAH-DOX**. The results showed that **MMP-SQ@GNR@LAH-DOX** with laser more significantly induced apoptosis (63%) as compared with those treated by laser alone (9%) or **MMP-SQ@GNR@LAH-DOX** alone (54%). The cytotoxic studies unraveled the superior effect of targeted SERS-nanoprobe upon laser irradiation through the induction of apoptosis.

3.3.7. Investigation of cellular events induced by photothermal chemotherapy

In accordance with the rapid increase in the number of techniques to identify, quantify and characterize cell death more information about the complex cellular processes which takes place during cell death was explored. However, most of these techniques are invasive, require preparation steps such as cell fixation, staining or protein extractions and are generally unable to monitor the mechanism of cell death at molecular level. Raman spectral investigation of the chemical modification has proven to be a new avenue to detect biological changes in molecular level related to cell death phenomenon.[30] SERS is demonstrated as a detection tool to identify the

minute changes in chemical components of organelles inside cells subjected to photothermal chemotherapy. The differential changes of SERS spectral pattern of cells before and after therapy were analyzed (**Figure 3.12**).
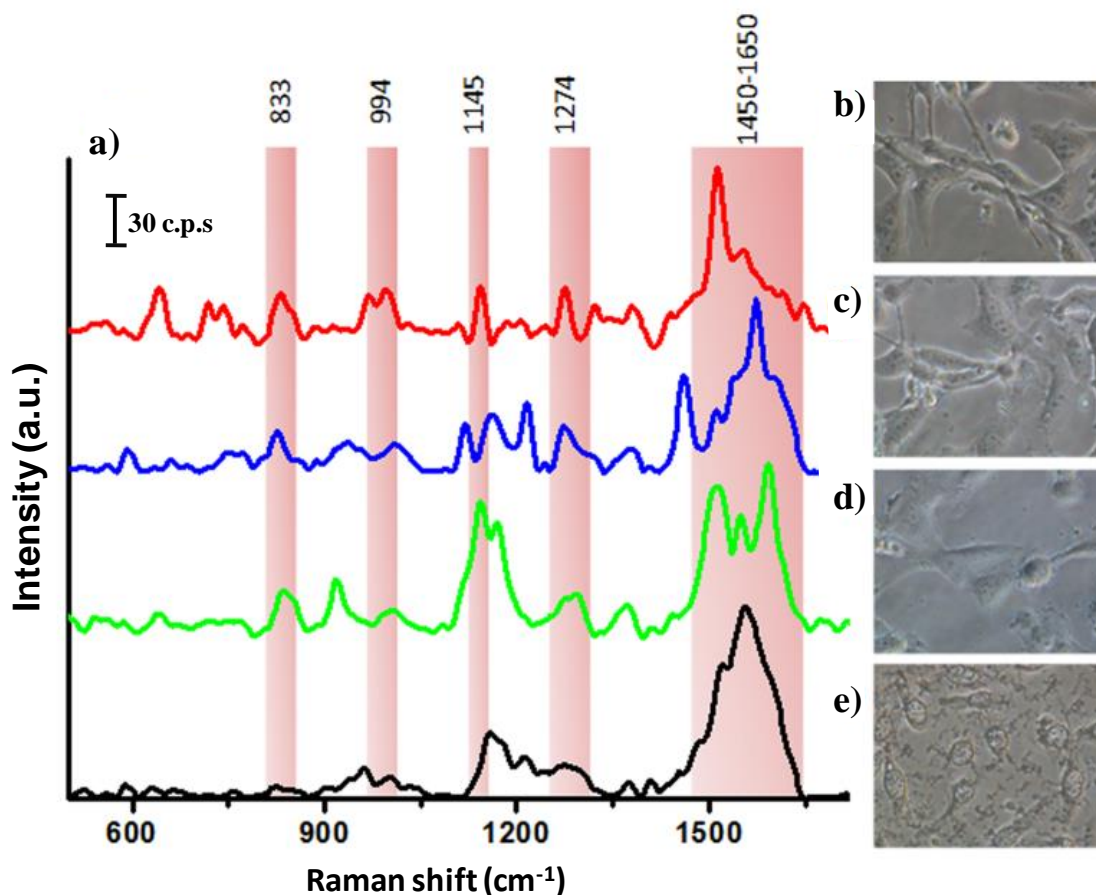
Figure 3.12 a) SERS spectra of HT1080 cells before and after photothermal chemotherapy. Control (red); cells irradiated with laser (blue); cells incubated with **MMP-SQ@GNR@LAH-DOX** for 4 h (green); cells incubated with **MMP-SQ@GNR@LAH-DOX** for 4 h after laser irradiation (black); b), c), d), & e) corresponding bright field images of HT1080 cells.

A closer inspection of the spectra revealed unique modifications in Raman features of several vibrations associated with cellular components. Significant

spectral changes were observed at positions characteristic to nucleic acid and protein vibrations after therapy. The spectra revealed pronounced bands at 833, 994, 1145, 1274, 1450-1650 cm^{-1} which were assigned to O-P-O backbone of DNA, proteins, deoxynucleotides, N_7-H stretching of guanine and adenine respectively.[31]

The molecular vibration most sensitive to cell death was the O-P-O stretching of the DNA at 833 cm^{-1}. The 833 cm^{-1} O-P-O backbone vibration decreased, while the 1450-1650 cm^{-1} N_7-H vibration of guanine and adenine significantly increased after therapy. The increase in guanine and adenine vibrations after therapy is associated with their increased exposure to the plasmonic field of SERS substrate during cell death due to the detachment of DNA from the histone proteins.

Time and dose dependent SERS spectral profile evaluation was carried out to track the apoptosis mechanism (**Figure 3.13-3.15**). The spectral profile of HT1080 cells incubated with **MMP-SQ@GNR@LAH-DOX** with and without laser irradiation were analysed to investigate the effect of chemotherapy and combined photothermal chemotherapy. Chemotherapy was initiated after 4 h of incubation as reflected the gradual decrease of the peak at 838 cm^{-1} where as within 10 min the intensity rapidly diminished as the peak was missing after photothermal chemotherapy. The intensity of 1550-1650 cm^{-1} band increased considerably in all cases and the increase was very fast in case of combined photothermal chemotherapy.
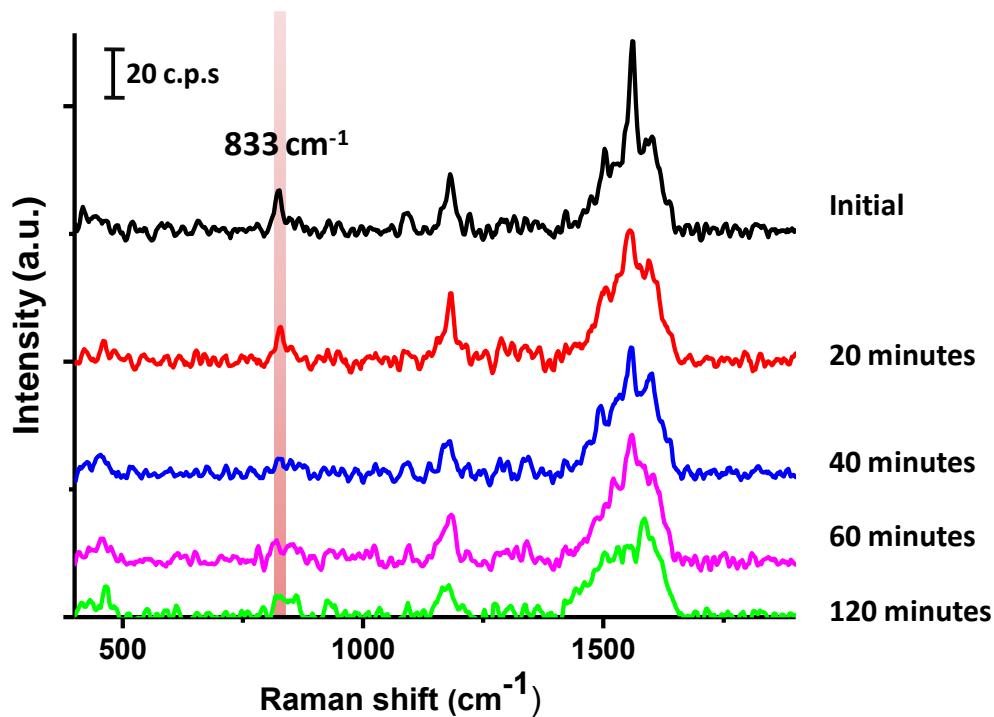
Figure 3.13. Time dependent SERS spectral evaluation of HT1080 cells incubated with **MMP-SQ@GNR@LAH-DOX** for 4 hour.
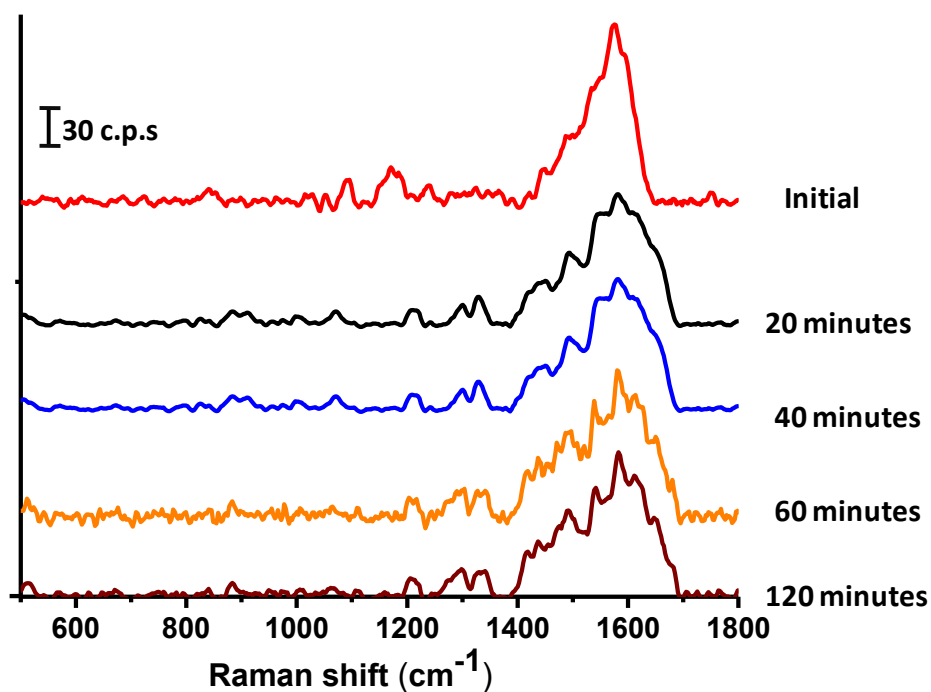
Figure 3.14. Time dependent SERS spectral evaluation of HT1080 cells incubated with **MMP-SQ@GNR@LAH-DOX** for 4 hour after laser irradiation
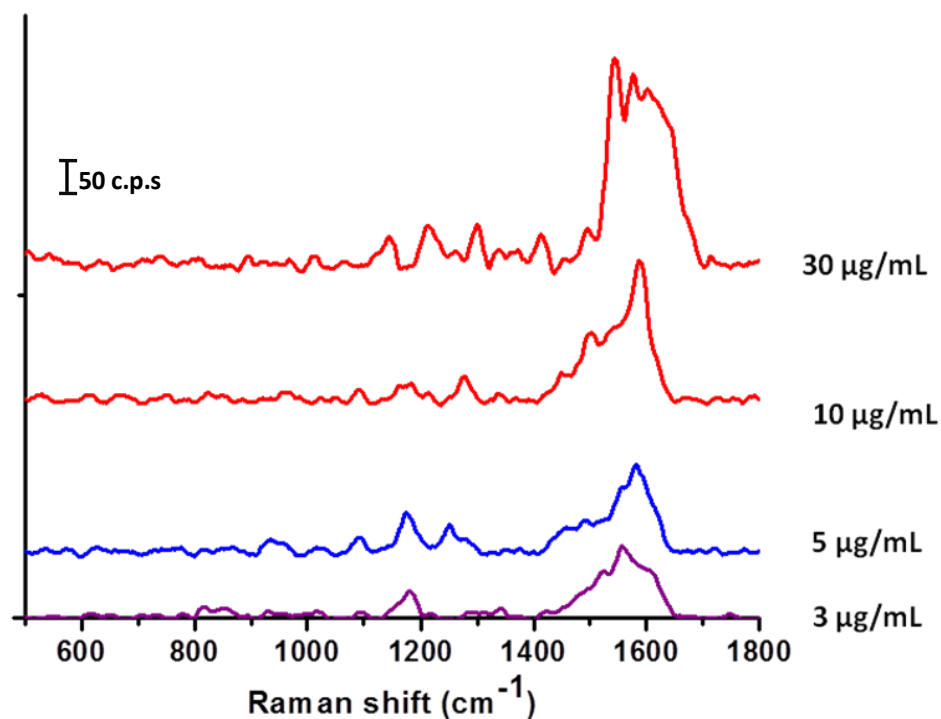
Figure 3.15. Dose dependent SERS spectral evaluation of HT1080 cells incubated with **MMP-SQ@GNR@LAH-DOX** after laser irradiation

It is known that an increase in Raman intensity often occur when DNA bases become unstacked. These alterations suggest the breakage of DNA double strand. In order to validate this assumption, DNA isolated from HT1080 cells before and after photothermal-chemotherapy was investigated for differential SERS spectral pattern. The spectra revealed pronounced bands at 700, 795, 838, 955, 1025, 1137, 1296, 1347, 1405-1568 cm^{-1} which were assigned to the nucleic acid adenine, cytosine, and thymine, O-P-O back bone of DNA, proteins that remained in the DNA extract after isolation, deoxy-nucleotides, C-H deformation of guanine and adenine, N$_7$-H stretch of guanine and adenine

respectively (**Figure 3.16a**). After therapy, the peak at 838 cm^{-1} for O-P-O backbone vibrations decreased, while the 1405-1568 cm^{-1} N$_7$-H vibration of guanine and adenine significantly increased which is in accordance with the result obtained from whole cell study.
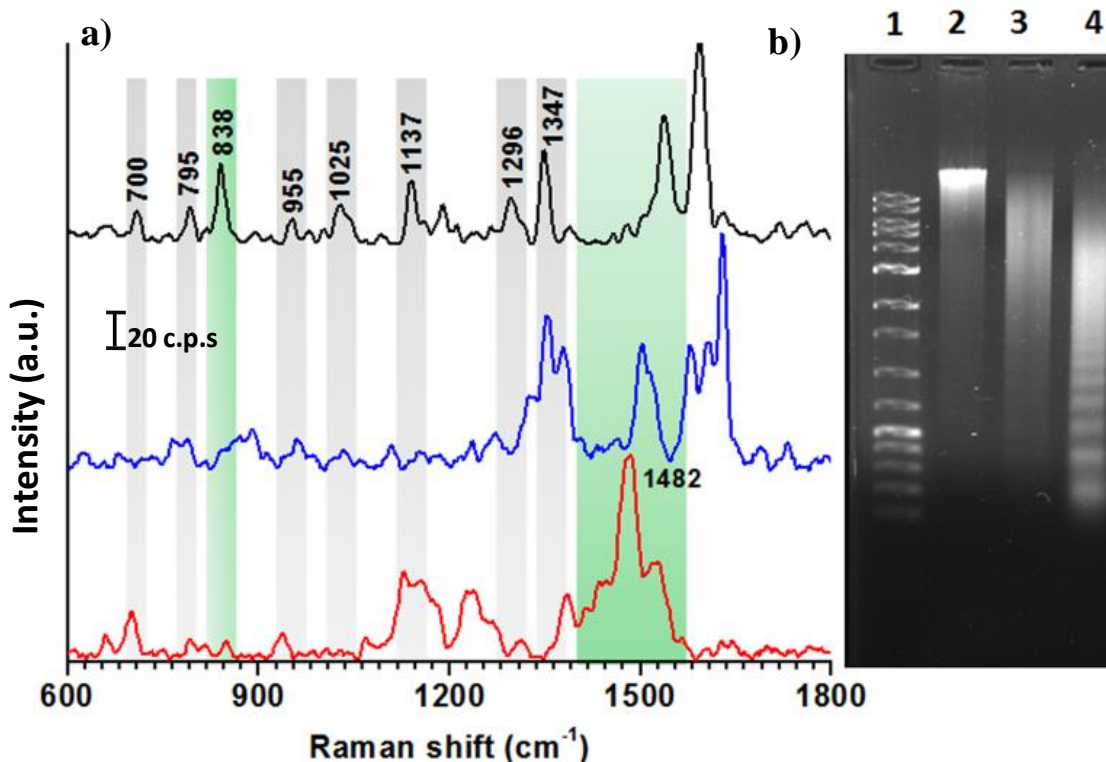
Figure 3.16. a) SERS spectra of DNA isolated from HT1080 cells (black),HT1080 cells incubated with **MMP-SQ@GNR@LAH-DOX** (blue), HT1080 cells incubated with **MMP-SQ@GNR@LAH-DOX** after irradiation with 808 nm laser for 2 min (red). b) Apoptotic DNA fragmentation study after laser irradiation 1) ladder 2) DNA isolated from HT1080 cells without treatment, 3) from cells incubated with GNR 4) DNA isolated from HT1080 cells incubated with MMP-SQ@GNR@LAH-DOX.

So it is evident that apoptotic DNA fragmentation occurred during photothermal-chemotherapy which was monitored effectively through SERS. DNA fragmentation during therapy was further confirmed by agarose gel

electrophoresis (**Figure 3.16b**). The SERS-nanoprobe induced DNA ladder formation during photothermal chemotherapy. DNA laddering is a feature observed in apoptotic event where the DNA is broken down into multiple fragments and viewed by agarose gel electrophoresis. Therefore, a conclusive agreement was established between SERS based monitoring for apoptotic DNA fragmentation and DNA ladder formation.

3.4 Conclusion

In conclusion, the application of the theranostic SERS-nanoprobe, **MMP-SQ@ GNR@LAH-DOX** as an excellent cancer-targeted cytotoxic agent for photothermal-chemotherapy assisted by Raman fingerprinting is revealed in this study. The cumulative impact of radiation and chemotherapeutic agent produced cytotoxicity through programmed cell death mechanism in a targeted fashion. Molecular events during cell death from single whole cell scale to DNA level was investigated through SERS platform. Although further investigations are demanded in a complex multifaceted disease such as cancer, the current study reveal the potential of nanoprobe platform to monitor cell death affected by photothermal-chemotherapy and offers SERS based diagnosis as an upcoming strategy to monitor therapeutic efficiency.

3.5. EXPERIMENTAL SECTION

3.5.1. Synthesis – General Procedures

All the chemicals (synthetic building blocks) and solvents were purchased from Sigma Aldrich, Alfa Aesar, Fluka, Merck, and used without further purification. ^{1}H-NMR spectra were recorded on Bruker Advance 500 NMR spectrometer, and chemical shifts are expressed in parts per million (ppm). Mass spectra were recorded under ESI/HRMS at 61800 resolution using Thermo scientific exactive, mass spectrometer. Surface plasmon absorption spectra were measured on a SpectraMax M2 spectrophotometer (Molecular Devices), and the data analysis was performed using GraphPad Prism 5.0/ Microsoft excel and Origin 7. SERS measurements were carried out in a WI-Tec Raman microscope (WI-tec Inc. Germany, alpha 300R) with a laser beam directed to the sample through 20x objective and a Peltier cooled CCD detector. Samples were excited with 633 nm excitation wavelength laser and Stokes shifted Raman spectra were collected in the range of 400 to 4000 cm^{-1} with 1 cm^{-1} resolution. Prior to every measurement, a calibration with a silicon standard (Raman peak centered at 520 cm^{-1}) was performed. WI-Tec Project plus (v 2.1) software package was used for data evaluation. TEM measurements were performed on a JEOL 2010 high-resolution transmission electron microscope with an accelerating voltage of 200 KV. The sample was prepared by pipetting a drop of the aqueous solution of nanoparticles onto a 230 mesh copper grid coated with carbon and the sample was allowed to dry in air before the measurement. The fluorescence emission

spectra were recorded using a Shimadzu RF-5301PC spectrofluorophotometer with an excitation wavelength at 480 nm for DOX release.

3.5.1.1. Preparation of GNRs

GNRs was prepared by adding around 5 mL of cetyltrimethylammonium bromide (CTAB) solution (200 mM CTAB in deionized water) to 5 mL deionised water. 40 μL of 250 mM $HAuCl_4$ aqueous solution was added to above solution then its colour changes to light yellow. Then 500 μL of 4mM silver nitrate solution was added followed by the addition of 250 μL 80 mM ascorbic acid solution. The solution immediately changes colorless followed by the addition of freshly prepared 5 μL 10 mM sodium borohydride solution and kept undisturbed for 30 min, centrifuged to remove excess CTAB.

3.5.1.2. Synthesis of 1-(3- aminopropyl) – 2, 3, 3- trimethyl – 3H - indolium:
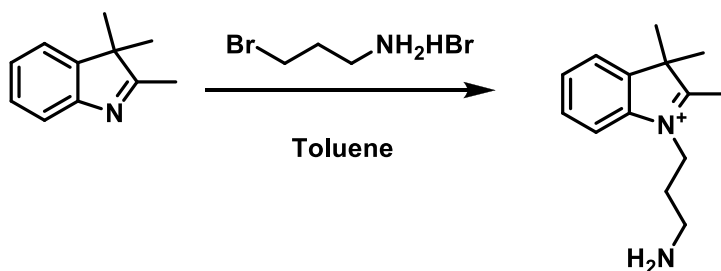
3-bromopoylamine hydrobromide (2.71 g, 12.5 mmol) was added in a seal tube containing 2, 3, 3-trimethyl-3H-indolium (2.2 mL; 12.5 mmol; 1 eqv.) under N_2 atmosphere, and was gently heated up to 110 ^{0}C in an oil bath. The mixture was kept at 120 ^{0}C for 10 h with stirring. After the reaction was completed, the mixture was cooled down to room temperature to form a solid cake that was washed with Et_2O and a chloroform-Et_2O solution. The resulting solid was then dried under high

vacuum to obtain it as a solid (yield 84%). ^{1}H-NMR (500 MHz; CDCl$_3$) δ 7.99–7.66 (m, 1H), 7.26-7.24 (m, 1H), 7.18-7.14 (m, 2H), 3.71 (s, 1H), 3.53-3.47 (m, 2H), 3.23-3.20 (m, 2H), 2.51-2.43 (m, 2H), 1.54 (s, 6H), 1.25 (s, 3H); HRMS (FAB): m/z (C$_{14}$H$_{21}$N$_2^+$) calculated: 217.32, found: 217.3022.

3.5.1.3. Synthesis of 1-(3-(tert-butoxycarbonylamino) propyl)-2, 3, 3 -trimethyl-3H-indolium:
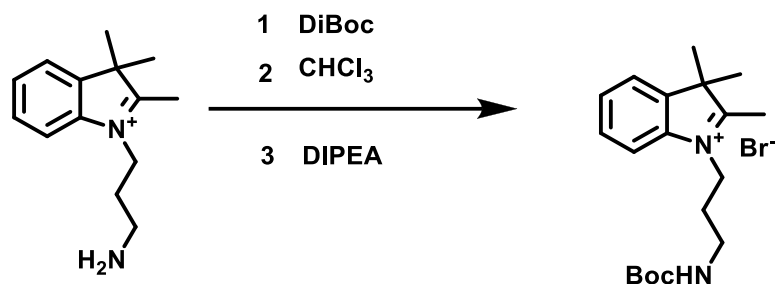
1-(3-aminopropyl) – 2, 3, 3- trimethylindolium (4 g; 18.43 mmol) and di-tert-butyl dicarbonate (10.1 g; 46.1 mmol) were added to a mixture of dry chloroform and diisopropyl ethylamine. The reaction mixture was gently heated to reflux temperature and stirred for 4 h. Afterwards, the organic layer was extracted with Et$_2$O, dried over anhydrous Na$_2$SO$_4$, and concentrated under reduced pressure. Purified the crude residue on a silica gel column using dichloromethane and methanol. Then the product is obtained as a brown liquid (yield: 72%). ^{1}H NMR (500 MHz; CDCl$_3$): δ 7.12 -7.0 7 (m, 2H), 6.76 (t, 1H, J = 7.5 Hz), 6.52 (d, 1H), 4.62 (s, 1H), 3.85 (t, 2H, J = 10 Hz), 3.27 (d, 2H, J = 5 Hz), 1.57 (s, 9H), 1.42 (s, 6H), 1.32 (s, 3H); HRMS (FAB): m/z (C$_{19}$H$_{29}$N$_2$O$_2^+$) calculated: 317.4458, found: 317.4410.

3.5.1.4. Synthesis symmetrical squaraine dye SQ
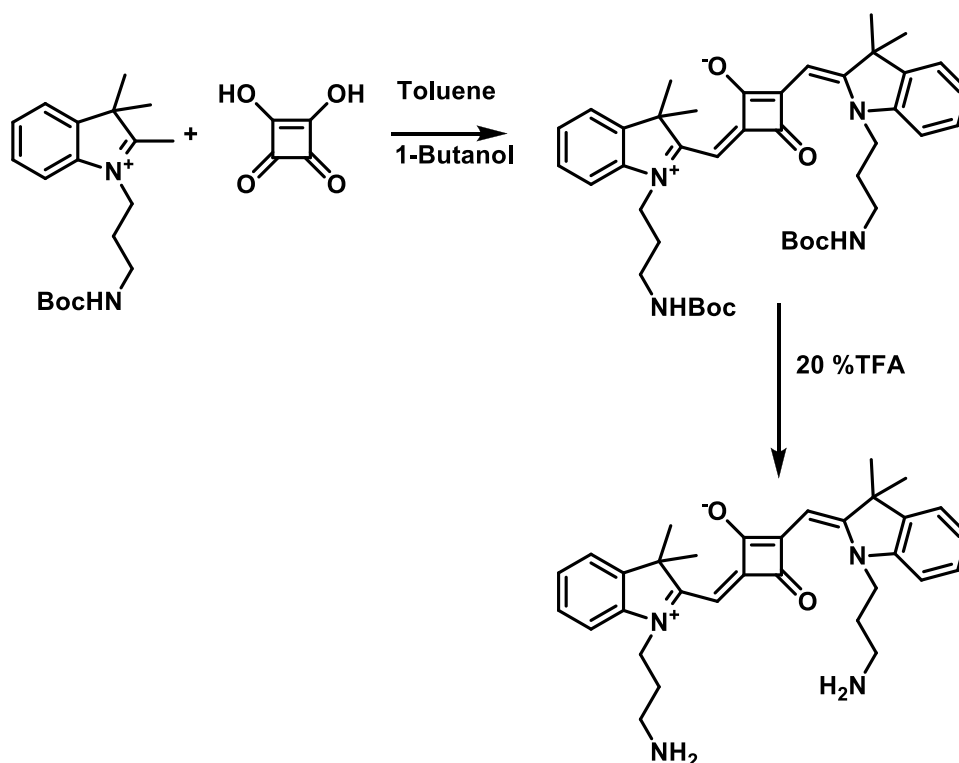
1-(3-(tert-butoxycarbonylamino)propyl)-2,3,3-trimethyl-3H-indolium (250 mg, 0.99 mmol) was added to a solution of squaric acid (56 mg, 0.49 mmol) in a mixture of dry n-butanol (6 mL) and dry toluene (4 mL) in an round bottom flask equipped with a Dean Stark apparatus.[1] Reaction mixture was refluxed for 12 h under N$_2$ atmosphere. A deep green coloured reaction mixture was concentrated and the crude product was purified by column chromatography using silica gel. Elution of the column with a mixture of DCM / methanol (1:9) afforded the desired squaraine dyes as green solid (yield = 49 %). ^{1}H NMR (500 MHz; CDCl$_3$): δ 7.35 7.26 (m, 2H), 7.15 (t, 1H, J = 7.25 Hz), 7.01 (d, 1H, J = 8 Hz), 5.94 (s, 1H), 3.27 (d, 2H, J = 5.5 Hz), 2.03 (m, 2H), 1.76 (s, 6H), 1.44 (s, 9H), ^{13}CNMR (125 MHz, CDCl$_3$): δ 206.97, 156.13, 142.36, 127.89, 123.86, 122.27, 109.41, 79.26, 50.34, 49.30, 38.18, 30.86, 28.33, 27.00, 24.56; HRMS (FAB): m/z (C$_{42}$H$_{54}$N$_4$O$_6$) calculated: 710.9014 found: 711. 9031 [M + 1]. Deprotection of Boc was carried out by treating the squaraine dye intermediate with 10% TFA in DCM (2 mL) for 3 h.

3.5.1.5. Synthesis of Matrix metalloproteinases (MMP 2) peptide sequence (PLGLAGS)
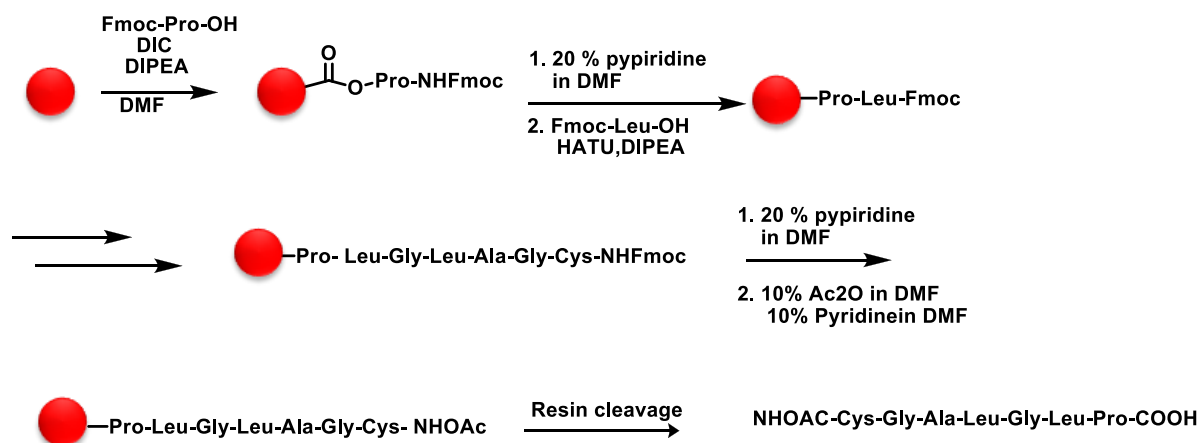
Preparation of PLGLAGS was initiated with Fmoc- Pro-OH (383 mg, 1.13 mmol) which was taken in dry dichloromethane (10mL) and DIC (0.218 mL, 0.071 mmol) was added. This was stirred at 0-5 ^{0}C for 1 h under N$_2$ atmosphere. The Fmoc- Pro-OH activated DIC complex was concentrated and then dissolved in DMF along with 2-3 drops of DIPEA and charged into the resin bed of HMPB-MBHA resin (200 mg, 0.0142 mmol) which was swelled up in dry dichloromethane (6 mL) for 30 min. The reaction was continued for 8 h with shaking. The progress of the reaction was monitored by the Kaiser test. After completion of the coupling, the resin was washed with DMF (3 x 3 mL), and the Fmoc protection group was removed by treatment with piperidine in DMF (20%, 3 x 2 mL, 3 x 15 min). The reaction cycle was continued in a similar manner with Fmoc- Leu-OH (150 mg, 0.426 mmol), Fmoc-Gly-OH (0.16 mg, 0.426 mmol), Fmoc-Leu-OH (150 mg, 0.426 mmol), Fmoc-Ala-OH(132 mg, 0.426), Fmoc-Gly-OH (0.16 mg, 0.426 mmol) and Fmoc-Cys-OH (585 mg, 0.426 mmol) amino acids charged to the resin. The resulting resin-bound peptide

was washed with DMF (3 x 5 mL), dichloromethane (7 x 3 mL) and methanol (3 x 3 mL), dried in vacuum (10 h), re-swelled in dichloromethane (5 mL), and filtered. Finally desired peptide sequence was released from the resin by treatment with 2% trifluoroacetic acid in dichloromethane (10 x 2 mL). The resin washing was combined and concentrated under reduced pressure, and the residue co-evaporated with toluene. The residue was precipitated with cold ether (3 mL) and filtered the residue peptide that afforded of white solid (yield: 89%). ^{1}H-NMR (500MHz, CDCl$_3$) : δ 8.90 (d, 1H), 7.99 (s, 5H), 7.43-7.40 (m, 6H), 7.38-7.23 (m, 9H), 4.49-4.50 (m, 1H), 4.29-4.27 (m, 2H), 4.12- 4.11 (m,1H), 3.91 (s, 2H), 3.74-3.71 (m, 1H), 2.66-2.65 (m,1H), 2.60-2.57 (m,1H), 1.97 (s, 3H), 1.70-1.67 (m, 2H), 1.39-1.28 (m, 2H), 0.94-0.90 (m,7H).

3.5.1.6. Synthesis of squaraine dye (SQ) conjugated MMP substrate (MMP-SQ)
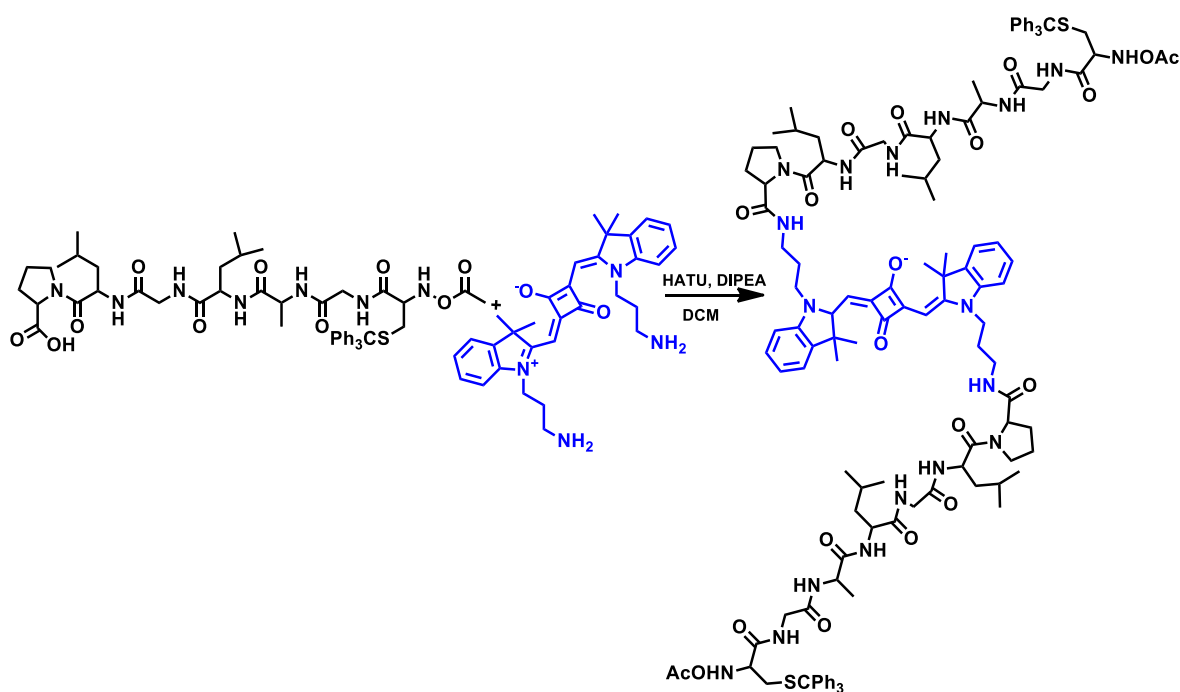
Squaraine dye (15 mg, 0.029 mmol) MMP substrate (54 mg, 0.058 mmol) were added to dry dichloromethane. Solution was stirred over night after adding HATU (22 mg, 0.058 mmol) DIPEA (4.5 mg, .035mmol) at room temperature to yield SQ-MMP as sticky blue solid (Yield=63%). ^{1}H-NMR (500MHz, CDCl$_3$) : δ 8.86 (s, 1H), 8.01-7.90 (m, 10 H), 7.42-7.36 (m, 18H), 7.30-7.27 (m, 1H), 7.22-7.20 (m, 1H), 7.14-7.11 (m, 2H), 5.84 (s, 1H), 4.20 (s, 2H), 4.16 (s, 2H), 3.65-3.59 (m, 2H), 3.01 (s, 3H), 2.10-2.07 (m, 2H), 1.67 (s, 6H).

3.5.1.7. Synthesis of MMP-SQ substrate conjugated gold nanorod, MMP-SQ@GNR

Squaraine dye, SQ was conjugated to MMP substrate by amide coupling. GNR was functionalized with MMP-SQ by simple mixing method. First, CTAB stabilized GNR was centrifuged (9000 rpm, 12 min) and washed twice with double distilled water. MMP-SQ (30 μM) solution was added in GNR colloid and it was kept in the absence of light at 25 ^{0}C under stirring for 24 h. The solution was purified by repeated centrifugation (9000 rpm, 30 min). To calculate the amounts of MMP-SQ attached per GNR, the absorption spectrum of the supernatant was measured using a UV-Vis spectrophotometer. The CTAB-coated GNR has molar absorption coefficients of 1.3 x 10^9 and 4.6 x 10^9 M^{-1} cm^{-1} at 510 and 785 nm, respectively. Molar absorption coefficient of MMP-SQ is calculated to be 1.5 x 10^5M^{-1} cm^{-1} at 620 nm. These values were used to calculate the average number of MMP-SQ bound per GNR in MMP-SQ@GNR.

3.5.1.8. Synthesis of Lipoic acid attached hydrazone linked doxorubicin
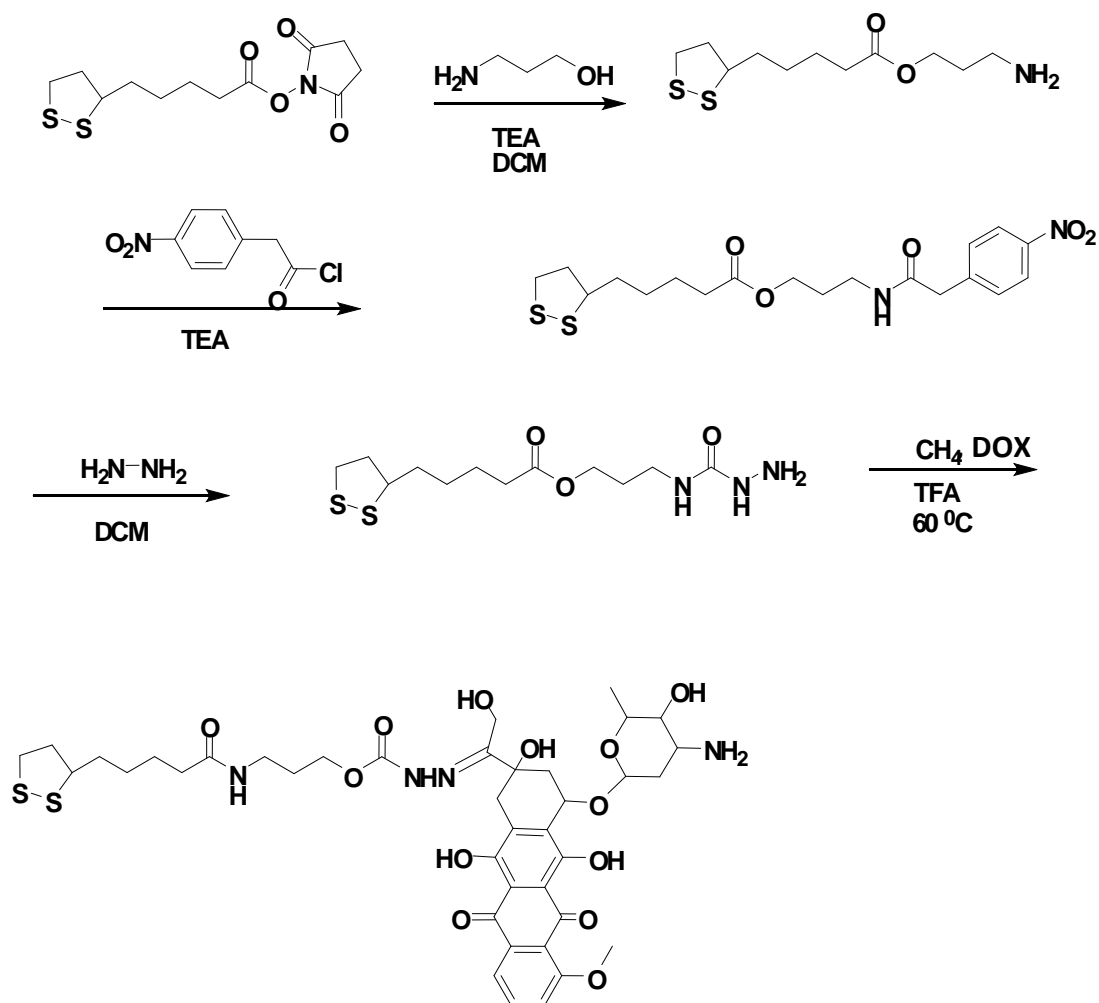
Scheme 3.3: Synthetic route towards LAH-DOX

3.5.1.9. Synthesis of lipoic acid succinimidyl ester
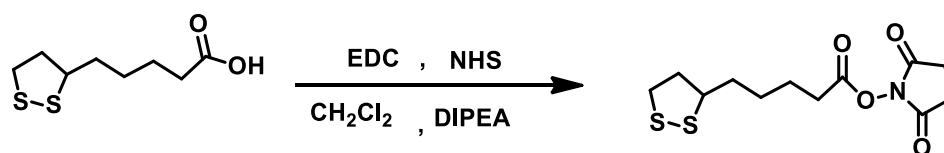
To a solution of EDC.HCl (1.1 g, 0.005 mmol) in dichloromethane, Diisopropyl ethylamine (0.750 g, 0.005 mmol) was added and stirred for 10 min. N-Hydroxysuccinimide (0.78 g, 0.006 mmol) was added followed by DL-Lipoic acid

(1g, 0.004 mmol). The reaction mixture was stirred in an ice bath for half an hour and then slowly continued in room temperature for overnight. The reaction mixture was washed with dilute HCl (5% 50 mL x 2) and water. The organic layer was dried over Na_2SO_4, filtered and concentrated. The crude residue was purified by silica gel column using ethyl acetate and hexane (yield 63%). ^{1}H NMR (500 MHz, CDCl$_3$) δ 3.557-3.612 (m, 2H), 3.178-3.212 (m, 1H), 3.097-3.133 (m, 2H), 2.617-2.647 (m, 2H), 2.442-2.5.0 (m, 2H), 1.897-1.964 (m, 2H), 1.750-1.824 (m, 2H), 1.665-1.720 (m, 2H), 1.571-1.624 (m, 2H).

3.5.1.10. Synthesis of LA-Pr-NPC
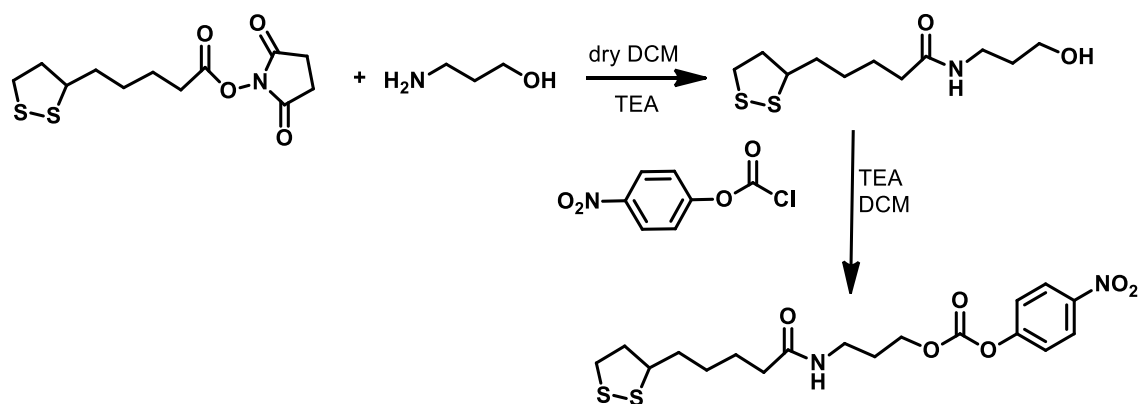
1-amino 3-propanol (10 µL, 0.141 mmol) was dissolved in dry DCM 0.2 mL of TEA was added to it. Lipoic acid succinimidyl ester (150 mg, 0.05 mmol) was added after 10min of stirring. Product obtained as white solid after overnight stirring. It was concentrated and precipitated in diethyl ether twice to produce LA-Pr-OH with a yield of 61%. ^{1}H-NMR (500MHz, CDCl$_3$): δ 5.91(s, 1H), 3.63 (t, 2H, *J* = 5 Hz), 3.44-3.40 (m, 2H), 2.49-2.43 (m, 3H), 1.93-1.89 (m, 2H), 1.69-1.67 (m, 8H), 1.43-

1.44 (m, 2H). The hydroxyl group of LA-Pr-OH was activated by p-nitrophenyl chloroformate. LA-Pr-OH (0.4 g, 0.115 mmol) and triethylamine (27 mg, 0.267 mmol) were dissolved in 20 mL anhydrous dichloromethane and stirred at 0 ^{0}C. To this solution was added drop wise p-nitrophenyl chloroformate (71 mg, 0.352 mmol) in 10 mL dichloromethane. The reaction was further performed at 0 ^{0}C for 1 h and at room temperature for 24 h under N_2 atmosphere. The resultant solution was diluted by dichloromethane and washed with brine solution for three times. The organic phase was collected, dried with anhydrous sodium sulphate, concentrated and precipitated into diethyl ether to give LA-Pr-NPC with a yield of 74%.^{1}H-NMR (500MHz, CDCl$_3$) : δ 8.15 (d, 2H, *J*=5Hz), 6.92(d, 2H, *J*= 5Hz), 3.59-3.54(m,2H), 3.45-3.41(m, 2H), 2.48-2.43(m, 2H), 2.24-2.20 (m, 2H), 1.93-1.88(m, 2H), 1.70-1.67(m, 8H), 1.49-1.44(m, 2H).

3.5.1.11. Synthesis of LA-Pr-Hyd
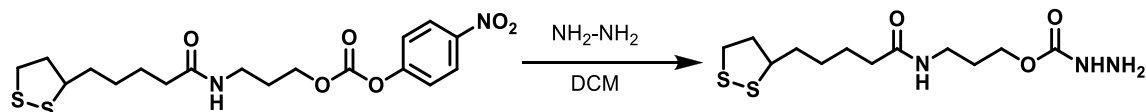
LA-Pr-NPC (30 mg, 0.07 mmol) was dissolved in 20 mL dichloromethane and reacted with hydrazine monohydrate (0.93 mmol). The solution was reacted for 24 h at room temperature. The resultant solution was washed with brine solution. The organic phase was collected and dried under vacuum after removing the solvent with a yield of 68%. ^{1}H-NMR (500 MHz, CDCl$_3$): δ 6.20 (s, 1H), 3.72-3.70 (m, 2H), 3.18-3.08 (m,2H), 2.48-2.42 (m, 3H), 2.28-2.24 (m, 2H), 1.92-1.86 (m, 2H),1.72-1.66 (m,

8H),1.49-1.44 (m, 2H). ESIMS: m/Z ($C_{12}H_{23}N_3O_3S_2$) calcd: 321.118, found: 344.1085 (M+Na).

3.5.1.12. Synthesis of LAH-DOX
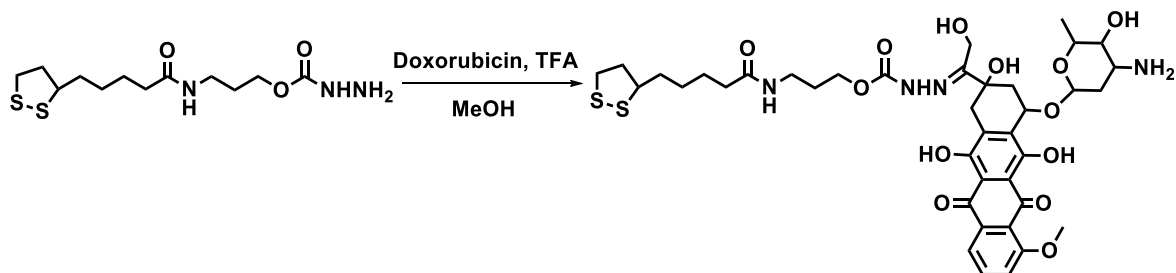
LA-Pr-Hyd (100 mg, 0.027 mmol) and doxorubicin (15 mg, 0.027 mmol) were dissolved in 25 mL anhydrous methanol. The mixture was reacted in the presence of a drop of trifluoroacetic acid at 60 ^{0}C overnight. After removal of methanol under vacuum purified through zeolite column. ESI-MS: m/Z ($C_{39}H_{50}N_4O_{13}S_2$) calcd: 846.2816, found: 845.6616(M-1).

3.5.1.13.   Preparation of DOX-Tethered GNRs

LAH-DOX (100 μM) was mixed with CTAB stabilized GNRs in 3 mL of ultra-purified water at pH 8.0. The mixture was stirred in the dark for 12 h at room temperature. Thereafter, the nanoparticles were centrifuged at a speed of 10000 rpm for 30 min to remove unconjugated LAH-DOX and washed once with Milli-Q water.

3.5.2.   Cell Culture.

The human cancer cell lines HTI080 (fibrosacroma), was obtained from American Type Culture Collection (ATCC, USA). The fibroblast-like murine preadipocyte cell line 3T3-L1 was generously provided by the Inter-University Centre for Genomics and Gene Technology, University of Kerala (Thiruvananthapuram, India).The cells

were maintained in DMEM media supplemented with 10% fetal bovine serum and antibiotics (100U mL^{-1} penicillin/100 µg mL^{-1} streptomycin mixture) in a 5% CO_2 incubator at 37 ^{0}C.

3.5.3. Cell viability assay.

HT1080 cells were seeded at a density of 10^4 cells/well in two 96 well plates and incubated at 37 ^{0}C for sufficient growth. Control, GNR, **MMP-SQ@GNR@LAH-DOX** were added to the wells separately in each plates. The treated cells were the incubated for 4 h. Then one of the plates were irradiated with 808 nm laser for 1 min. 100 µL MTT (0.5mg/mL) was added to each well and the purple color formation was measured calorimetrically at 570 nm

3.5.4. Live dead assay

100 µg/ mL Acridine orange (AO) and 100 µg/mL ethidium bromide (EB) were mixed in 1:1 ratio. 200 µL of the final mixture was added to 24 well plate. Fluorescence images were taken 2 min after Washing twice with PBS. Live cells were stained green and dead cells stained orange / red.

3.5.5. Annexin V assay

Additionally, evaluation of apoptosis by FITC Annexin V staining (FITC Annexin V apoptosis detection kit from BD Pharmingen #556547, BD Biosciences, San Jose, CA) was also confirmed by flow cytometry, using kit specified instructions. Signals were then detected using a FACS Calibur flow cytometer (BD Biosciences, San Jose, CA) and the data was analyzed with the Cell Quest Pro software.

3.5.6. DNA isolation before and after Photothermal chemotherapy

The DNA isolation kit for the study was bought from Geneaid. HT 1080 cells were grown in 6 well plates. Control, GNR, GNR DOX and **MMP-SQ@GNR@LAH-DOX** were treated in triplicate wells. HT1080 cells with and without laser irradiation in 10% DMEM medium was scraped using cell scraper followed by centrifugation and resuspension of the cells in Lysis Buffer. It was then incubated at 60 ^{0}C for 10 min 5 µL of RNase A (10 mg/mL) was added. After several steps of centrifugation by addition of provided reagents, purified DNA was eluted out and quantified for further experiments. For confirming apoptotic cell death due to photothermal-chemotherapy by the nanoconstruct, agarose gel electrophoresis was carried out. Genomic DNA isolated from HT1080 cells with and without laser irradiation was run on 0.8% agarose gel at 80 V power for about 45 min. The gel was then examined in a gel documentation system for the visualization of bands.

3.5.7. SERS spectral analysis

Cells were cultured in 4 well chamber slide made of glass at a seeding density of 10^4 cells/mL. **MMP-SQ@GNR@LAH-DOX** was added to the wells separately including control (media alone) and was incubated at 37 ^{0}C for 4 h. Further the cells were irradiated with 808 nm laser (0.1 W/cm^2, 1 min) .These cells were investigated with the spectral Imaging Mode of the confocal Raman Microscope (alpha300R, WI-Tec Inc. Germany). A spectrum at every pixel was taken (Scan Range: 40 x 40 µM^2, 100 x 100 pixel, 10,000 spectra) using a 20 x Nikon objective. The sample was excited with a 10 mW power 633 nm frequency doubled Nd:YAG laser. Using the

integrated video camera, a suitable cell was focused and scanned with an integration time of 0.5 s.

3.6. References

(1)   Nair, L. V.; Nazeer, S. S.; Jayasree, R. S.; Ajayaghosh, A. *ACS Nano* **2015**, *9* (6), 5825.

(2)   Graham, L. J.; Shupe, M. P.; Schneble, E. J.; Flynt, F. L.; Clemenshaw, M. N.; Kirkpatrick, A. D.; Gallagher, C.; Nissan, A.; Henry, L.; Stojadinovic, A.; Peoples, G. E.; Shumway, N. M. *Journal of Cancer.* **2014**, *5*, 58.

(3)   Panikkanvalappil, S. R.; Hira, S. M.; Mahmoud, M. A.; El-Sayed, M. A. *J. Am. Chem. Soc.* **2014**, *136* (45), 15961.

(4)   Kneipp, J. In *Surface-Enhanced Raman Scattering*; Kneipp, K., Moskovits, M., Kneipp, H., Eds.; Springer Berlin Heidelberg, 2006; Vol. 103, pp 335–349.

(5)   Cho, H.; Lee, B.; Liu, G. L.; Agarwal, A.; Lee, L. P. *Lab Chip* **2009**, *9* (23), 3360.

(6)   Panikkanvalappil, S. R.; Hira, S. M.; El-Sayed, M. A. *Chem. Sci.* **2016**, *7* (2), 1133.

(7)   Gao, Y.; Li, Y.; Wang, Y.; Chen, Y.; Gu, J.; Zhao, W.; Ding, J.; Shi, J. *Small* **2015**, *11* (1), 77.

(8)   Orendorff, C. J.; Gearheart, L.; Jana, N. R.; Murphy, C. J. *Phys. Chem. Chem. Phys.* **2006**, *8* (1), 165.

(9)   Cobley, C. M.; Au, L.; Chen, J.; Xia, Y. *Expert Opin. Drug Deliv.* **2010**, *7* (5), 577.

(10) Chen, J.; Glaus, C.; Laforest, R.; Zhang, Q.; Yang, M.; Gidding, M.; Welch, M. J.; Xia, Y. *Small* **2010**, *6* (7), 811.

(11) Lu, W.; Singh, A. K.; Khan, S. A.; Senapati, D.; Yu, H.; Ray, P. C. *J. Am. Chem. Soc.* **2010**, *132* (51), 18103.

(12) Choi, W. Il; Kim, J. Y.; Kang, C.; Byeon, C. C.; Kim, Y. H.; Tae, G. *ACS Nano* **2011**, *5* (3), 1995.

(13) Webb, J. A.; Bardhan, R. *Nanoscale* **2014**, *6* (5), 2502.

(14) Ali, M. R. K.; Wu, Y.; Han, T.; Zang, X.; Xiao, H.; Tang, Y.; Wu, R.; Fernández, F. M.; El-Sayed, M. A. *J. Am. Chem. Soc.* **2016**, *138* (47), 15434.

(15) Jain, S.; Hirst, D. G.; O'Sullivan, J. M. *Br. J. Radiol.* **2012**, *85* (1010), 101.

(16) He, C.; Liu, D.; Lin, W. *ACS Nano* **2015**, *9* (1), 991.

(17) Chen, Y.-W.; Chen, P.-J.; Hu, S.-H.; Chen, I. W.; Chen, S.-Y. *Adv. Funct. Mater.* **2014**, *24* (4), 451.

(18) Zheng, M.; Yue, C.; Ma, Y.; Gong, P.; Zhao, P.; Zheng, C.; Sheng, Z.; Zhang, P.; Wang, Z.; Cai, L. *ACS Nano* **2013**, *7* (3), 2056.

(19) Yuan, Y.; Wang, Z.; Cai, P.; Liu, J.; Liao, L.-D.; Hong, M.; Chen, X.; Thakor, N.; Liu, B. *Nanoscale* **2015**, *7* (7), 3067.

(20) Chen, R.; Zheng, X.; Qian, H.; Wang, X.; Wang, J.; Jiang, X. *Biomater. Sci.* **2013**, *1* (3), 285.

(21) Peng, J.; Qi, T.; Liao, J.; Chu, B.; Yang, Q.; Qu, Y.; Li, W.; Li, H.; Luo, F.; Qian, Z. *Theranostics* **2014**, *4* (7), 678.

(22) Feng, L.; Li, K.; Shi, X.; Gao, M.; Liu, J.; Liu, Z. *Adv. Healthc. Mater.* **2014**, *3*

(8), 1261.

(23) Yi, D. K.; Sun, I.-C.; Ryu, J. H.; Koo, H.; Park, C. W.; Youn, I.-C.; Choi, K.; Kwon, I. C.; Kim, K.; Ahn, C.-H. *Bioconjug. Chem.* **2010**, *21* (12), 2173.

(24) Lee, S.; Cha, E.-J.; Park, K.; Lee, S.-Y.; Hong, J.-K.; Sun, I.-C.; Kim, S. Y.; Choi, K.; Kwon, I. C.; Kim, K.; Ahn, C.-H. *Angew. Chemie* **2008**, *120* (15), 2846.

(25) Gong, T.; Kong, K. V.; Goh, D.; Olivo, M.; Yong, K.-T. *Biomed. Opt. Express* **2015**, *6* (6), 2076.

(26) Narayanan, N.; Karunakaran, V.; Paul, W.; Venugopal, K.; Sujathan, K.; Kumar Maiti, K. *Biosens. Bioelectron.* **2015**, *70*, 145.

(27) Ramya, A. N.; Samanta, A.; Nisha, N.; Chang, Y.-T.; Maiti, K. K. *Nanomedicine* **2015**, *10* (4), 561.

(28) Maniganda, S.; Sankar, V.; Nair, J. B.; Raghu, K. G.; Maiti, K. K. *Org. Biomol. Chem.* **2014**, 6564.

(29) Wang, F.; Wang, Y.-C.; Dou, S.; Xiong, M.-H.; Sun, T.-M.; Wang, J. *ACS Nano* **2011**, *5* (5), 3679.

(30) Verrier, S.; Notingher, I.; Polak, J. M.; Hench, L. L. *Biopolymers* **2004**, *74* (1–2), 157.

(31) Kang, B.; Austin, L. A.; El-Sayed, M. A. *ACS Nano* **2014**, *8* (5), 4883.

Exploration of Targeted Theranostic Nanoprobe built on SERS and Fluorescence Dual Imaging Modality Towards Enhanced Phototherapy on Breast Tumor Cells
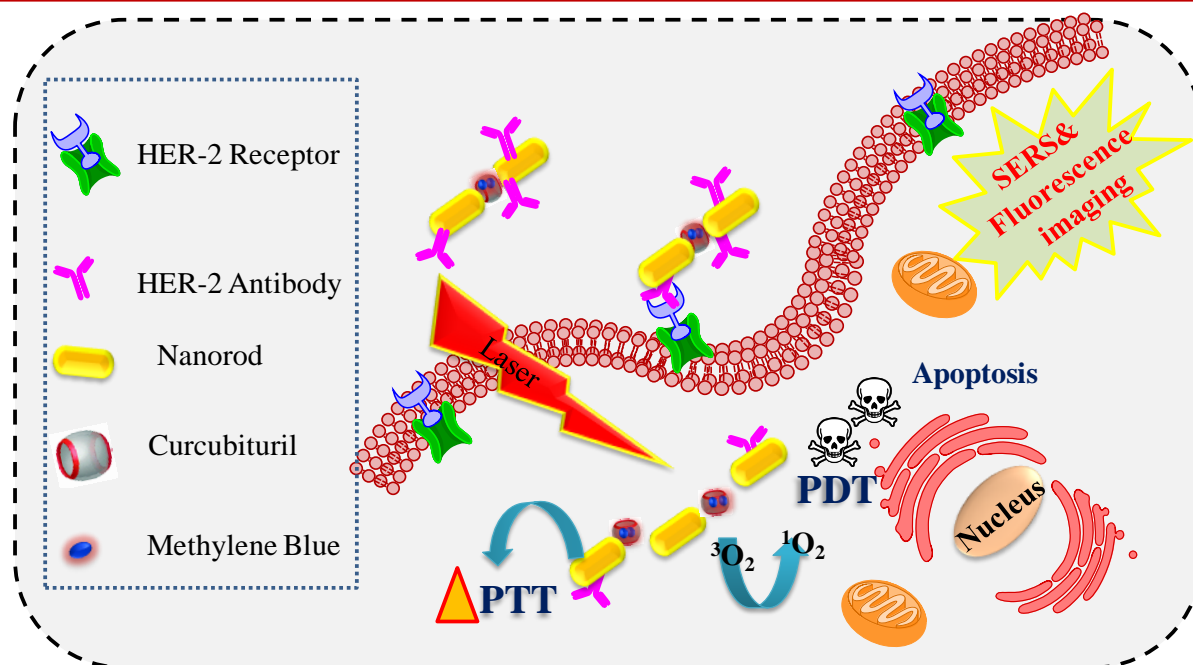
4.1. Abstract

Recent progress in nano theranostics promotes to integrate different treatment strategies in a single platform to improve the therapeutic efficiency because of the synergistic effects. Photodynamic therapy (PDT) is one of the most promising approaches for cancer management and it is minimally invasive. In PDT photosensitizers (PSs) are excited by light of suitable wavelength and react with molecular oxygen to generate reactive oxygen species (ROS), which in turn destructs

tumor cells and tissues in situ. Conventional PSs endure low solubility in the physiological media, non specificity, poor photostability and high photobleachability. Therefore it is crucial to administer high doses of PSs for effective treatment. Also, the light sensitivity of the presently used PSs restricts the patients from entering the day light. The high reactivity and specificity presented by the nanoparticles can be utilised to tune them to overcome these limitations to a great extent. In recent years, photothermal therapy (PTT) has also been explored as another noninvasive effective treatment for malignant carcinomas. Following NIR laser irradiation, photoabsorbing agents could transduce electromagnetic energy into localized heat and consequently destroy tumor cells and tissues. Gold nanomaterials such as nanorod, nanocage, nanostar, nanoshell etc. have attracted much attention as photothermal transducers. The combination of PDT with PTT can enhance the therapeutic index through synergistic effect. Gold nanorod based theranostic platform integrating PTT and PDT could be an ideal choice for cancer management. Methylene blue-loaded cucurbituril [8] @ gold nanorod conjugated with HER2 antibody, MB-CB [8] @ GNR-Her2 was constructed for SERS and fluorescence imaging modality in combination with PTT and PDT dual therapy. The nanocarrier envisages high surface plasmon resonance and intense fluorescence enabling it as a promising SERS nanotag as well as fluorescence imaging probe. The superior HER2-targeted cytotoxicity of the nanoconstruct was evaluated by apoptosis assays like acridine orange-ethidium bromide, and colorimetric quantification using APOPercentage™ Apoptosis assay. The cytotoxic studies unravelled the superior therapeutic potential of targeted theranostic nanoprobe upon

single 808 nm laser irradiation through the induction of apoptosis. Although auxiliary investigations are warranted with this promising nanoconstruct, superior cytotoxic effect under single laser irradiation along with dual imaging capability emphasizes its further exploration in oncology.

4.2. Introduction

Breast cancer is one of the prevalent and commonly diagnosed cancers among women worldwide. Various approaches such as Magnetic resonance imaging (MRI), ultrasound, biopsy etc. are routinely used to detect this deadly disease in order to find out effective strategies for better treatment. Last several decades have witnessed great advancement in cancer imaging and therapy.[1] Photodynamic therapy (PDT) is gaining progressive recognition because it can be useful for treating solid tumors that are not accessible to surgery, radiation and chemotherapy.[2,3] Further PDT has low systemic toxicity, lower toxic side effects than those induced by radiotherapy and chemotherapy. PDT can be affected locally onto a specific region by selectively illuminating the tumor area only by light, while leaving normal tissues unharmed. The fundamental principle of PDT engrosses the production of highly toxic reactive oxygen species upon excitation of a sensitizer with harmless visible light of defined wavelength.[4] Two key reaction pathways, path I and path II, are involved in the PDT action. The first pathway, termed the type I mechanism, involves the generation of radical species through either hydrogen abstraction or redox processes between a sensitizer in an excited state and the biomolecule.[5] In the type II mechanism, the

sensitizer in the triplet excited state generates singlet oxygen ($^1O_2$) from ground-state molecular oxygen ($^3O_2$) through an energy transfer process (**Figure 4.1**).[6]
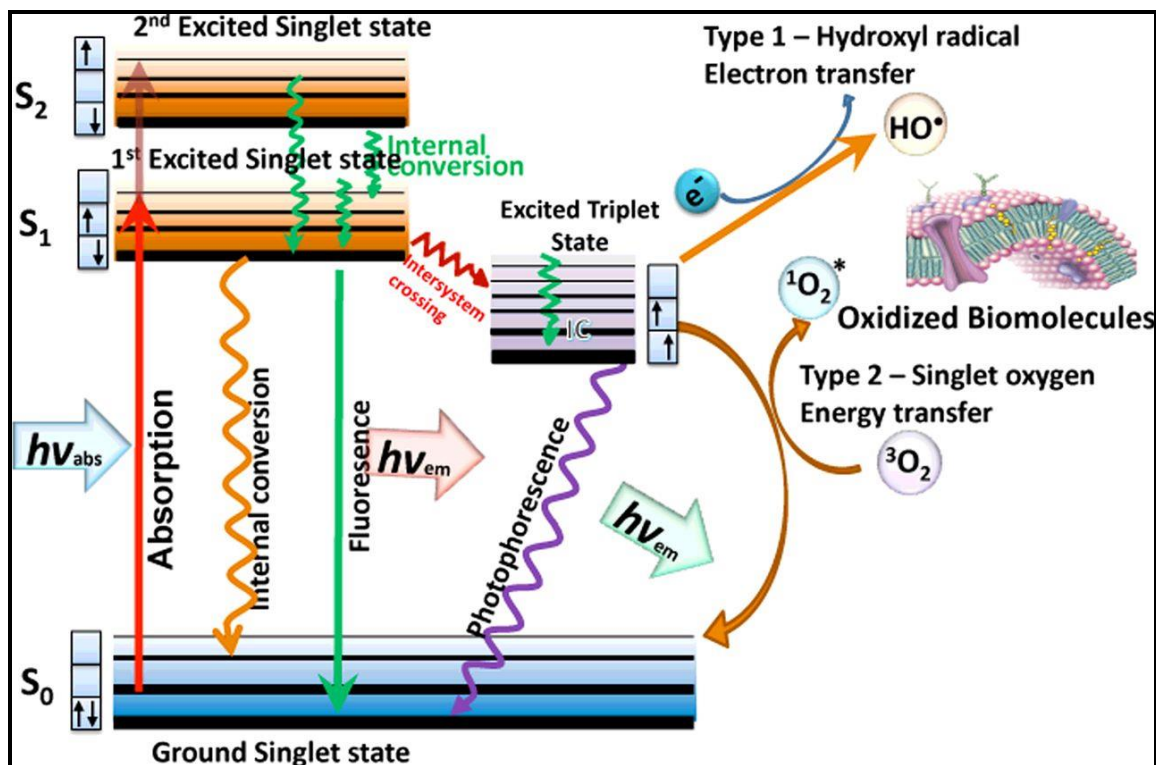
Figure 4. 1. Schematic representation of two pathways involved in photodynamic therapy.

A typical photosensitizer (PS) should have very good photostability, minimum dark toxicity, high absorption in the red or near infrared region of the spectrum, reasonable hydrophilicity, target specificity, and quick clearance from the body etc. Different kinds of PSs have been developed and their therapeutic efficiency has been investigated. Porphyrins, chlorins, benzoporphyrins, benzoporphycenes, phthalocyanins, purpurins, and aminolevulinic-acid mediated porphyrins etc. are excellent PSs with high therapeutic potential(**Figure 4.2**).[7,8] Methylene blue (MB) is a well known PS[9,10] because of its high photo-stability, easy elimination from the

body, minimum toxicity and MB has exhibited phototoxicity towards a variety of cancer cell lines *in vitro*.[11,12]
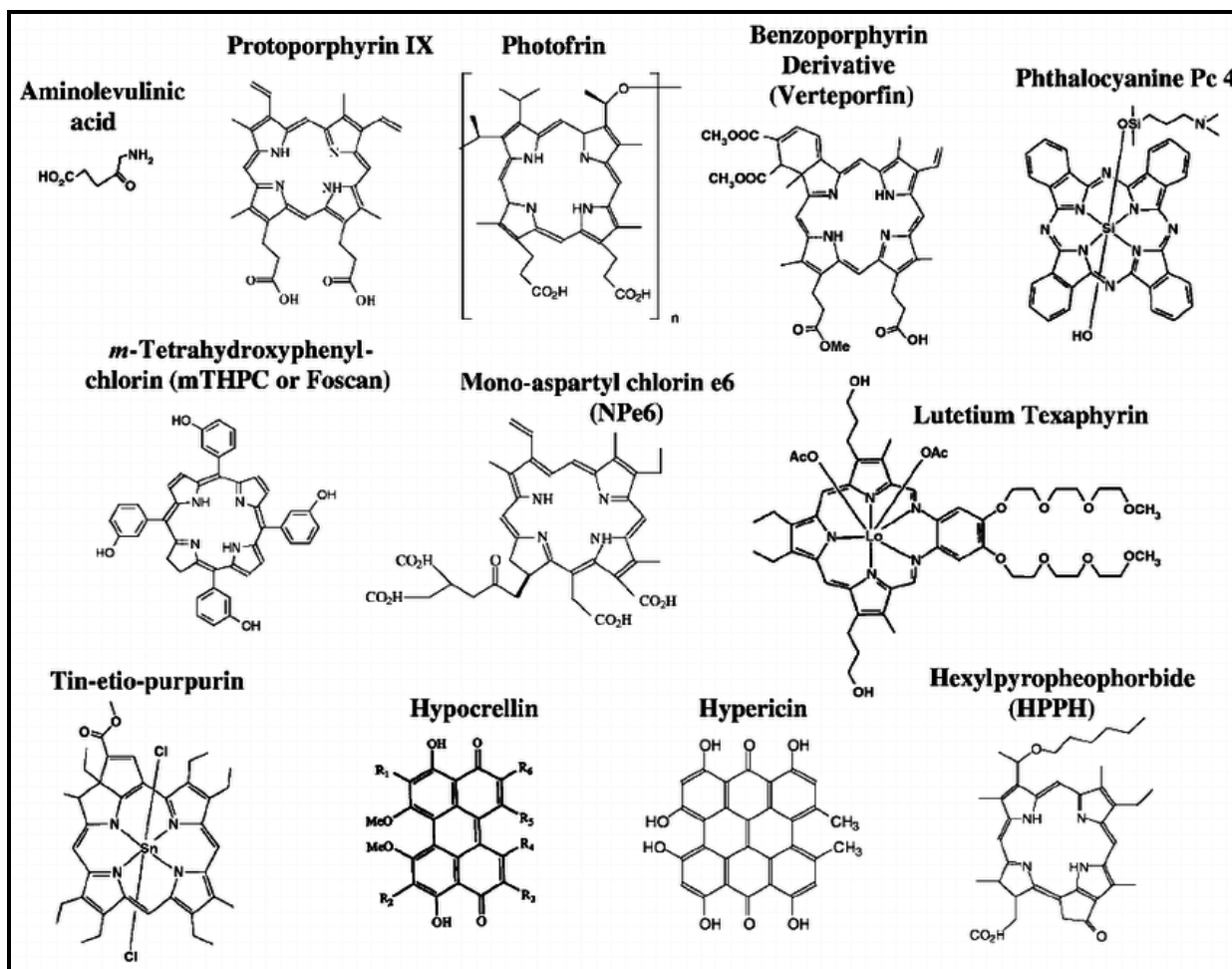
Figure 4.2.Structures of some of the selected PSs in clinical or pre-clinical studies.

However, clinical use of MB has been restricted because it has several drawbacks[13] such as its poor tumor localization, and prolonged cutaneous photosensitivity. Further MB is converted to its leuko- (colorless) isomer, a non-photosensitizer with negligible photodynamic activity in the biological environment. In order to overcome these limitations, various strategies have been applied to improve the therapeutic

potential of MB. These strategies include the delivery of MB using nano-sized carriers such as liposomes, polymer micelles, and organic/inorganic NPs etc. The conventional delivery systems suffer from drawbacks such as the post treatment accumulation of the free PS in the skin and the eyes. So the development of a highly potent nanocarrier for targeted therapy is very essential to improve the therapeutic potential of PDT. An intelligent strategy of host-guest complexation of MB inside cucurbit [7]uril, CB[7] was adopted by Scaiano and co-workers. The triplet excited state lifetime of MB was found to be increased in the CB [7] cavity. Further CB protects the dye triplets from quenching by oxygen. The $^1O_2$ quantum yield is similar for both MB and MB-CB [7]. Similarly complexation of MB inside CB [7] & CB [8] was investigated by Garcia and co-workers. CBs are water-soluble macrocyclic molecules made of glycoluril units connected by methylene bridges.[14] The photodynamic efficiency of MB protected inside CB cavity in cancer cells is yet to be explored. CBs are generally written as cucurbit[n]uril, where n represents the number of glycoluril units. The architecture of CBs are quite suitable to form strong inclusion complexes with positively charged organic molecules.[15] "Cucurbituril'' got its name because of its similarity to ''a gourd or pumpkin'' which belong to the *Cucurbitaceae* family. To date CB family is extended with members having upto 14 repeat units. The cavity size increases with increase in number of glycoluril units **(Figure 4.3)**
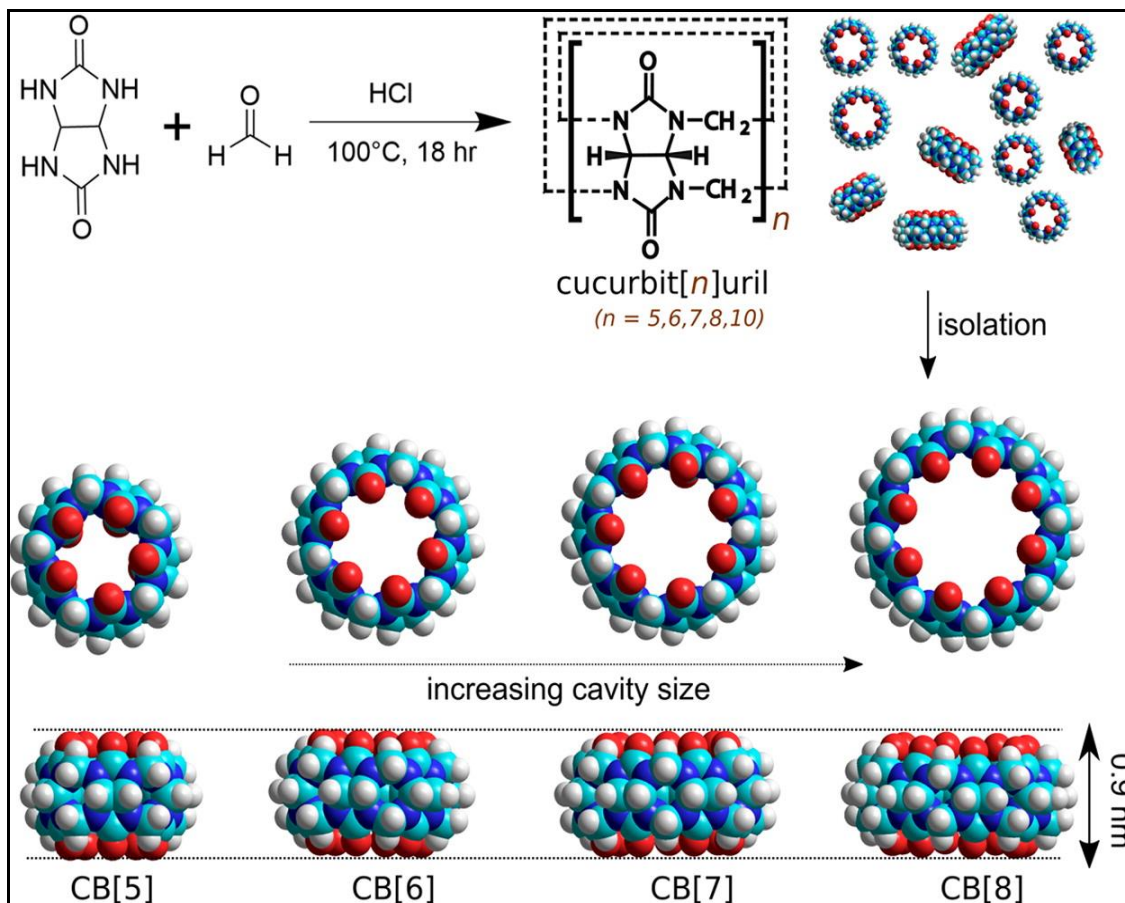
Figure 4.3. The reaction between glycoluril and formaldehyde (Top) Space-filling models of CB[5]–CB[8] demonstrating the increasing cavity size of the CB[n] macrocycles.

It is recently reported that CBs can act as a rigid spacer between nanoparticles maintaining desired distance between nanoparticles **(Figure 4.4)**.[16] CB [5] is a stiff barrel-shaped molecule which binds to the AuNP surface through the carbonyl groups at the portals and thus fixes the separation between AuNPs and act as glue between NPs. Besides, the molecule encapsulated inside CB cavity will be at the hotspot enabling finest SERS sensing.
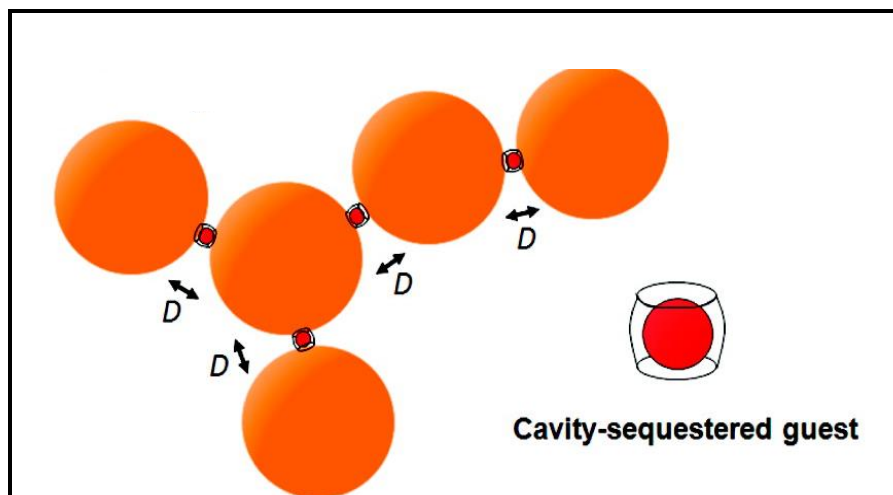
Figure 4.4: CB[n] cavity supports selective guest sequestration, leading to the use of AuNP: CB[n] aggregates for molecular-recognition-based SERS assays.

Alignment of GNRs end-to-end using CB[n] bridges and large SERS enhancement of rhodamine 6G signals was reported by Scherman and co- workers (**Figure 4.5**).[17] GNRs with an aspect ratio of 3.3 was synthesized with transverse and longitudinal modes at 510 nm and 712 nm respectively. Functionalisation at the curved end of GNRs is more easily compared to longitudinal facet this fact is exploited to align GNRs using CB[n]. CTAB layer was removed by continuous centrifugation and addition of 1:1 solution of H_2O: CB [5].

So based on the previous reports MB having positive charge and optimum size can be encapsulated inside CB cavity. In the present work CB [8] has been exploited as an effective carrier for MB at the same time, it aligns GNRs for generating precise sub nanometer plasmonic junctions serving as SERS hot spots. GNR plays key role as SERS substrate as well as photothermal transducer. PTT is another promising strategy for treatment of solid tumors in minimally invasive manner.[18]
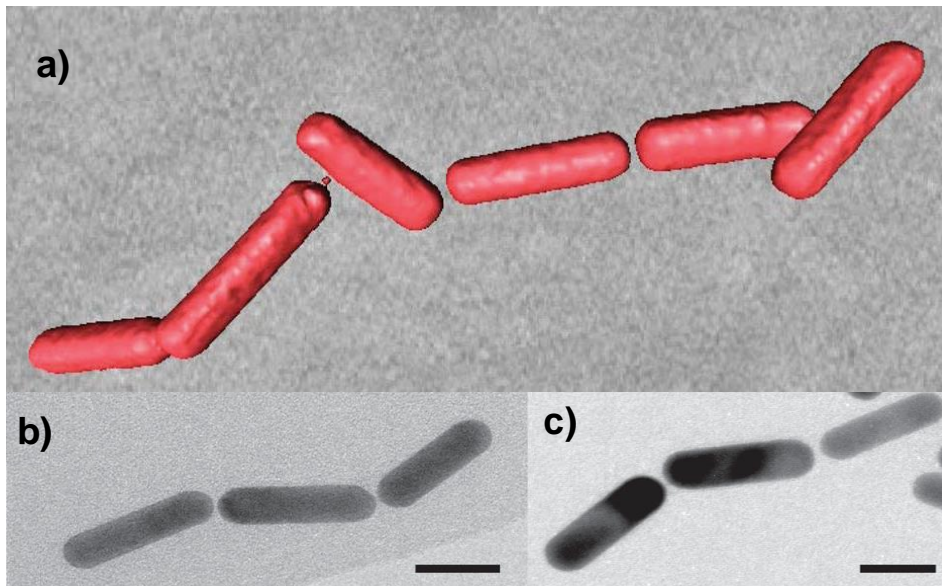
Figure 4.5 a) Computer-aided visualization of the cryo-electron tomogram obtained from the assembly of GNRs. b) & c) TEM images showing alignment of GNRs after washing with CB [5].

PTT involves the conversion of the absorbed NIR light into heat.[19] Developments in nanotheranostic allows the integration of PDT and PTT in a single platform to further enhance the phototherapeutic efficiency.[20–22] Generally individual nanoparticles are conjugated with PSs in order to produce combined PDT and PTT in a localized manner.[23,24] Synergistic PDT/PTT based on this method need two lasers in different wavelengths.[25] Therefore there is a great challenge to develop simple and effective strategy for simultaneous PDT/PTT exhibited in a single laser.[26,27] In the present study CB [8] with encapsulated MB acts as glue between GNRs which generate SERS hot spots and executes synergistic PDT and PTT in a targeted fashion along with fluorescence and SERS imaging. The combinations of targeted therapy by PDT, and PTT along with simultaneous fluorescence and SERS imaging will be an excellent

nanotheronstic towards the treatment of solid tumors.[28,29] Hence, the fabricated nano-construct exhibited the potential for pre-clinical and further clinical studies towards efficient cancer treatment.

4.3. RESULTS AND DISCUSSION

4.3.1. Methylene blue encapsulation in cucurbit[8]uril cavity

MB is a drug used in clinical applications for malaria as well as a recognized PS for local treatment of periodontal diseases. MB belongs to the phenothiazinium family having tricyclic structure. The positive charge as well as the amino substituent's at the 2 and 7 positions along with optimal molecular dimensions make it adequate to form stable complexes with CBs of the appropriate size. Complex formation is investigated in double distilled water with working dye concentration of 10^{-6} M. The formation of the MB-CB [8] complex was established through UV-Vis, Fluorescence, and ^{1}H-NMR spectroscopic analysis. The addition of CB [8] to the MB solution produces significant changes in the optical spectrum. When a small volume of a 10^{-4}M stock solution of CB[8] was added to 10^{-6} M solution (3 mL) of MB, the intensity of monomer absorption band centered at 664 nm gradually decreases whereas the intensity of dimer band with λ-max at 610 nm increases (**Figure 4.6a**). This indicates that the large cavity of CB [8] allows the inclusion of two dye molecules which is reflected by the reversal in monomer and dimer concentration of the solution. Complex formation between MB and CB [8] was also investigated by recording the dramatic variations in fluorescence spectra on addition of CB (10^{-4} M)

to MB solution. The dimeric character of the dye molecules when encapsulated inside CB [8] and the self quenching due to π-π interactions are responsible for the decrease in fluorescence intensity[30] (**Figure 4.6b**). The absorption and emission spectral changes indicates that MB dimer species are present inside CB [8] cavity.
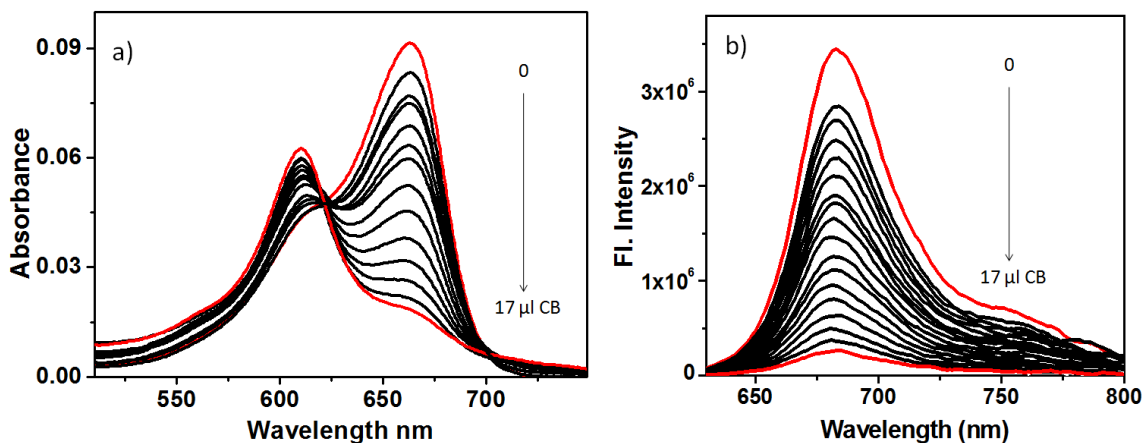
Figure 4.6. a) Absorption b) emission spectral changes of MB as a function of CB [8] concentration from 0 to 5×10^{-7}M

Encapsulation of MB inside CB was further analyzed by ^{1}H-NMR spectra. The chemical shifts, as well as the number of peaks are changed remarkably with respect to the ^{1}H-NMR spectra of MB alone. The duplication of most of the ^{1}H-NMR signals are observed which also accounts for the development of dimers of MB inside CB [8]. The dimers will overlap by two of the three aromatic rings thus disturbing the symmetry of the molecule (**Figure 4.7**), generating different signals for the overlapped and unoverlapped aromatic protons in ^{1}H-NMR spectra (**Figure 4.8).**

Figure 4.7 Chemical structure of MB and its dimer.
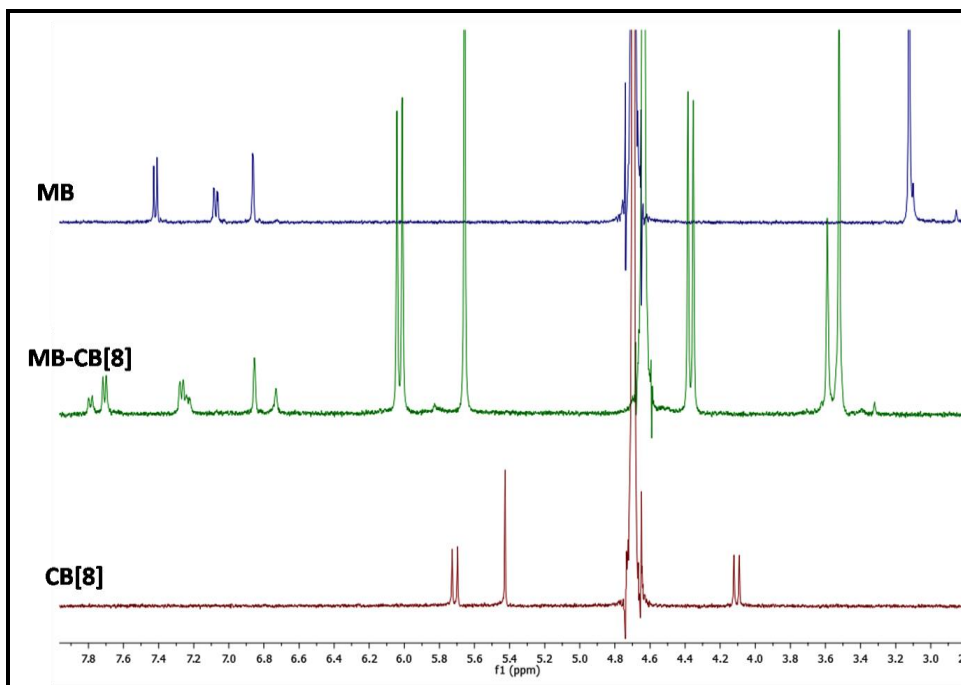
Figure 4.8. ^{1}H-NMR spectra recorded in D_2O for MB (blue), MB-CB [8] (green), CB [8] (brown).

The MB monomers and dimers have different photochemical reactions, the monomers usually undergo the type I photochemical mechanism, in which photo excited MB molecules in a singlet state endure int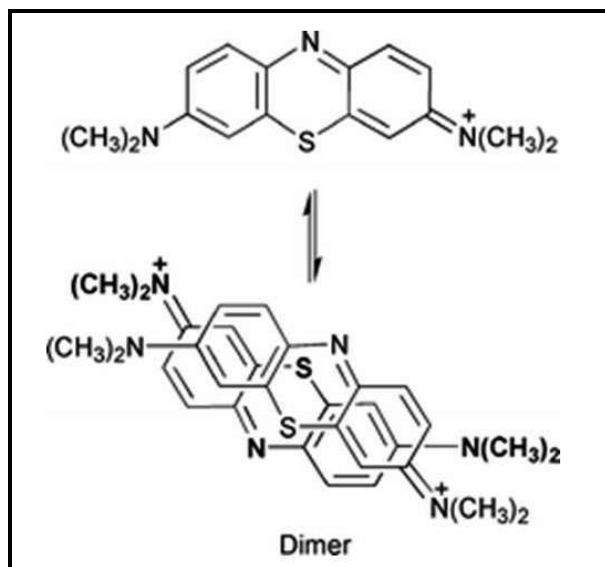ersystem crossing (ISC) to a metastable triplet state.[31] Then, singlet oxygen ($^1O_2$) is generated by the triplet MB molecules through energy transfer, as represented by reaction (2) in **Scheme 4.1**. Whereas MB dimers can produce MB free radicals through self-dissociation as shown in reaction (6) of **Scheme 4.1**. MB radicals react with oxygen to produce a superoxide. Further MB radicals produce various ROS species, including a highly reactive hydroxyl radical through a Fenton reaction. So MB dimers are more effective than monomers in eliminating hypoxic conditions which arises due to the imbalance between oxygen supply and consumption. Usually a high concentration of MB solution is essential to attain MB dimers.
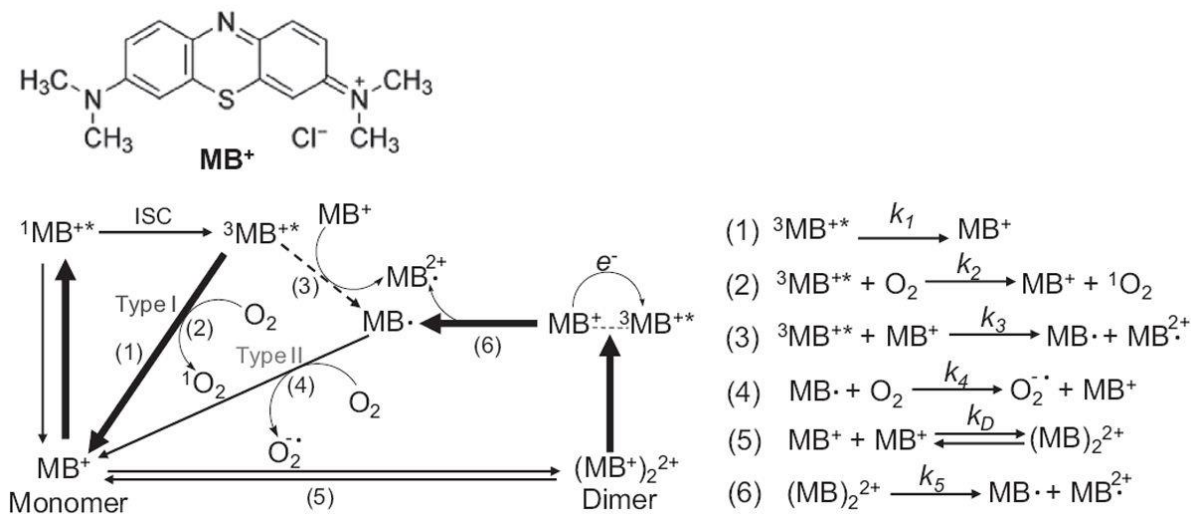
Scheme 4.1. Schematic illustration of photochemical reaction of MB, where MB^+ is the singlet ground state; $^3MB^+*$ the excited triplet state; ISC the intersystem crossing; MB• the semi-reduced radical; MB•$^{2+}$ the semi-oxidized radical.

But high concentration will induce chemical toxicity in normal cells. The encapsulation of MB inside CB cavity generates MB dimers thereby enhancing the photodynamic efficiency and overcomes the drawbacks in conventional MB treatment.
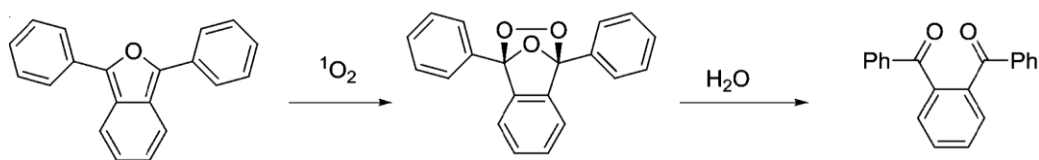
4.3.2. Singlet oxygen generation study

The PS gets excited when it is exposed to light of a specific wavelength, which in turn generates singlet oxygen through different pathways. The singlet oxygen generation ability can be measured by direct or indirect method. In the direct method for detecting singlet oxygen generation ability, PSs in appropriate solvent is irradiated with suitable radiation source in regular interval of time and subsequent emission spectra are recorded to measure the intensity of strong emission maxima around 1280 nm which is directly proportional to the concentration of singlet oxygen.

Indirect method is associated with the measurement of decreasing optical density value of the singlet oxygen scavenger such as diphenylbenzofuran (DPBF) by UV-Vis spectroscopy (**Scheme 4.2**). The PS, mixed with singlet oxygen scavenger upon laser irradiation produce singlet oxygen which is rapidly consumed by the scavenger. This reduces the optical density value of the scavenger molecule in the UV-Vis spectrum.

Scheme 4.2. Schematic illustration of the reactions between singlet oxygen and the scavenger DPBF.

In the present work, indirect method was adopted for determining singlet oxygen generation efficiency. MB solution was mixed with DPBF in a 3 mL cuvette and the UV-Vis spectra were recorded by irradiating it with radiation from an orial lamp (610 nm). Up on irradiation PS generated singlet oxygen which is rapidly consumed by DPBF molecule, this leads to the decrease in optical density value of DPBF (**Figure 4.9**).
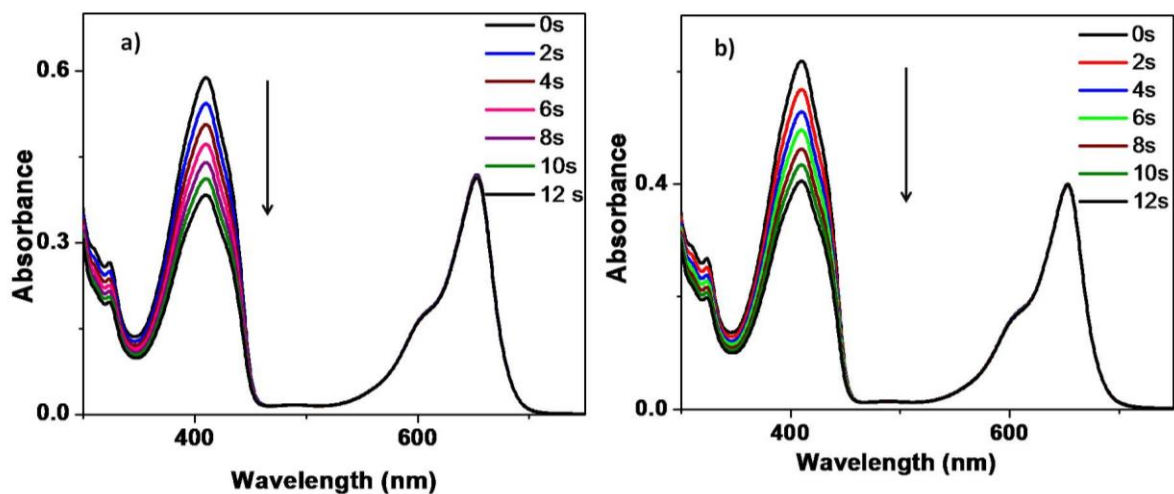

Figure 4.9: Time evolution of the UV-vis spectrum of a DPBF (25 µM) in methanol a) with MB b) with MB-CB [8] on irradiation with radiation from an orial lamp (610 nm).

4.3.3. Synthesis and characterization of Gold nanorod

After confirming the formation of MB dimers for enhanced PDT efficacy inside cucurbituril cavity through UV- Vis, fluorescence and ^{1}H-NMR spectral analysis, synthesis of GNR was initiated. CTAB stabilized GNRs having aspect ratio approximately 4 was synthesized according to the standard literature method.[32] The synthesized GNR has the zeta potential around +36. The strong LSPR of GNR was tuned to the NIR region by tuning the aspect ratio to minimize tissue absorption and maximize laser absorption of GNR.

4.3.4. Bioconjugation on GNRs: PEG encapsulation and antibody conjugation

Polyethylene glycol (SH-C$_2$H$_4$-CONHPEG-C$_3$H$_6$-COOH (MW: 3000 dalton) encapsulation of GNR was carried out before antibody conjugation on the GNR surface. The carboxy functionality was introduced by chemisorption with SH-PEG-COOH for bioconjugation with targeting monoclonal antibodies. The PEG encapsulation of the nanotheranostic probe was characterized by UV–Vis absorption spectra which showed a shift in absorption maxima around 2–3 nm **(Figure 4.10a)**. Next, monoclonal antibody specific to breast cancer over expressed protein HER/neu (Erb-B2) was covalently conjugated to carboxy functionalized PEG coated GNRs surface which followed the standard protocol[33]. HER2 is a recognized breast cancer marker which belongs to the group of membrane receptor tyrosine kinase that regulates cell cycle and its over-expression assists cancer progression. Successful anti-body conjugation was achieved by well established EDC-NHS coupling strategy

which was finally confirmed by UV–Vis spectroscopy and polyacrylamide gel electrophoresis (PAGE).[34] UV–Vis spectra of antibody conjugated GNRs showed a distinct protein absorption band nearly around 260 nm. HER2 conjugation was further confirmed by PAGE analysis, in which native PAGE after complete migration, proteins were silver stained and the size was compared with PAGE ruler plus pre-stained protein ladder10–250 kDa. HER2 antibody has size around 185 kDa. The antibody conjugated GNR showed the band nearly at 185 kDa which is correlated with the position of the pure antibody **(Figure 4.10b)**.

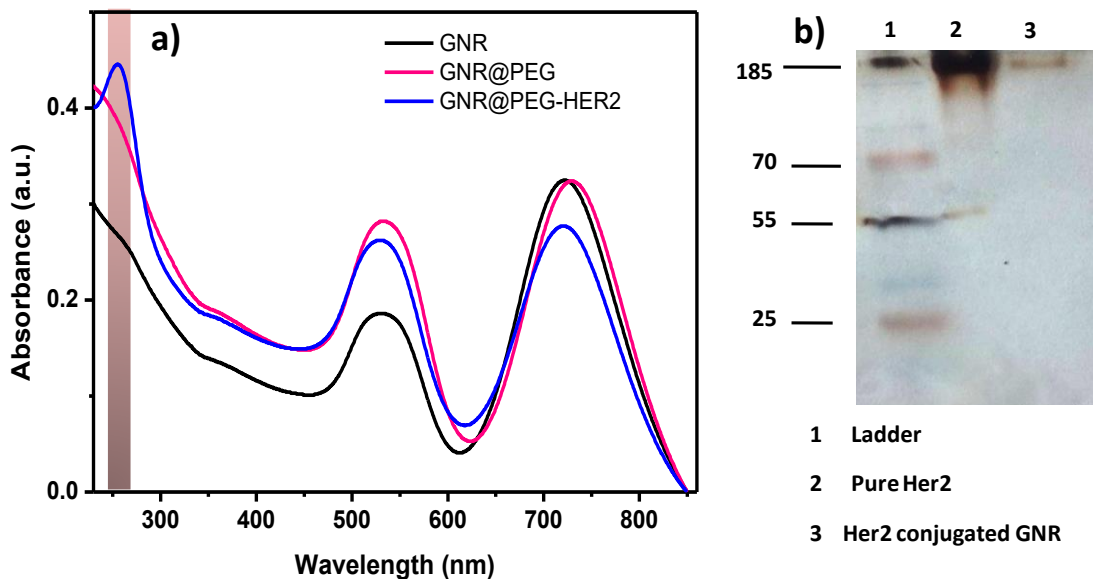**Figure 4.10 a)** Absorption spectra of GNR (black), PEG encapsulated GNR (red), antibody conjugated GNR (blue). **b)** PAGE of HER2 conjugated GNR.

4.3.5. Alignment of GNRs with CB [8]

Aligning GNR end-to-end will enhance its impact for SERS intensities where, gaps between GNRs can be controlled with sub nanometer precision to achieve reproducible hot spots.[35] It is recently reported that cucurbit[n]urils, can arrange

spherical AuNPs maintaining desired distance (~1 nm) between them by acting as a rigid spacer.[35,36] Scherman and co-workers extended the work by using cucurbituril to align GNRs in end to end fashion.[37] Functionalization and bioconjugation at the curved end of GNR is easy when compared to the longitudinal facet as CTAB can be easily removed from the curved ends. This insight is exploited to allow the alignment of PEG encapsulated GNRs using CB [8]. Colloidal solution of functionalized GNRs was centrifuged to remove excess CTAB followed by the addition of a 1:1 solution of H_2O: CB [8] (1 mM), this process was repeated twice. Upon addition of CB [8] after two wash cycles, alignment of GNR occurs in an end to-end manner. HR-TEM analysis showed the precise arrangement of PEG encapsulated GNRs by CB [8] compared to PEG encapsulated GNR without CB [8] alignment (**Figure 4.11a**) HR-TEM analysis exhibited short GNR chains with ~3 nm gap between them which accounts for the expected height of one CB molecule (~1 nm) along with PEG coating on two curved ends of GNR.(**Figure 4.11b**).
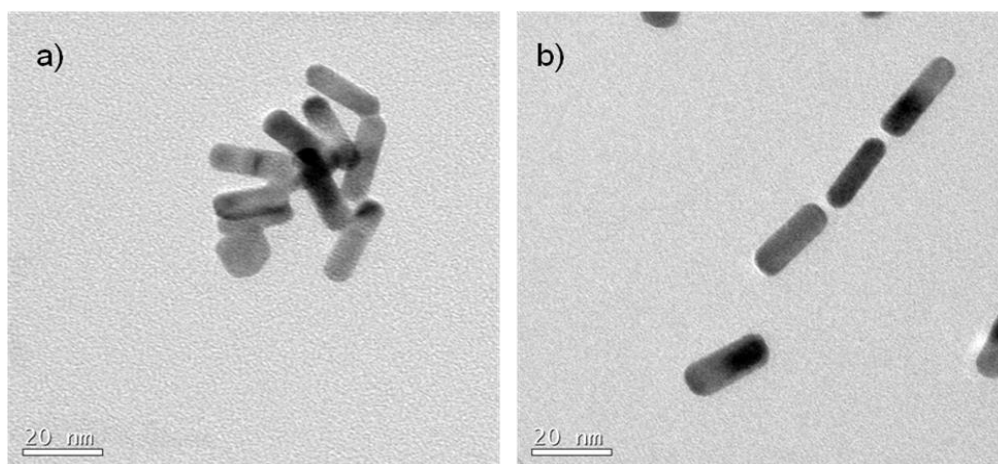

Figure 4.11. HR-TEM images of a) GNRs b) GNRs linearly aligned with CB [8]

4.3.6. Evaluation of SERS fingerprinting of MB encapsulated in CB [8]

SERS analysis were carried out on MB alone (by simple addition of 60 µM MB to equal volume of GNR) and MB encapsulated in CB [8] (120 µM MB solution mixed with equal volume of CB [8] solution followed by the addition of equal volume of GNR) using confocal Raman microscope with 633 nm laser source. Strong Raman bands were observed from the MB encapsulated in CB [8]. The intensity of the C–N–C skeletal deformation mode ν (C–N–C)) at 452 cm^{-1} (**Figure 4.12)** and the C–N symmetric stretching mode ν(C–N)) at 1394 cm^{-1} were amazingly enhanced when compared to SERS peaks obtained from MB alone under a 633 nm excitation laser. Moreover, the Au–N stretching mode ν (Au–N) came out at 238 cm^{-1} from the MB-CB [8] nanocomposites, as shown in **Figure 4.12.** This is a clear confirmation that the encapsulated MB molecules were connected to the GNR surface through nitrogen atoms, ensuing an SERS effect by transporting the plasmonic free electrons from the GNRs to the MB molecules. It is expected that the movement of the plasmon-induced electrons from the GNRs to the MB molecules could exhibit a synergistic effect of PTT and PDT on breast cancer cells under single-wavelength NIR laser irradiation.
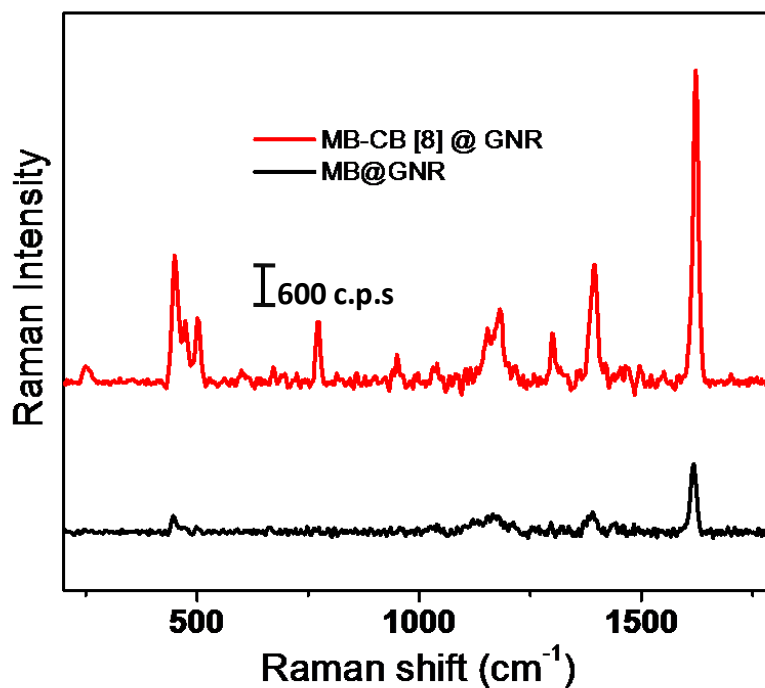
Figure 4.12: SERS spectra of MB alone and MB encapsulated inside CB [8] cavity.

4.3.7. Photothermal conversion of MB-CB [8]@GNR

Photothermal conversion efficiency of **MB-CB [8]@GNR** was examined by recording the temperature changes under 808 nm laser irradiation at 0.1 W/cm^2 with time using a thermocouple integrated multimeter. The temperature of **MB-CB [8]@GNR**, PEG encapsulated GNR and GNR rapidly increased above 55^{0}C within 9 min of laser irradiation, while water alone showed almost no heating effect (**Figure 4.13**). Such an elevation of temperature is essential to cause an irreversible damage to cancer cells.
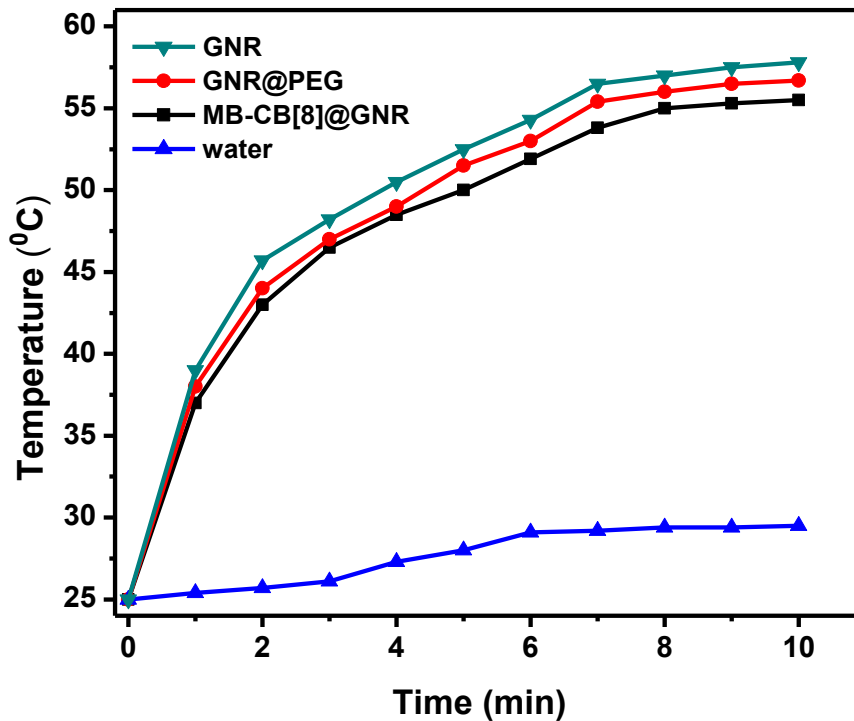
Figure 4.13. Temperature changes of GNR, GNR@PEG, **MB-CB [8]@GNR** irradiated with an 808 nm laser at a power density of 0.1 W/cm^2 as a function of time.

4.3.8. Cellular uptake of MB-CB [8] @GNR-HER2

The cellular uptake of the **MB-CB [8] @GNR-HER2** was examined in human breast cancer SKBR3 cells which over express HER2 receptors. As shown in the confocal fluorescence images (**Figure 4.14**), red fluorescence of MB was clearly visible from SKBR3 cells suggesting both MB, and **MB-CB [8] @GNR-HER2** was internalized efficiently into SKBR3 cells. The fluorescence intensity of **MB-CB [8]@GNR-HER2** from SKBR3 cells was slightly less compared to that of free MB which is in accordance with observation of some extent fluorescence quenching of MB inside CB [8] cavity.
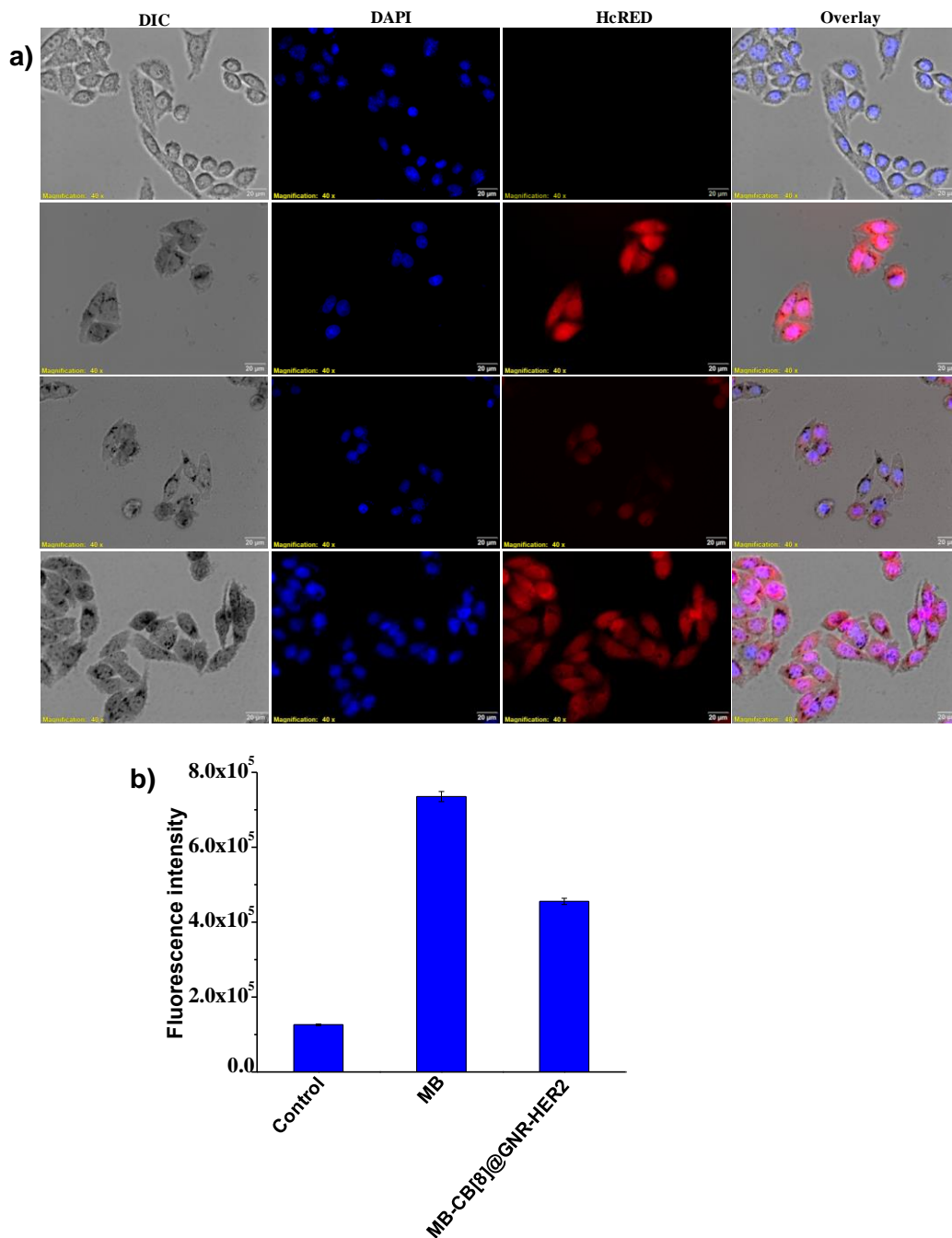
Figure 4.14. a) Fluorescence images of SKBR3 cells after being incubated with MB, MB-CB[8] and **MB-CB [8] @GNR-HER2** for 3 h. (first row control cells, second row cells treated with MB third row cells treated with MB-CB[8] and forth row cells treated with **MB-CB [8] @GNR-HER2**) Scale bar: 20 μm**. b)** Quantification of normalized fluorescence intensity difference between cells treated with MB or **MB-CB[8]@GNR-HER2** along with control.

4.3.9. Cellular recognition of MB-CB [8]@GNR-HER2 by Raman imaging

In order to investigate the cellular recognition, HER2 antibody conjugated **MB-CB [8]@GNR-HER2** was incubated with SKBR3 cells cultured in chamber slide. SERS mapping was carried out after washing with PBS buffer in order to remove the unbound nanoconstruct. Cells incubated with **MB-CB [8]@GNR-HER2** was scanned using the confocal Raman microscope. The cluster analysis was performed on the characteristic Raman spectral scan obtained and the color coded Raman image (cluster mapping) is shown in **Figure. 4.15**. The violet region corresponds to the nanoconstruct, **MB-CB [8]@GNR-HER2** attached to the surface of the SKBR3 cell, red being nucleus, green the cytoplasm and yellow region corresponds to the medium (buffer) and glass container. SKBR3 cells are recognized by targeted nanoconstruct reflecting strong mapping images where the NPs are mostly localized around the cell surface which confirmed the recognition with the HER2 cell-surface receptor. SERS mapping was also carried out in HER2 negative MCF7 cells (**Figure 4.16**) where no traceable Raman image was observed.
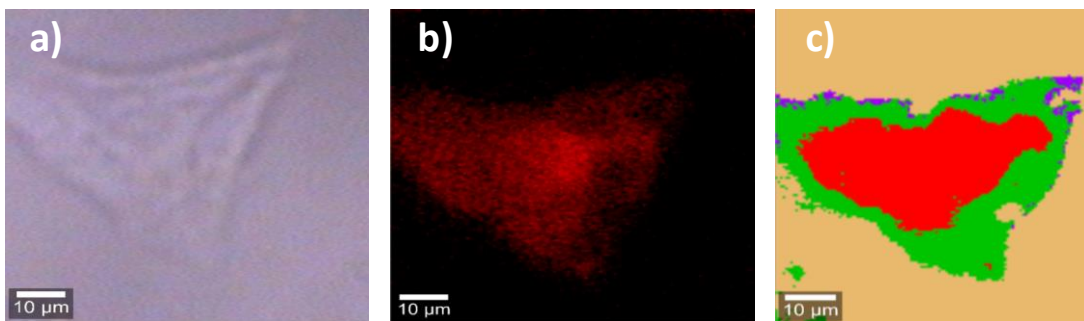

Figure.4.15. Color coded Raman cluster map: (a) white light image; (b) the corresponding confocal Raman distribution image; (c) color coded cluster mapping image of SKBR3 cells incubated with **MB-CB [8] @GNR-HER2** violet : nanoconstruct on the surface, green: cytoplasm, red: nucleus, yellow: buffer.
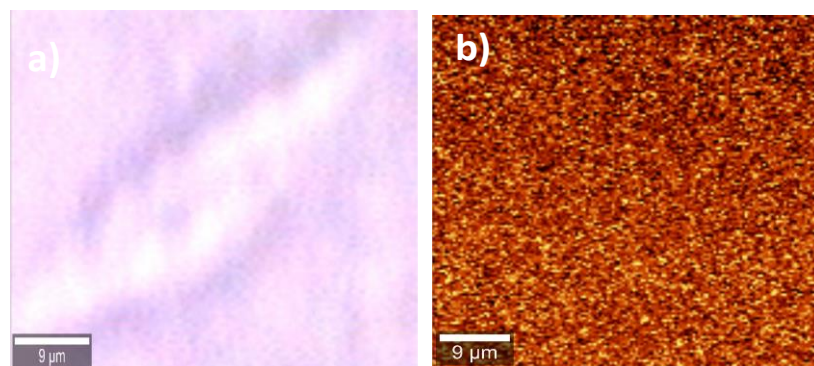
Figure.4.16. (a) white light image, **(b)** the corresponding confocal Raman distribution image of MCF7 cells incubated with **MB-CB [8] @GNR-HER2**

4.3.10. Intracellular ROS generation by MB-CB [8] @GNR-HER2

ROS generation is the mechanism common to all non-surgical therapeutic strategies for cancer treatment, including chemotherapy, radiotherapy and photodynamic therapy, due to its implication in triggering cell death.[38] ROS level in tumor cells is higher than normal cells. Both death receptor- and mitochondria mediated apoptosis rely on ROS.[38,39] PS on excitation with light of suitable wavelength produces reactive oxygen species (ROS) and the anticancer effects of PDT is determined by the generation of cytotoxic ROS produced. In order to detect the ROS level in SKBR3 cells through the photosensitizing effect, ROS staining was carried out for GNR, MB, MB-CB [8] and **MB-CB [8] @GNR-HER2** treated SKBR3 cells upon NIR laser irradiation (λ = 808 nm, 1 W/cm^2) using dichloro-dihydro fluorescein diacetate (DCFH-DA) as the green fluorescence dye. For the GNR- treated cells, the ROS level was negligible even after laser irradiation. However, for the **MB-CB [8]@GNR-HER2** treated SKBR3 cells, the ROS level was significantly enhanced with NIR

laser irradiation, as shown in **Figure. 4.17.** This is a clear evidence that the **MB-CB [8]@GNR-HER2** nanoparticles can induce photothermal effect as well as concomitantly exerted photodynamic effect in presence of the PS under the same 808 nm laser. This implies that the **MB-CB [8] @GNR-HER2** nanoparticles operated according to the direct oxidation process of the MB dimers through a type II photoreaction pathway.
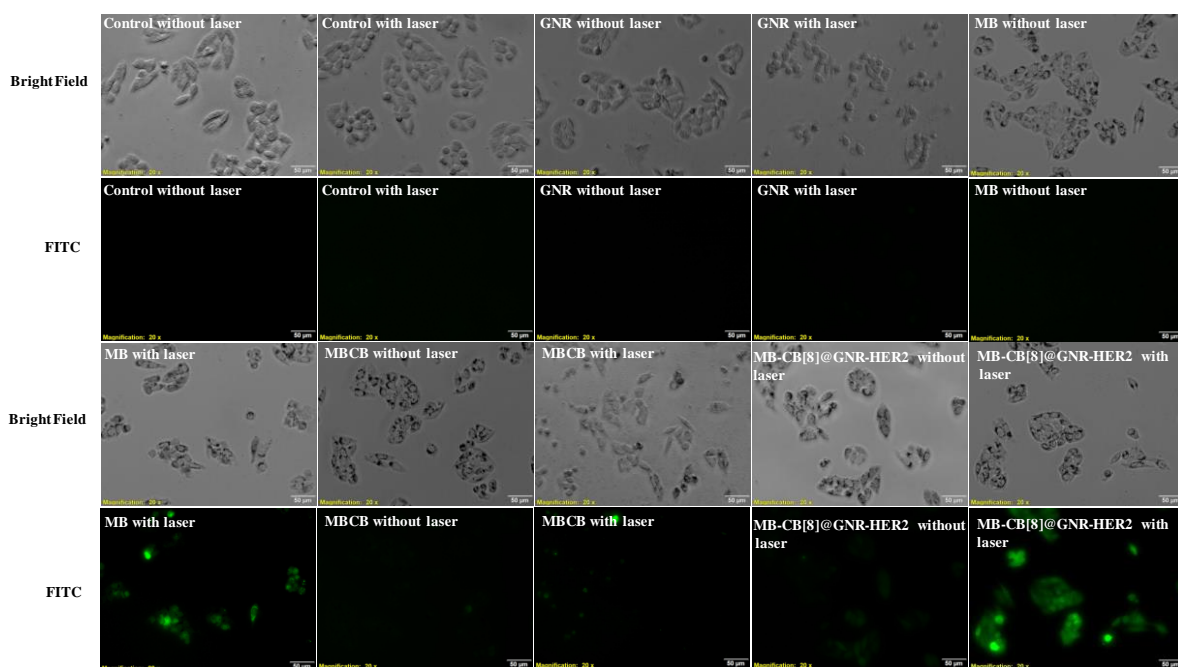
Figure 4.17. DCFH-DA staining of SKBR3 cells incubated with GNR, MB, MB-CB [8] and **MB-CB [8]@GNR-HER2** with and without irradiation with 808 nm laser for 2 min.

4.3.11. *In vitro* evaluation of therapeutic efficiency by MB-CB [8] @ GNR-HER2

Cytotoxic potential of **MB-CB [8] @ GNR-HER2** was evaluated in SKBR3 cells by MTT assay. Cells were treated with MB, MB-CB, GNR and **MB-CB [8] @GNR-HER2** for 4 h and irradiated with 808 nm laser at 1 W/cm^2 for 2 min. MB, MB-CB, GNR and **MB-CB [8] @GNR-HER2** induced negligible cytotoxicity before laser

irradiation, indicating the non-toxic nature of MB, MB-CB, GNR and **MB-CB[8] @GNR-HER2** even at a concentration of 50 μg/mL. Cytotoxicity of the nanoconstruct increased drastically upon laser irradiation. Maximum cytotoxic effect was observed upon 808 nm laser irradiation after 4h incubation with **MB-CB [8] @ GNR-HER2.** This enhanced cytotoxic effect observed under laser irradiation complements the combined effects of PTT and PDT in a targeted fashion (**Figure 4.18**).
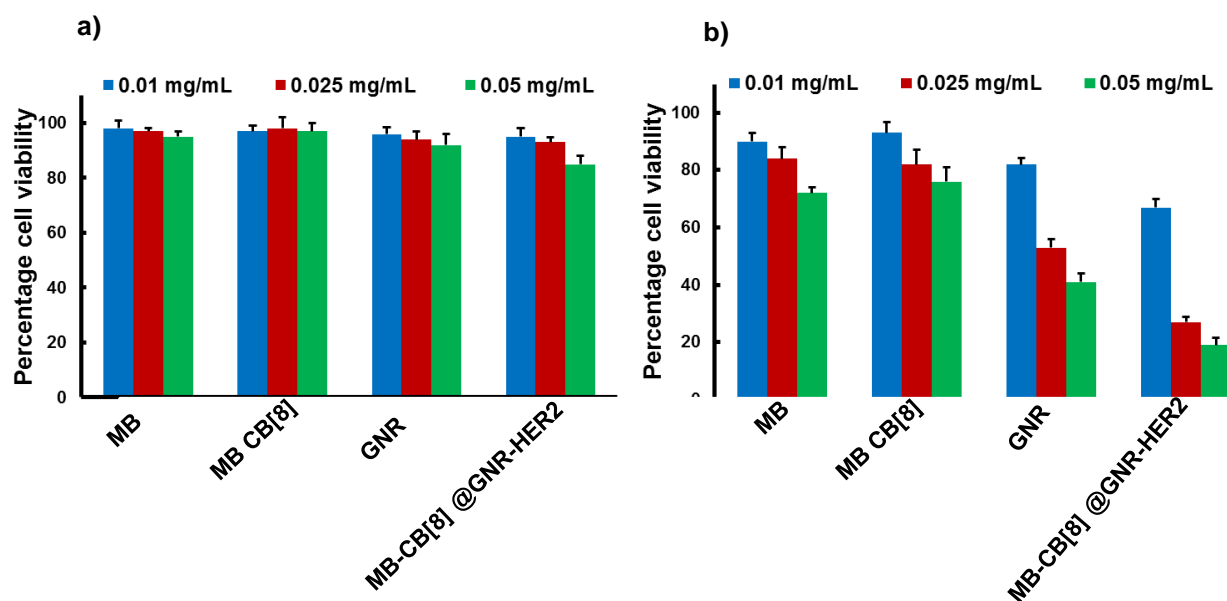
Figure 4.18. *In vitro* cytotoxicity in SKBR3 cells a) without laser irradiation b) with 808 nm laser irradiation at a power density 0.1 W/cm^2, irradiation time 2 min.

Further we have evaluated the cytotoxicity in MCF7 cells as negative control (**Figure 4.19**). Cytoxicity of GNR, MB and MB-CB [8] slightly reduced upon laser irradiation, whereas, MB-CB [8]@GNR-HER2 retained cell viability even after laser

irradiation. This data confirmed the target specific cytotoxicity of the theranostic nanoprobe.
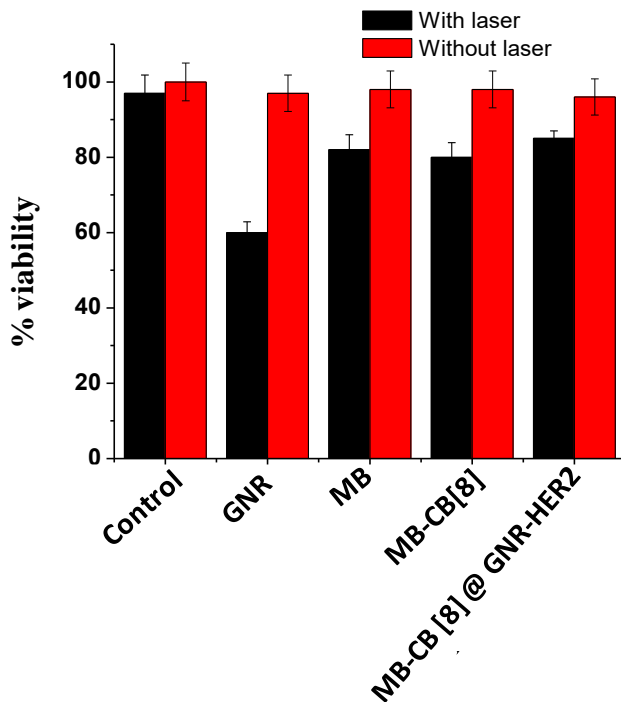
Figure 4.19. *In vitro* cytotoxicity in MCF7 cells incubated with GNR, MB, MB-CB and **MB-CB [8]@GNR-HER2** with or without 808 nm laser irradiation at a power density 0.1 W/cm^2, irradiation time 2 min.

To investigate the method of cell death prompted by **MB-CB [8]@GNR-HER2** in SKBR3 cells in a non-fluorescent platform, APOPercentage™ Apoptotic assay was executed. Apoptosis initiates with the transfer of phosphatidylserine from the inner to the outer surface of the cell membrane. This PS transmembrane movement causes in the uptake of the APOPercentage dye by the cells undergoing apoptosis, and it lasts until blebbing takes place, which is the distinct characteristic of apoptosis. The representative images that illustrate the results of the assay captured under a

conventional microscope are shown in **Figure. 4.20**. The **MB-CB [8]@GNR-HER2** treated cells which undergo apoptosis, distinctly absorb the dye and get stained intense purple-red and the control cells persisted unstained.

Figure 4.20. Photomicrographs of SKBR3 cells incubated with GNR and **MB-CB [8] @ GNR-HER2** after irradiation with 808nm laser for 2 min. (Scale bar corresponds to 100 µM)

The cytotoxicity of the nanoconstruct upon laser irradiation was further confirmed by double immunofluorescence assay with acridine orange (green fluorescence) and ethidium bromide (red fluorescence) dyes used as staining dyes for live and dead cell differentiation respectively. Control cells with laser irradiation showed a few early

apoptotic cells with condensed chromatin and nuclear fragmentation which appear as bright green dots in the nuclei, when compared with the cells without laser irradiation. As compared to the bare GNRs treated cells (**Figure 4.21**), the live cell population were decreased in case of **MB-CB [8] @GNR-HER2** treated cells upon NIR laser irradiation. This result is in well agreement with the above MTT assay results.

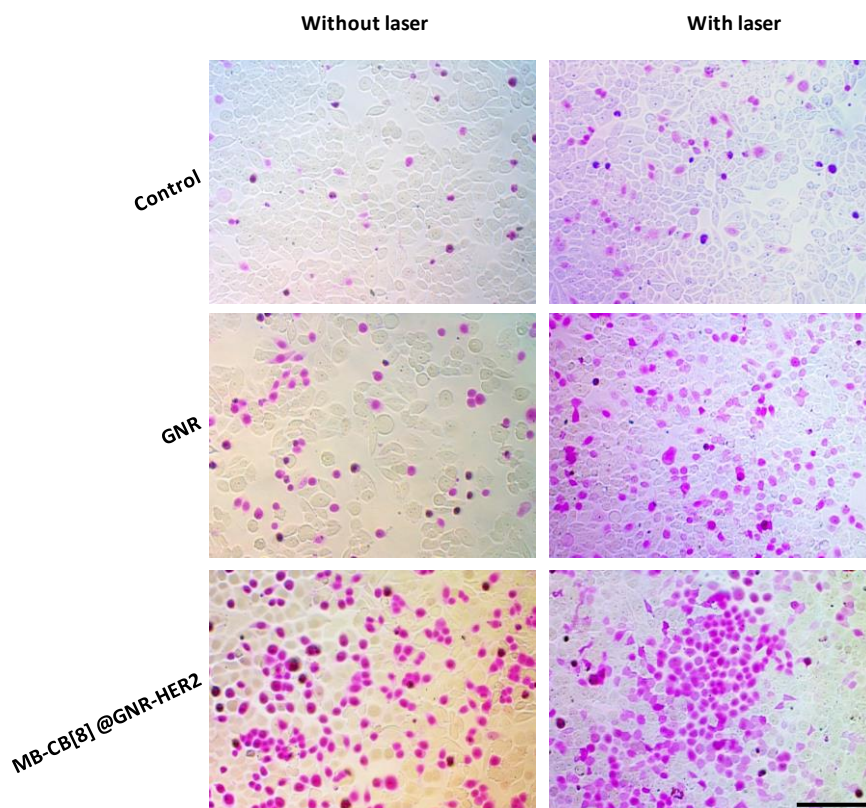| Control | Control with laser | GNR with laser | MB-CB [8]@GNR-HER2 with laser |
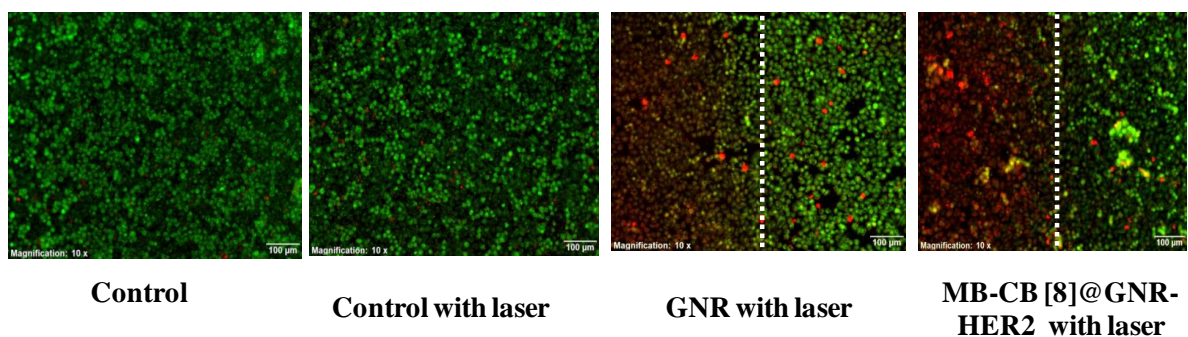
Figure 4.21. AO/EtBr dual staining of SKBR3 cells incubated with GNR and **MB-CB[8]@GNR-HER2** after irradiation with 808nm laser for 2 min (The laser irradiated area is marked with white dotted line). scale bar corresponds to 200 µm.

Morphological changes observed with staining assays were further confirmed by Annexin V-FITC assay, using flow cytometry. SKBR3 cells were treated with GNR and **MB-CB [8] @ GNR-HER2** for 4 h with or without laser irradiation, and labeled with Propidium iodide (PI) as well as Annexin V. The percentage of apoptotic cells after treatment or negative control are represented in **Figure 4.22.** The flow cytometry data showed that SKBR3 cells incubated with GNR after 808 nm laser irradiation for 1min showed a lesser proportion of apoptotic cell death (37.6%) where as a higher proportion of apoptotic death (58.5%) was occurred after treatment

with the **MB-CB [8]@GNR-HER2** followed by laser irradiation. This data clearly indicates the superiority of combined phototherapy over individual therapy.
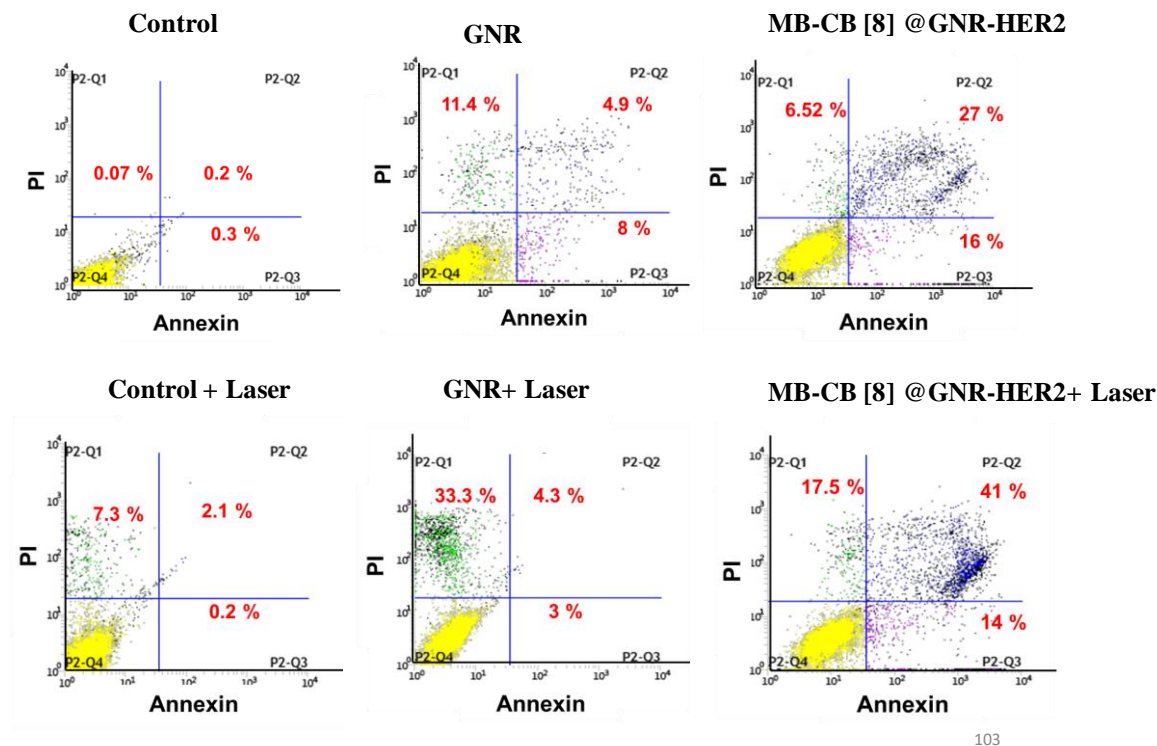
Figure 4.22. Annexin V-FITC staining by flow cytometry of SKBR3 cells incubated with GNR, **MB-CB [8] @GNR-HER2**.

4.4 Conclusion

A novel strategic development of theranostic nanoprobe **MB-CB [8]@GNR-HER2** was adopted for efficient treatment of breast tumor cells in a target specific manner with minimal side effect. The designed theranostic probe effectively detected exact tumor location through tumor targeting moiety i.e. HER2 and executed safe phototherapy (PDT and PTT). The fluorescence from the PS was explored for the cell imaging and the target recognition of the nanoconstruct was validated by SERS imaging. In this study, we introduced GNRs-PS complex as a multifunctional

theranostics platform for synergistic effect of PTT and PDT under single laser irradiation. The nanoconstruct served as an alternative strategy to overcome the drawbacks of conventional PDT by encapsulating MB dimers in CB [8] cavity and performed the enhanced therapeutic efficacy. Moreover, apoptotic event was examined by the theranostic nanoprobe in cellular level with various apoptotic assays. Therefore, as a proof of concept, designated theranostic nanoprobe proved to be an excellent nanomedicine for the treatment of breast tumor cells under dual phototherapeutic modality.

4.5. EXPERIMENTAL SECTION.

4.5.1. Materials and Methods

All the chemicals (synthetic building blocks) and solvents were purchased from Sigma Aldrich, Alfa Aesar, Fluka, Merck, and used without further purification. ^{1}H-NMR spectra were recorded on Bruker Advance 500 NMR spectrometer, and chemical shifts are expressed in parts per million (ppm). Mass spectra were recorded under ESI/HRMS at 61800 resolution using Thermo scientific exactive, mass spectrometer. Surface Plasmon absorption spectra were measured on a Spectra Max M2 spectrophotometer (Molecular Devices), and the data analysis was performed using GraphPad Prism 5.0/ Microsoft excel and Origin 7. TEM measurements were performed on a JEOL 2010 high-resolution transmission electron microscope with an accelerating voltage of 200 KV. The sample was prepared by pipetting a drop of the aqueous solution of nanoparticles onto a 230 mesh copper grid coated with carbon

and the sample was allowed to dry in air before the measurement. The fluorescence emission spectra were recorded using a Shimadzu RF-5301PC spectrofluorophotometer.

4.5.2. Preparation of GNRs.

GNRs was prepared by adding around 5 mL of cetyltrimethylammonium bromide (CTAB solution (200 mM CTAB in deionized water) to 5 mL deionised water. 40 μL of 250 mM HAuCl$_4$ aqueous solution was added to above solution then its colour changes to light yellow. Then 500 μL of 4 mM silver nitrate solution was added followed by the addition of 250 μL 80 mM ascorbic acid solution. The solution immediately changes colourless followed by the addition of freshly prepared 5 μL 10 mM sodium borohydride solution and kept undisturbed for 30min, centrifuged to remove excess CTAB.

4.5.3 Thiolated PEG encapsulation.

GNRs was prepared by well established seed mediated method. The hetero functional linker SH-C$_2$H$_4$-CONHPEG-C$_3$H$_6$-COOH (PEG MW: 3000 dalton; RAPP Polymer GmbH) solution (10 μM) was added to GNR solution in a polypropylene tube with rapid mixing. After 15min of mixing the Au-colloid was exposed to excess of CH$_3$-PEG-SH (PEG MW: 5000 dalton; RAPP Polymer GmbH) (10 μM) to maximize its surface coverage and to stabilize the PEG. Excess PEG-SH was removed after 3 h of through mixing by three rounds of centrifugation (4000 rpm, 15min) and resuspended in milli-Q water. For antibody conjugation water was replaced by phosphate-

buffered saline (PBS) for covalent conjugation at the carboxyl terminal of heterofunctional PEG. Successful PEG encapsulation was confirmed by UV-Vis absorption studies.

4.5.4. Antibody conjugation of PEG encapsulated GNR

The antibody was purified by filtration using Amicon Ultra 3K centrifuge filters (Milipore) to remove the sodium azide. The carboxylic groups of the PEG encapsulated nanorod was activated by EDC N-(3-(dimethylamino)-propyl)-N'-ethylcarbodiimide (EDC, 25 mM) and N-hydroxysuccinimide (NHS, 25 mM). After 30 min incubation, excess of EDC and NHS was removed by 3 rounds of centrifugation (8000 rpm, 15min), and re-suspended in PBS using Amicon Ultra 3K centrifuge filters (Milipore). The activated nanotags GNR-PEG was incubated with antibody HER2 (20µL, 200µg/ mL) at 25 ^{0}C for 2 h. Antibody conjugated nanotags were stored at 4 ^{0}C overnight. Further unbound antibodies were removed by a five round of centrifugation at 10000 rpm 5min. The pellet containing the antibody conjugated nanorods were then again resuspended in PBS and stored at 4^{0}C. Antibody conjugation was further confirmed by UV-Vis Spectroscopy and Sodium Dodecyl sulphate Poly Acrylamide Gel Electrophoresis.

4.5.5. SDS Polyacrylamide Gel Electrophoresis.

 To confirm the antibody conjugation SDS polyacrylamide gel electrophoresis was done. A 12 % resolving and 5% stacking gel was used for the separation of conjugated and pure antibodies.

4.5.6. Cell Culture.

The human cancer cell lines SKBR3 was obtained from American Type Culture Collection (ATCC, USA). The cells were maintained in Dulbecco's Modified Eagle's Medium (DMEM) media supplemented with 10% fetal bovine serum and antibiotics (100U mL^{-1} penicillin/100 μg mL^{-1} streptomycin mixture) in a 5 % CO_2 incubator at 37 ^{0}C.

4.5.7. Cell viability assay.

SKBR3 cells were seeded at a density of 10^4 cells/well in two 96 well plates and incubated at 37 ^{0}C for sufficient growth. Control, GNR, **MB-CB [8]@GNR** were added to the wells separately in each plates. The concentration of MB and GNR is maintained with respect to free MB and GNR in the final construct. For preparing 0.01 mg/mL of final construct, 0.04 mg/mL MB solution was mixed with equal volume of 0.04 mg/mL CB[8] solution to obtain 0.02 mg/mL of MB-CB[8] which was mixed with equal volume of 0.02 mg/ML of GNR to get final construct containing 0.01 mg/mL of each component .The treated cells were the incubated for 4 hours. Then one of the plates were irradiated with 808 nm laser for 1 min.100 μl MTT (0.5mg/ml) was added to each well and the purple color formation was measured colorimetrically at 570 nm.

4.5.8. APOPercentage™ apoptosis assay

Apoptosis was also monitored using APOPercentage™ dye (Biocolor, Belfast, Northern Ireland). Briefly, 1x 10^4 SKBR3 cells were cultured in 96- well tissue culture plates and grown to sub-confluent monolayers for 48 h. The cells were

incubated with GNR and **MB-CB [8]@GNR** for 24 h and then irradiated with 808 nm laser for 1 min. The culture medium was removed, and analysed after 1 h incubation with a fresh culture medium consisting of APOPercentage dye. The images of APOPercentage dye-labelled cells, which stained purple under a light microscope, were used to visualize the extent of apoptosis.

4.5.9. Live dead assay

100 µg/ mL Acridine orange (AO) and 100 µg/mL ethidium bromide (EB) were mixed in 1:1 ratio. 200 µL of the final mixture was added to 24 well plate. Washed twice with PBS after 2 min. Fluorescence images were taken. Live cells were stained green and dead cells stained orange /red.

4.5.10. Annexin V assay

Additionally, evaluation of apoptosis by FITC Annexin V staining (FITC Annexin V apoptosis detection kit from BD Pharmingen #556547, BD Biosciences, San Jose, CA) was also confirmed by flow cytometry, using kit specified instructions. Signals were then detected using a fluorescence activated cell sorting (FACS) Calibur flow cytometer (BD Biosciences, San Jose, CA) and the data was analyzed with the Cell Quest Pro software.

4.6. Reference

(1)   Li, W.-S.; Lam, W. S.; Liu, K.-C.; Wang, C.-H.; Chang, H. C.; Jen, Y. C.; Hsu, Y.-T.; Shivatare, S. S.; Jao, S.-C. *Org. Lett.* **2010**, *12* (1), 20.

(2)   Vaidya, A.; Sun, Y.; Ke, T.; Jeong, E. K.; Lu, Z. R. *Magn. Reson. Med.* **2006**,

56 (4), 761.

(3)   Tian, B.; Wang, C.; Zhang, S.; Feng, L.; Liu, Z. *ACS Nano* **2011**, *5* (9), 7000.

(4)   Awuah, S. G.; You, Y. *RSC Adv.* **2012**, *2* (30), 11169.

(5)   Greer, A. *Acc. Chem. Res.* **2006**, *39* (11), 797.

(6)   Avirah, R. R.; Jayaram, D. T.; Adarsh, N.; Ramaiah, D. *Org. Biomol. Chem.* **2012**, *10* (5), 911.

(7)   Pandey, R. K.; Goswami, L. N.; Chen, Y.; Gryshuk, A.; Missert, J. R.; Oseroff, A.; Dougherty, T. J. *Lasers Surg. Med.* **2006**, *38* (5), 445.

(8)   Momenteau, M.; Maillard, P.; de Bélinay, M.-A.; Carrez, D.; Croisy, A. *J. Biomed. Opt.* **1999**, *4* (3), 1.

(9)   Yu, J.; Hsu, C.; Huang, C.; Chang, P. *Appl. Mater. Interfaces* **2014**, *7*, 432.

(10)   Klepac-ceraj, V.; Patel, N.; Song, X.; Holewa, C. *Lasers Surg Med.* **2012**, *43* (7), 600.

(11)   Tang, W.; Xu, H.; Kopelman, R.; Philbert, M. A. *J. Photochem. Photobiol.* **2005**, *81*, 242.

(12)   Khanal, A.; Bui, M. N.; Seo, S. S. *J Breast Cancer* **2014**, *17* (1), 18.

(13)   Golab, J.; Korbelik, M.; Russell, D.; Preise, D.; Scherz, A.; Salomon, Y. *Photochem. Photobiol. Sci* **2011**, *10*, 832.

(14)   Masson, E.; Ling, X.; Joseph, R.; Kyeremeh-Mensah, L.; Lu, X. *Cucurbituril chemistry: a tale of supramolecular success*; 2012; Vol. 2.

(15)   Barrow, S. J.; Kasera, S.; Rowland, M. J.; Scherman, O. A. *Chem.Rev.* **2015**, *115*, 12320.

(16) Taylor, R. W.; Lee, T.; Scherman, O. A.; Esteban, R.; Aizpurua, J.; Huang, F. M.; Baumberg, J. J.; Mahajan, S.; Al, T. E. T. *ACS Nano* **2011**, *5* (5), 3878.

(17) Jones, S. T.; Taylor, R. W.; Esteban, R.; Abo-hamed, E. K.; Bomans, P. H. H.; Sommerdijk, N. A. J. M.; Aizpurua, J.; Baumberg, J. J.; Scherman, O. A. *Small* **2014**, *10* (21), 4298.

(18) Zhang, D.; Wu, M.; Zeng, Y.; Wu, L.; Wang, Q.; Han, X.; Liu, X.; Liu, J. *ACS Appl. Mater. Interfaces* **2015**, *7* (15), 8176.

(19) Wang, K.; Zhang, Y.; Wang, J.; Yuan, A.; Sun, M.; Wu, J.; Hu, Y. *Sci. Rep.* **2016**, *6* (1), 27421.

(20) Bucharskaya, A.; Maslyakova, G.; Terentyuk, G.; Yakunin, A.; Avetisyan, Y.; Bibikova, O.; Tuchina, E.; Khlebtsov, B.; Khlebtsov, N.; Tuchin, V. *Int. J. Mol. Sci.* **2016**, *17* (8), 1.

(21) Li, W. T.; Peng, J. R.; Tan, L. W.; Wu, J.; Shi, K.; Qu, Y.; Wei, X. W.; Qian, Z. Y. *Mild photothermal therapy/photodynamic therapy/chemotherapy of breast cancer by Lyp-1 modified Docetaxel/IR820 Co-loaded micelles*; Elsevier Ltd, 2016; Vol. 106.

(22) Han, H. S.; Choi, K. Y.; Lee, H.; Lee, M.; An, J. Y.; Shin, S.; Kwon, S.; Lee, D. S.; Park, J. H. *ACS Nano* **2016**, *10* (12), 10858.

(23) Wang, N.; Zhao, Z.; Lv, Y.; Fan, H.; Bai, H.; Meng, H.; Long, Y.; Fu, T.; Zhang, X.; Tan, W. *Nano Res.* **2014**, *7* (9), 1291.

(24) Jang, B.; Park, J.; Tung, C.; Kim, I.; Choi, Y. *ACS Nano* **2011**, *5* (2), 1086.

(25) Lin, J.; Wang, S.; Huang, P.; Wang, Z.; Chen, S.; Niu, G.; Li, W.; He, J.; Cui,

D.; Lu, G.; Chen, X.; Nie, Z. *ACS Nano* **2013**, *7* (6), 5320.

(26) Gao, L.; Fei, J.; Zhao, J.; Li, H.; Cui, Y.; Li, J. *ACS Nano* **2012**, *6* (9), 8030.

(27) Kim, J.-Y.; Choi, W. Il; Kim, M.; Tae, G. *J. Control. Release* **2013**, *171* (2), 113.

(28) Wang, S.; Riedinger, A.; Li, H.; Fu, C.; Liu, H.; Li, L.; Liu, T.; Tan, L.; Barthel, M. J.; Pugliese, G.; De Donato, F.; Scotto D'Abbusco, M.; Meng, X.; Manna, L.; Meng, H.; Pellegrino, T. *ACS Nano* **2015**, *9* (2), 1788.

(29) Gayathri Devi, D.; Cibin, T. R.; Ramaiah, D.; Abraham, A. *J. Photochem. Photobiol. B Biol.* **2008**, *92* (3), 153.

(30) Montes-navajas, P.; Corma, A.; Garcia, H. *chemPhysChem* **2008**, *9*, 713.

(31) Seo, S.; Kim, B.; Joe, A.; Han, H.; Chen, X.; Cheng, Z.; Jang, E. *Biomaterials.* **2015**, *35* (10), 3309.

(32) Alsammarraie, F. K.; Lin, M. *J. Agric. Food Chem.* **2017**, *65* (3), 666.

(33) Maiti, K. K.; Dinish, U. S.; Fu, C. Y.; Lee, J. J.; Soh, K. S.; Yun, S. W.; Bhuvaneswari, R.; Olivo, M.; Chang, Y. T. *Biosens. Bioelectron.* **2010**, *26* (2), 398.

(34) Samanta, A.; Maiti, K. K.; Soh, K. S.; Liao, X.; Vendrell, M.; Dinish, U. S.; Yun, S. W.; Bhuvaneswari, R.; Kim, H.; Rautela, S.; Chung, J.; Olivo, M.; Chang, Y. T. *Angew. Chemie - Int. Ed.* **2011**, *50* (27), 6089.

(35) Taylor, R. W.; Lee, T. C.; Scherman, O. A.; Esteban, R.; Aizpurua, J.; Huang, F. M.; Baumberg, J. J.; Mahajan, S. *ACS Nano* **2011**, *5* (5), 3878.

(36) Lee, T. C.; Scherman, O. A. *Chem. - A Eur. J.* **2012**, *18* (6), 1628.

(37)   Jones, S. T.; Taylor, R. W.; Esteban, R.; Abo-Hamed, E. K.; Bomans, P. H. H.; Sommerdijk, N. A. J. M.; Aizpurua, J.; Baumberg, J. J.; Scherman, O. A. *Small* **2014**, *10* (21), 4298.

(38)   Wang, J.; Yi, J. *Cancer Biol. Ther.* **2008**, *7* (12), 1875.

(39)   Mroz, P.; Yaroslavsky, A.; Kharkwal, G. B.; Hamblin, M. R. *Cancers (Basel).* **2011**, *3* (2), 2516.

List of publications

1. Investigation of apoptotic events at molecular level induced by SERS guided targeted theranostic nanoprobe; **Nisha N**, Lakshmi V. Nair, Varsha Karunakaran, Manu M. Joseph, Jyothi B. Nair, Ramya A. N., Ramapurath S. Jayasree* and Kaustabh Kumar Maiti*, *Nanoscale*., **2016**, 8, 11392-1139

2. New Insight of Tetraphenylethylene-based Raman Signatures for Targeted SERS Nanoprobe Construction Toward Prostate Cancer Cell Detection;Adukkadan N. Ramya, Manu M. Joseph, Jyothi B. Nair, Varsha Karunakaran, **Nisha N.**, and Kaustabh Kumar Maiti*, *ACS Appl. Mater. Interfaces*., **2016**, 8, 10220-10225

3. Aggregation induced Raman scattering of squaraine dye: Implementation in diagnosis of cervical cancer dysplasia by SERS imaging ; **Nisha N**, Varsha Karunakaran, Willi Paul, Karunakaran Venugopal, K. Sujathan, Kaustabh Kumar Maiti*, *Biosens. Bioelectron*, **2015**, 70, 145-152

4. New Insight of Squaraine Based Biocompatible SERS Nanotag for Cancer Cell Imaging; Ramya, A.N., A. Samanta, **Nisha, N**, Y-T. Chang, Kaustabh K. Maiti*, *Nanomedicine*, **2015**,10, 561-71

5. Exploration of Targeted Theranostic Nanoprobe built on SERS and Fluorescence Dual Imaging Platform with Enhanced Phototherapy for Breast Cancer Treatment; **Nisha N**, Hema S. K., Manu M. Joseph, Varsha Karunakaran, Ramapurath S. Jayasree* and Kaustabh Kumar Maiti* *(To be communicated)*

6. Exploring the Margins of SERS in Practical Domain: An Emerging Diagnostic Modality for Modern Biomedical Applications (Review); Manu M. Joseph, **Nisha N.**, Jyothi B. Nair, Varsha Karunakaran, Ramya A.N. Sujai P.T. Saranya Giridharan, Arya J.S. *(To be communicated)*

Papers presented at conferences (Posters/Oral)

1. The International Symposium on Photonics Applications and Nanomaterials; Organized by Sree Chitra Tirunal Institute for Medical Sciences & Technology, Thiruvananthapuram (Oct, 28-30th, 2015); Development of SERS Active Nano Probe for Targeted Chemothermal Therapy **(Oral presentation)**

2. 6th International Conference on Nano Science and Technology (ICONSAT 2014); Organized by Institute of Nano Science and Technology (INST), Mohali, Punjab (March, 2-5, 2014). **(Poster presentation)** Nisha N., Jyothi B. Nair, Kaustabh Kumar Maiti. "New Insight of Squaraine Based Raman Reporters for Construction of Diagnostic SERS Nano-Probe In Cancer Screening."

3. 2nd International Conference on Advanced Functional Materials (ICAFM 2014), Organized by CSIR-NIIST, Trivandrum (19-21 February, 2014). **(Poster presentation)** Nisha N., Jyothi B. Nair, Kaustabh Kumar Maiti. "New Insight of Squaraine Based Raman Reporters for Construction of Diagnostic SERS Nano-Probe In Cancer Screening."